Noninvasive Neuromodulation:
Modeling and Analysis of Transcranial Brain Stimulation with Applications to Electric and Magnetic Seizure Therapy

Won Hee Lee

Submitted in partial fulfillment of the
requirements for the degree
of Doctoral of Philosophy
in the Graduate School of Arts and Sciences

COLUMBIA UNIVERSITY

2014

ABSTRACT

Noninvasive Neuromodulation: Modeling and Analysis of Transcranial Brain Stimulation with Applications to Electric and Magnetic Seizure Therapy

Won Hee Lee

Bridging the fields of engineering and psychiatry, this dissertation proposes a novel framework for the rational dosing of electric and magnetic seizure therapy, including electroconvulsive therapy (ECT) and magnetic seizure therapy (MST), for the treatment of psychiatric disorders such as medication resistant major depression and schizophrenia. The objective of this dissertation is to develop computational modeling tools that allow ECT and MST stimulation paradigms to be biophysically optimized *ex vivo*, prior to testing safety and efficacy in preclinical and clinical trials. Despite therapeutic advances, treatment resistant depression (TRD) remains a largely unmet clinical need. ECT is highly effective for TRD, but its side effects limit its real-world clinical utility. Modifications of treatment technique (e.g., electrode placement, stimulus parameters, novel paradigms such as MST) significantly improve the tolerability of convulsive therapy. However, we know relatively little about the distribution of the electric field (E-field) induced in the brain to inform spatial targeting of ECT and MST. Lacking an understanding of biophysical and physiological mechanisms, refinements in ECT/MST technique rely exclusively on time-consuming and costly clinical trials. Consequently, key questions remain unanswered about how to position the ECT electrodes or MST coil for targeted brain

stimulation. Addressing this knowledge gap, this dissertation proposes a new platform that will inform an improved spatial targeting of ECT and MST through state-of-the-art computer simulations of the E-field distribution in human and nonhuman primate (NHP) brain.

Part I of this dissertation aims to develop anatomically realistic finite element models of transcranial electric and magnetic stimulation in human and NHPs incorporating tissue heterogeneity and anisotropy derived from structural magnetic resonance imaging (MRI) and diffusion tensor imaging (DTI) data. The NHP models of ECT and MST are created alongside the human model since NHPs are used in preclinical studies on the mechanisms of seizure therapy.

Part II of this dissertation aims to apply the model developed in Part I to electric and magnetic seizure therapy. We compute the strength and spatial distributions of the E-field induced in the brain by various ECT and MST paradigms. The relative E-field strength among various regions of interest (ROIs) is examined to select electrode/coil configurations that produce most focal stimulation of target ROIs that are considered to mediate the therapeutic action of ECT and MST. Since E-field alone is insufficient to account for individual differences in neurophysiological response, we calibrate the E-field maps relative to the neural activation threshold via *in vivo* measurements of the corticospinal tract response to single pulses (motor threshold, MT). We derive an empirical estimate of the neural activation threshold by coupling simulated E-field strength with individually measured MT. The E-field strength relative to an empirical neural activation threshold and corresponding volume of suprathreshold stimulation (focality) is examined to inform the selection of ECT and MST stimulus pulse amplitude that will result in focal ROI stimulation. We contrast the ECT/MST stimulation strength and focality with conventional fixed and individually titrated pulse amplitude necessary to induce a seizure

(seizure threshold, ST) to study pulse amplitude adjustment as a novel means of controlling stimulation strength and focality. This work provides a basis for rational dosing of seizure therapies that could help improve their risk/benefit ratio and guide the development of safer alternatives for patients with severe psychiatric disorders.

Table of Contents

List of Figures

List of Tables

Acknowledgements

The work on this dissertation has given me great pleasure, largely due to the support of many wonderful and inspiring people.

I would like to express my deepest gratitude to my advisor, Professor Angel Peterchev for his guidance and unwavering support throughout my doctoral studies. He gave me the opportunity to work with him on challenging problems in brain stimulation and always supported me with encouragement and motivation over the years. He has been with me every step of the way guiding my work and nurturing my career. I am grateful for all his support, encouragement, and patience.

I am greatly indebted to my co-advisor, Professor Andrew Laine for his support and guidance. Throughout the years his friendliness and understanding have made my graduate school enjoyable. I have to thank Dr. Laine for his encouragement and invaluable advice and support on the field of medical imaging and signal processing.

I would like to express my sincere appreciation to Professor Sarah Lisanby for recognizing the clinical significance of this work. I had the great honor of working with her. Her enthusiasm has always been a great asset. I am grateful for her valuable feedback, support, and constructive advice.

I would like to thank Professors Paul Sajda and Qi Wang for serving on my proposal and defense committee for their enormous generosity in the midst of busy schedules and for their vote of confidence. They have been a source of encouragement and advice that have contributed a great deal in the course of my doctoral work.

Thanks to all current members and alumni of the Heffner Biomedical Imaging Laboratory at Columbia University and of Brain Stimulation and Neurophysiology Division at Duke University. Special thanks to Drs. Zhi-De Deng and Stefan Goetz for their scientific discussions and constructive comments.

Last but not least, I would like to express appreciation to my parents for their unconditional love, endless support and encouragement, and to my brother and his family for their understanding and encouragement. I would also like to express my sincere love and gratitude toward my grandmothers. Their love and devotion will always be remembered.

To my family for their love and support

Chapter 1

Introduction

1.1. Overview of Electric and Magnetic Seizure Therapy

Treatment resistant depression remains a largely unmet clinical need. Despite advances in psychotherapeutic, neuropharmacologic, and device-based therapies, electroconvulsive therapy (ECT) remains the most effective and rapidly acting treatment for severe, acute, and medication resistant psychiatric disorders such as major depression and treatment resistant schizophrenia. However, the cognitive side effects of ECT, including post-ictal disorientation, decreased processing speed, poor attention, and impaired memory (particularly retrograde amnesia), limit its clinical utility. These adverse side effects can lead to functional impairments, increased relapse rates, poor clinical outcome, increased burden, and deter patients and practitioners. Fortunately, modifications of dosing paradigms can improve the side effect profile, including alterations in ECT technique and the use of magnetic fields to induce the seizure (magnetic seizure therapy, MST). Unfortunately, key questions about the impact of dosing parameters on clinical outcomes remain unanswered, because the biophysical principles governing the relations

among parameters and clinical outcome are incompletely understood. This knowledge gap impedes optimization of definitive treatment for severe depression and other disabling conditions. Furthermore, conventional approaches to dosing seizure therapies have limitations that adversely impact clinical care and hamper the progress of research to refine and improve this lifesaving treatment.

1.2. Background and Significance

1.2.1. Major Depressive Disorder

Major depressive disorder (MDD) is a leading public health problem that contributes to substantial disability, morbidity, and mortality. MDD has a lifetime prevalence of 16% (about 34 million Americans) [2, 3]. MDD is one of the leading causes of disability/burden of illness [4]. The World Health Organization (WHO) estimates that MDD will be the second most common cause of disability worldwide by 2020 [5]. MDD is life-shortening due both to suicide and the association with increased mortality from other medical conditions. These observations make it particularly distressing that only 37% of patients achieved remission with their first antidepressant medication in the Sequenced Treatment Alternatives to Relieve Depression (STAR*D) trial, and that the odds of responding to antidepressant medications diminish with each successive trial (31%, 14%, and 13% after the second, third, and fourth trial, respectively). Overall, 33% of patients failed to achieve remission despite multiple trials and augmentation steps [6]. If we assume 33% of the estimated 14 million Americans with depression per year are

treatment resistant [2, 3], that yields an estimated 4.6 million Americans with TRD. ECT plays a vital role in meeting this pressing clinical need.

1.2.2. Electroconvulsive Therapy

ECT is administered by delivering electric current to the brain via scalp electrodes to induce a generalized tonic-clonic seizure under anesthesia. ECT continues to play an important role in TRD because its unparalleled efficacy and speed of response are unmatched by medications, transcranial magnetic stimulation (TMS), or vagus nerve stimulation (VNS). For patients who do not respond adequately to currently available pharmacotherapy or cannot tolerate their side effects, the efficacy and speed of response to ECT are unparalleled [7]. The Consortium for Research in ECT (CORE) reported a 75% remission rate to ECT among patients with MDD. Over half of patients showed an initial response by the end of week 1, 34% of patients remitted by week 2, and 65% remitted by weeks 3-4 [8]. ECT is also rapidly effective in treating suicidality [9], the greatest source of morbidity and mortality from depression. It is estimated that 1-2 million patients worldwide and 100,000 patients in the United States receive ECT each year [10]. Given the exceptionally high remission rates and rapid speed of response with ECT, it is perhaps surprising that ECT utilization rates are so much lower than the estimated prevalence of TRD (only 0.1 million of the estimated 4.6 million Americans with depression receiving ECT per year in the US). These numbers suggest that only about 2% of patients who could benefit from ECT actually receive it. The cognitive side effects of ECT may be partially responsible for this apparent underutilization of this lifesaving treatment. Thus, strategies to reduce these adverse side effects would have a major public health impact.

American Psychiatric Association practice guideline for MDD recommends ECT for difficult-to-treat depression, either after failure of less invasive treatments, or as an initial treatment for those patients with severe symptoms, psychotic features, prior good response to ECT, need for rapid response, intolerance to medications, or those who have a preference for ECT [11]. However, in practice ECT is often used much later in the course of treatment or not at all, due both to its stigma and, most importantly, its well-recognized cognitive side effects [12-14]. Indeed, the cognitive side effects of ECT reduce its tolerability and deter many patients from receiving this potentially lifesaving treatment. Retrograde amnesia is the most persistent adverse effect of ECT [15-18]. Shortly after ECT, most patients have gaps in memory for events that occurred close in time to ECT, but retrograde amnesia may extend back several months or years. While retrograde amnesia often improves during the first few months following ECT, for many patients recovery is incomplete, with prolonged amnesia for events that occurred close to the time of treatment [19]. Specific cognitive deficits can persist for at least 6 months [20]. Cognitive impairment is not the only side effect of concern with ECT. Cardiac complications represent the most frequent complication seen with ECT [21]. The tachycardia, hypertension, and risk of arrhythmias associated with the treatment represent special risks for patients with comorbid ischemic heart disease, aneurysms, cardiac arrhythmias, pacemakers/implanted defibrillators, and cerebrovascular disease. These side effects deter some patients from accepting ECT and deter practitioners from prescribing it. Yet evidence clearly demonstrates that ECT is unmatched in its speed of action and efficacy [7]. The need for a better-tolerated but highly effective treatment is clear. Fortunately, variations in ECT technique can lower its side effects substantially, without sacrificing efficacy [22-24].

Over the years, various improvements in ECT technique have lowered its risk of side effects while preserving efficacy, demonstrating that efficacy and side effects are not inextricably linked as was the older dogma [25]. Modifications in ECT technique that resulted in lowered side effects include: (1) pulse shape – the shift from sine wave to rectangular pulses [26-28] and the shift from brief to ultrabrief pulse width [29, 30], (2) electrode placement – the introduction of right unilateral (RUL) [31, 32] and bifrontal (BF) electrode placement [33], and (3) individualization of dosage – with age-based dosing [34] and dosing the number of pulses relative to individual ST [35]. Randomized controlled trials demonstrate that these innovations (pulse shape [36] electrode placement [23] and individualization of dosage [37]) play a major role in determining the efficacy and side effects of seizure therapy. As shown in Figure 1.1, RUL ECT induces less amnesia than BL, but the efficacy of RUL ECT matches that of BL ECT when the dosage is given at 500% above the seizure threshold [37]. Increasing the dosage of RUL from 50% to 500% above the ST increased its efficacy while not substantially increasing its side effects [37]. Likewise, we found that reducing the width of the ECT pulse from 1.5 ms to 0.3 ms dramatically reduced its side effects, but efficacy was preserved when given at 500% above ST for RUL ECT [36]. Of note, each of these memory-sparing innovations was associated with greater efficiency in seizure induction. Specifically, ST is lower with RUL vs. BL [37], and with ultrabrief vs. brief pulse width (PW) [36]. These observations support the conclusion that modifying treatment parameters can reduce side effects, and suggest that improving the efficiency of stimulation parameters for seizure induction, and thereby reducing the stimulus dosage required to induce the seizure, improves tolerability. These findings highlight the importance of individualization of dosage and the complex interactions that can be seen among parameters. They also raise a number of unanswered questions about how best to individualize

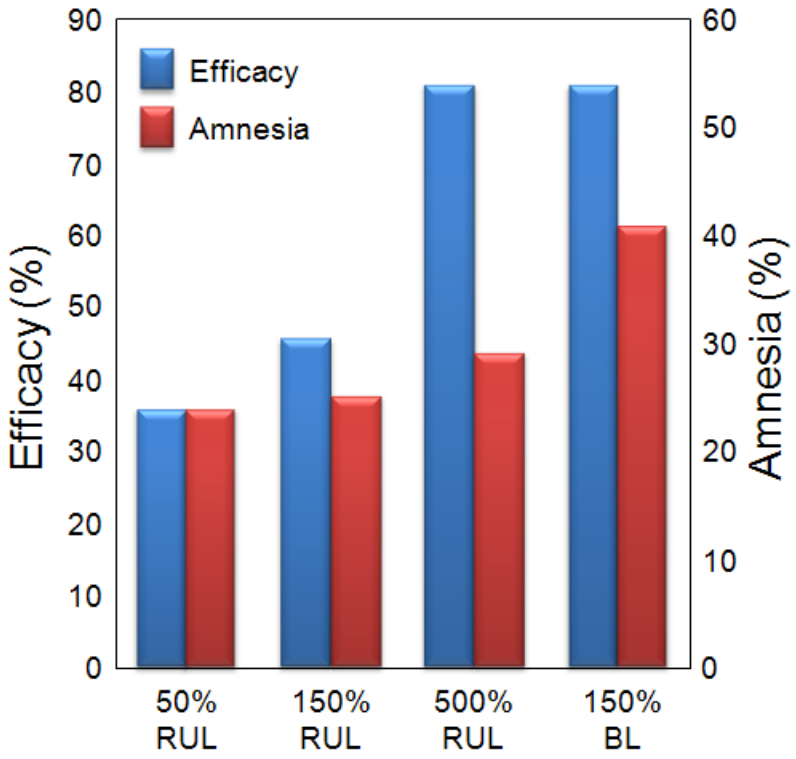

Figure 1.1. Efficacy and amnesia scores as a function of electrode placement and dosage relative to seizure threshold [38].

and optimize seizure therapies. Answering these questions requires knowledge of the biophysical principles relating stimulation parameters with clinical outcomes.

Despite mounting clinical evidence that dosage parameters interact in determining clinical outcomes, unanswered questions remain regarding the mechanisms by which variations in treatment technique lead to differences in antidepressant efficacy, cognitive side effects, and efficiency of seizure induction. A number of studies have attempted to understand the biophysical mechanisms of action of ECT/MST by manipulating stimulation parameters (e.g., electrode placement or stimulus current parameters). For instance, experimental electrode configurations including bifrontal (BF) [33] and focal electrically administered seizure therapy (FEAST) [39, 40] were developed to target prefrontal cortex and limiting spread to deeper

regions. However, their relative focalities have not been measured. It is posited that reducing the current amplitude required to induce the seizure (as with ultrabrief pulse width ECT and with MST) reduces side effects by virtue of enhanced physiological efficiency, but neural thresholds with ECT/MST configurations have not been studied [41]. Contrasting ECT/MST configurations that differ markedly in side effects, efficacy, and seizure threshold in their impact on the strength and focality of neural stimulation, could advance our understanding of the principles linking parameters with outcome, and provide a means of testing these theories. Such work is critically important since the parameter space that defines ECT/MST dosing is large to be systematically tested through of clinical trials. A mechanistic understanding can narrow the parameter space that needs to be tested clinically, and inform the optimization of seizure therapies which play such a vital role in TRD.

1.2.3. Magnetic Seizure Therapy

MST refers to the use of repetitive transcrnaial magnetic stimulation (rTMS) to induce a seizure for therapeutic purpose using rapidly alternating magnetic fields applied to the scalp. MST was designed to intentionally induce a series of generalized seizures under anesthesia. As a less invasive alternative to ECT, MST was developed with the goal of stimulating a more focal region of cerebral cortex by taking advantage of superior spatial precision of magnetic fields with the unparalleled antidepressant action of seizures. MST offers greater control of the induced electric field, since magnetic fields avoid the impedance of scalp and skull and induce the electric field confined to superficial cortex, facilitating focal seizure induction. A number of studies have demonstrated that MST can serve as a means of retaining antidepressant efficacy of

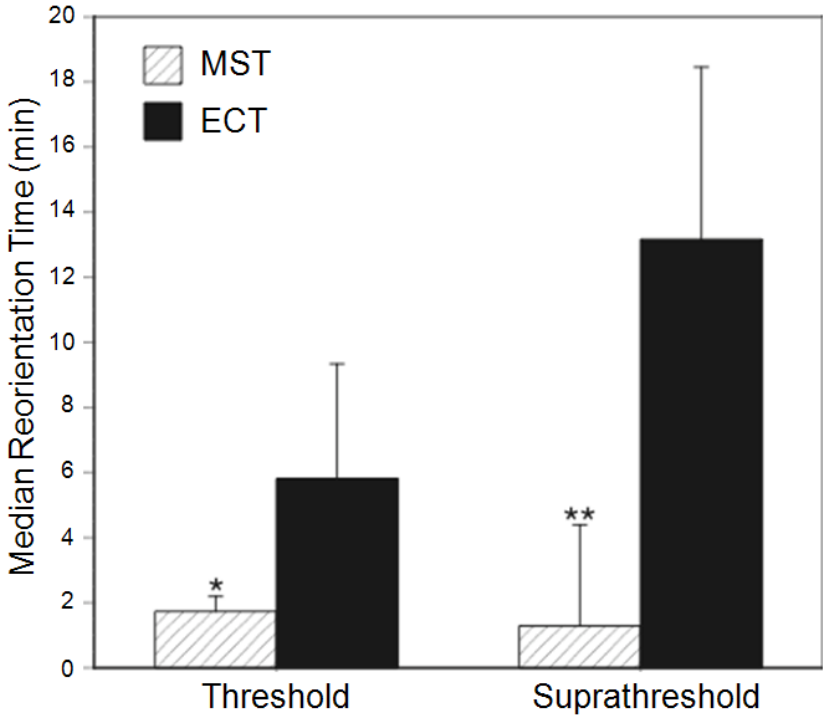

Figure 1.2. Faster reorientation following MST than ECT [1].

ECT with fewer cognitive side effects. For example, seizure induction with MST is feasible [42, 43]. MST-induced electric fields are weaker, more superficial, and less affected by variation of head tissue anatomy than those seen with ECT [44-46]. MST-induced current and the resulting seizures are more focal, weaker and less generalized than ECT [44, 47, 48]. MST offers a superior cognitive outcome profile than conventional ECT (Figure 1.2) [1, 49-51]. Our group has shown preliminary evidence of antidepressant benefits [43, 52, 53]. However, knowledge of MST dosing paradigms is still limited and its mechanisms are not completely understood for optimizing treatment parameters of seizure therapies and maximizing its antidepressant effects.

1.3. Approach

The conventional approach to device optimization that has been undertaken in the refinement of seizure therapies [Figure 1.3 (top)] has tested each stimulation paradigm in the context of clinical trials, sometimes with preclinical testing in animals as a precursor but often not. This process has led to significant innovations but has also been slow and costly. Even though MST employed translational studies in preclinical models prior to human testing, the impact of coil placement and pulse train frequency was first examined in clinical trials, which can be costly and expose patients to risks and the possibility of lack of benefit. We propose a rational approach [Figure 1.3 (bottom)] which includes multiple, iterative, high-throughput steps to refine the stimulation paradigm at the stage of *ex vivo* computational modeling (Chapter 2) and *in vivo* evaluation prior to testing safety and efficacy in clinical trials. This translational project couples a computational model (Chapter 2) with an animal model to address clinically salient questions about the rational dosing for seizure therapy. The intermediate steps between transcranial stimulation and clinical outcome can be examined by characterizing the induced electric fields (Chapters 3-7) and electric field strength relative to neural activation thresholds (Chapters 4-7). Computational models can yield essential information about the strength and distribution of the electric field induced in the brain by various ECT and MST paradigms (Chapters 4-7), yet such models have not been rigorously applied to the clinically important topic of seizure therapies. Animal models can then be used to physiologically calibrate the computational model to neural activation threshold and to determine the stimulation strength and focality of various ECT and MST paradigms (Chapters 4-7).

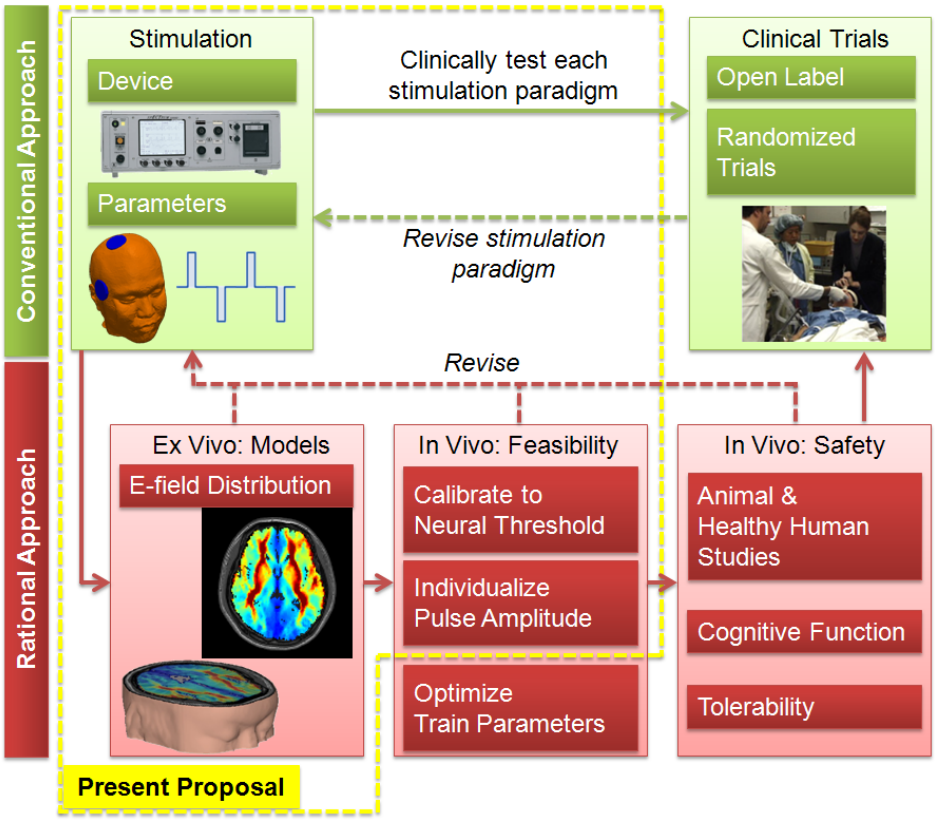

Figure 1.3. Top (green): Conventional approach to device optimization. Bottom (red): Rational approach, with multiple iterative revisions prior to clinical testing. Yellow dotted line: Scope of present proposal in this dissertation (figure courtesy of Drs. Lisanby and Peterchev, Duke University).

1.4. Thesis Overview

This dissertation can be organized into two main parts. Part I (see Chapter 2) presents a modeling framework for transcranial electric and magnetic stimulation.

Chapter 2 describes computational modeling methodology for transcranial brain stimulation that will be utilized in subsequent chapters. In this chapter, we develop anatomically realistic finite element head models of transcranial electric and magnetic stimulation in human

and nonhuman primates (NHPs) incorporating tissue heterogeneity and anisotropy derived from structural MRI and DTI data.

Part II (see Chapters 3-7) presents translational applications to electric and magnetic seizure therapy using the models developed in Part I.

Chapter 3 investigates the electric field strength generated by various ECT electrode configurations in specific brain regions of interest (ROIs) that have putative roles in the therapeutic action and/or adverse side effects of ECT. This chapter also characterizes the impact of the white matter conductivity anisotropy on the electric field distribution.

Chapter 4 examines the characteristics of the electric field induced in the brain by various ECT electrode and MST coil configurations. We compute the maps of the electric field strength relative to an estimated neural activation threshold, and used them to evaluate the suprathreshold direct stimulation strength and volume (focality) of the various ECT and MST paradigms.

Chapter 5 computes the spatial distributions of the electric field induced by right unilateral (RUL) ECT/transcranial electric stimulation (TES) in four NHP heads and investigates the influence of anatomical differences on the electric field strength in the brain across multiple subjects at a fixed TES current amplitude. This chapter also derives the neural activation threshold by coupling the simulated electric field strength with individually-titrated RUL TES motor threshold (MT) and shows that individual anatomical variability as captured by structural MRI and the electric field model predicts individual differences in TES MT.

Chapter 6 investigates the characteristics of the electric field induced in the brain by ECT with individualized current amplitude in the NHP models. In this chapter, we generate the maps of the electric field strength relative to an empirical neural activation threshold and determine the stimulation strength and focality of the various ECT electrode configurations with individualized

current amplitude corresponding to amplitude-titrated seizure threshold (ST) assessed in the anesthetized NHPs. This chapter examines the impact of individualizing and reducing current amplitude on the strength and distributions of the electric field induced by various ECT paradigms.

Chapter 7 examines the characteristics of the electric field induced in the brain by MST with individualized current amplitude in the NHP models. In this chapter, we compute the spatial distributions of the electric field induced by a cap (CAP) MST coil configuration in anatomically realistic NHP computational models. This chapter also aims to derive the neural activation threshold by coupling the simulated electric field strength in the motor cortex with individually-titrated MST MT. We create the maps of the electric field strength relative to the neural activation threshold and determine the electric field stimulation strength and focality of CAP MST with individualized current amplitude corresponding to amplitude-titrated ST. This chapter also investigates the impact of individualizing and reducing current amplitude on the stimulated brain volume.

Chapter 8 summarizes the contributions of this dissertation and suggests directions for future research.

Earlier, partial versions of the material in this thesis have been published: Chapter 2 is based on work published in [54-58]; Chapter 3 has been published in [54-56]; Chapter 4 is based on work published in [59]; Chapter 5 has been published in [60]; Chapter 6 is based on work published in [61, 62].

Part I

Modeling Framework for Transcranial Electric and Magnetic Stimulation

Chapter 2

Computational Modeling of Transcranial Brain Stimulation

The steps of the electric field modeling and analysis for the human and NHP subjects are diagrammed in Figures 2.1 and 2.2, respectively, and described in detail below.

2.1. MRI and Diffusion Tensor MRI Data Acquisition

2.1.1. Human

To construct an individual volume model of the head, T1-weighted MRI and diffusion weighted MRI data sets of a healthy subject (28 year old male) were acquired with a 3 T MRI scanner (Magnum 3.0, Medinus Inc., Republic of Korea). The MRI images captured the head above the level of the auditory canal, including the complete brain. The T1-weighted structural MRI data

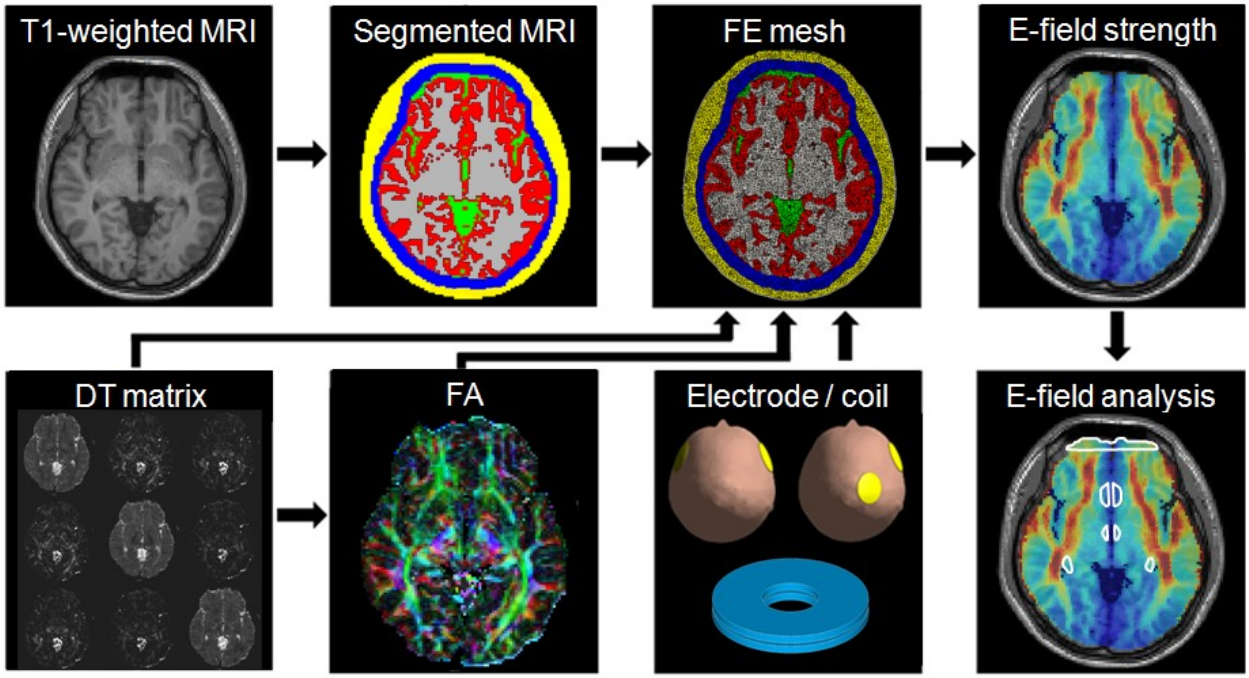

Figure 2.1. Schematic illustration of the methods for generating a realistic finite element (FE) model of the *human* head incorporating white matter (WM) anisotropic conductivity for electric field simulation and analysis in specific brain regions of interest (ROIs). T1-weighted MRI and diffusion-weighted MRI data sets of the subject are acquired. The T1-weighted MRI images are segmented into various tissues types: example segmentation of the human head shows the five tissues—scalp (yellow), skull (blue), cerebrospinal fluid (CSF, green), gray matter (red), and WM (gray). A diffusion tensor (DT) matrix and a fractional anisotropy (FA) map are computed from the diffusion-weighted MRI data. The color-coded FA map represents the principal orientations (largest eigenvectors) of the tensors (red: left-right, green: anterior-posterior, and blue: superior-inferior). ECT electrodes and MST coil are rendered with computer-aided design (CAD) tools and added to the head model. The composite 3-D models of transcranial electric and magnetic stimulation are adaptively discretized into FE meshes, and the electric field distribution is calculated using the FE method. The electric field is then analyzed both globally and in specific brain ROIs. ROI outlines in white from top to bottom show frontal pole, subcallosal cingulate cortex (SCC), hypothalamus, and hippocampus.

were obtained using a standard anatomical MR imaging sequence (TR = 35 ms; TE = 7 ms; 180 slices; 1×1×1 mm^3 voxel; FOV = 256 mm). The diffusion weighted MRI data were acquired using a single-shot spin-echo echo-planar imaging sequence (TR = 8280 ms; TE = 70 ms; 70 contiguous slices; 1.75×1.75×2 mm^3 voxel; 2 averages). The diffusion sensitizing gradients with a b-value of 600 s/mm^2 were applied in 45 non-collinear directions. The diffusion weighted images were corrected to remove eddy current and subject motion artifacts. We then computed the diffusion tensor for each voxel of the DT-MRI data set based upon a mono-exponential relationship between the signal attenuation and the diffusion tensor matrix [63, 64].

T1-weighted structural MRI and DTI datasets of one healthy human subject, including the skull base and a portion of the neck underneath, was acquired on a 3T Philips Achieva scanner (Philips Medical Systems, Best, Netherlands) using an 8-channel head coil, since existing human MRI data was only acquired for the portion of the head above the level of the auditory canal. The truncated head model eliminates shunting of the stimulus current in the lower portion of the head. The T1-weighted MRI images were acquired with a 3D spoiled gradient recalled echo (SPGR) (TR=6.5 ms; TE=3.0 ms; 256 coronal slices; 1×1×1 mm^3 voxel; FA=8º; 2 averages). The DTI data was also acquired by employing a single-shot spin-echo echo-planar imaging (EPI) sequence (TR=13510 ms; TE=70 ms; 112×112 acquisition matrix; FA=90º; 2×2×2 mm^3 voxel). The diffusion sensitizing gradients with a b-value of 1000 s/mm^2 were applied in 32 non-collinear directions. The whole head MRI and DTI data sets were utilized to construct an anatomically realistic computational model of the human head.

2.1.2. Nonhuman Primates

All studies were approved by the Institutional Animal Care and Use Committees (IACUC) of New York State Psychiatric Institute, Columbia University, and Duke University. T1-weighted MRI and diffusion-weighted imaging (DWI) data sets of four healthy male rhesus macaques (*Macaca mulatta*) (age=12–18 years; weight=8.4–10.7 kg) were acquired on a Siemens 3T Trio scanner (Siemens, Erlangen, Germany) using an 8-channel knee coil. The NHPs were sedated with a combination of ketamine HCl (3 mg/kg body wt. IM) and dexdomitor (0.075 mg/kg to 0.15 mg/kg body wt. IM) and transported to the MRI unit in approved transport cages. Prior to MRI scanning, the NHPs were intubated with a 4 mm to 5 mm tube for administration of isoflurane gas anesthesia (0.5% to 3%). The NHPs were oriented in a sphinx position with the head forward and were continuously monitored by an Invivo (Essential) MRI-compatible patient monitor. Vital signs monitored included heart rate and blood oxygenation (SpO2). The T1-weighted MRI images were acquired with a 3D magnetization prepared rapid gradient echo (MPRAGE) sequence (TR=2300 ms; TE=4.4 ms; TI=1100 ms; 256 coronal slices; 0.7×0.7×0.7 mm^3 voxel; FA=8º; 2 averages). The DWI data were acquired by employing a single-shot spin-echo echo-planar imaging (EPI) sequence (TR=13000 ms; TE=81 ms; 128×128 matrix; 1.4×1.4×1.4 mm^3 voxel; interleaved acquisition; pixel bandwidth=1346 Hz). The diffusion sensitizing gradients with a b-value of 1000 s/mm^2 were applied in 12 non-collinear directions. Six image volumes with non-diffusion weighting (b=0 s/mm^2) were also acquired as reference images. A twice-refocused technique was used to minimize eddy current effects induced by strong diffusion-weighting gradients [65]. The generalized autocalibrating partially parallel acquisitions (GRAPPA) parallel imaging scheme with an acceleration factor of 2 was applied to reduce susceptibility artifacts and to improve the SNR [66]. A partial Fourier algorithm of a

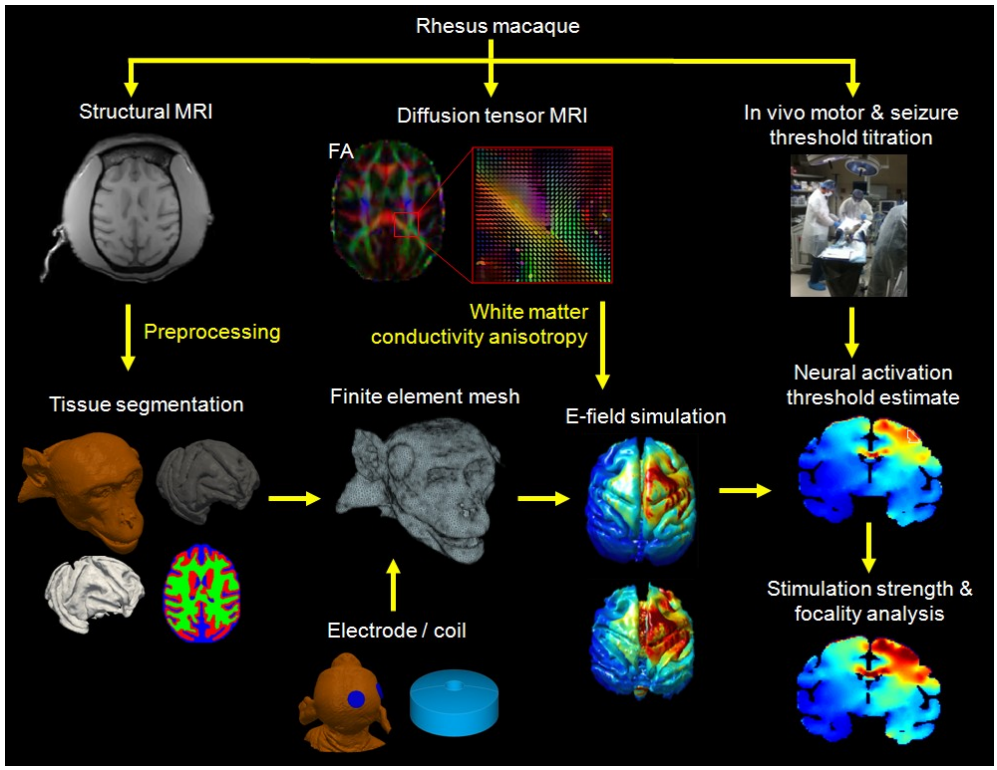

Figure 2.1. Overview of the workflow for generating a realistic finite element (FE) model in nonhuman primates (NHPs) for electric field computation and combining it with *in vivo* motor and seizure threshold to estimate neural activation threshold and to determine electric field stimulation strength and focality. T1-weighted MRI and diffusion-tensor MRI data sets of the NHP subjects are acquired. The T1-weighted MRI images are segmented into 14 tissues: example segmentation of the rhesus macaque head shows 3-D surface renderings of skin (brown), gray matter (dark gray), and white matter (light gray), and 2-D masks of cerebrospinal fluid (CSF, blue), gray matter (red), and WM (green). The color-coded fractional anisotropy (FA) map and diffusion tensor ellipsoids (enlarged view of the region framed in red) represent the principal orientations (largest eigenvectors) of the tensors using the color convention defined in Figure 2.1. ECT electrodes and MST coil are incorporated into the head model. The complete 3-D ECT or MST models are adaptively discretized into FE meshes, and the electric field distribution is computed using the FE method. Motor threshold is titrated *in vivo* by the current amplitude of single stimulus pulses. Neural activation threshold is estimated by extracting the simulated electric field strength in the target motor area at the empirical motor threshold current. Electric field stimulation strength and focality relative to neural activation threshold of the various ECT and MST paradigms are analyzed.

factor of 0.75 was used to reduce the EPI echo train length, which further ameliorated geometric distortion [67]. DWI acquisition was repeated six times and averaged to increase the SNR.

2.2. Image Processing

2.2.1. Preprocessing

We extracted the human and NHP head regions from the background noise and artifacts in the T1-weighted MRI data set by applying a morphological processing technique that included thresholding, opening and closing of the head binary masks [68]. The preprocessing of the extracted head MRI volume was performed based on the open source software components available within 3D Slicer 4.0 (http://www.slicer.org/) and in-house image processing algorithm [68]. The head MRI images were spatially oriented along manually-defined anatomical landmarks, corresponding to anterior commissure (AC), posterior commissure (PC), and fiducials for inter-hemispheral midline, so that AC-PC line was perpendicular to the coronal plane, and the midline plane was aligned with the sagittal plane. The MRI image intensities were corrected for bias field inhomogeneity using improved N3 bias correction algorithm [69].

2.2.2. Gradient Vector Flow Nonlinear Anisotropic Diffusion

It is of particular importance to remove undesirable properties of given MRI images such as noise and artifacts. Besides, pre-segmentation of image structures is critical to simplify the

structures of the MRI images for enhanced tissue segmentation [70]. Content-preserving anisotropic diffusion provides such pre-segmentation of the MRI volume and improvement of the MRI image quality. In this study, we applied 3-D gradient vector flow (GVF) anisotropic diffusion filtering algorithm in order to remove the image noise while preserving content details and enhancing tissue boundaries [71].

The GVF nonlinear diffusion was proven to be much more robust than conventional Structure tensor-based anisotropic diffusion algorithm [72], and is summarized here.

The GVF as a 3-D vector field can be defined as:

$$\mathbf{V}(i,j,k) = (\mathbf{u}(i,j,k), \mathbf{v}(i,j,k), \mathbf{w}(i,j,k)) \tag{2.1}$$

The field can be obtained by minimizing the energy functional:

$$\begin{aligned} \varepsilon &= \iiint \gamma(\eta_{\mathbf{u}} + \eta_{\mathbf{v}} + \eta_{\mathbf{w}}) + |\nabla f|^2 |\mathbf{V} - \nabla f|^2 \partial x \partial y \partial z \\ \eta_{\mathbf{u}} &= \mathbf{u}_x^2 + \mathbf{u}_y^2 + \mathbf{u}_z^2 \\ \eta_{\mathbf{v}} &= \mathbf{v}_x^2 + \mathbf{v}_y^2 + \mathbf{v}_z^2 \\ \eta_{\mathbf{w}} &= \mathbf{w}_x^2 + \mathbf{w}_y^2 + \mathbf{w}_z^2 \end{aligned} \tag{2.2}$$

where f is an image edge map and γ is a noise control parameter.

For 3-D anisotropic smoothing, the Structure tensor $\mathbf{S}$ is formed with the components of $\mathbf{V}$

$$\mathbf{S} = \begin{bmatrix} I_x^2(i,j) & I_x I_y(i,j) \\ I_y I_x(i,j) & I_y^2(i,j) \end{bmatrix} \tag{2.3}$$

$$\mathbf{S} = \mathbf{V}(\mathbf{V})^T \tag{2.4}$$

where I is an image, i and j are image indices, x and y denote partial derivatives in space.

The 3-D anisotropic regularization is governed using the GVF diffusion tensor $\mathbf{D}_{\mathrm{GVF}}$ which is constructed with eigen components of $\mathbf{S}$.

$$\partial J / \partial t = div[\mathbf{D}_{GVF} \nabla J], \quad (2.5)$$

where J is an image volume in 3-D. The regularization behavior of (2.4) is controlled with the eigenvalue analysis of the GVF Structure tensor [70, 73].

2.3. Tissue Segmentation

2.3.1. Human

To generate a realistic volume conductor model of the head, the various distinct tissues have to be mapped, since they have different electrical properties. Segmentation involves creating 3-D masks that correspond to each tissue layer of the head. The structural MRI images were segmented into several tissue regions (see Table 2.1). We first removed non-brain regions using the skull-stripping algorithm BET tool [74] in FSL (FMRIB Analysis Group, University of Oxford, UK, http://fsl.fmrib.ox.ac.uk/fsl/fslwiki). This initial segmentation was further corrected for accurate brain extraction using manual editing tools in the ITK-SNAP software [75]. The de-skulled MRI images were automatically segmented into partial volume images corresponding to gray matter, white matter, and cerebrospinal fluid (CSF) using an automated segmentation tool FAST in FSL. We then segmented non-brain regions into 11 different tissue regions, including skin, muscle, skull compacta, skull spongiosa, vertebrae, spinal cord, lens, eyeball, sclera, optic nerve, and sinus, using a combination of segmentation editing tools from the ITK-SNAP software and an in-house segmentation algorithm based on thresholding and mathematical morphological operations [12, 14].

2.3.2. Nonhuman Primates

The implementation for tissue segmentation described in Chapter 2.3.1 has been developed and fine-tuned for the human brain. Since the NHP brain has relatively smaller brain sizes and somewhat different brain anatomy than human, the segmentation tools for human MRI brain scans are not well adapted for segmentation of the NHP brain segmentation. As such, we implemented an automatic algorithm that uses the unified segmentation routines [76] implemented in SPM8 (Wellcome Department of Cognitive Neurology, Institute of Neurology, University College London, UK, http://www.fil.ion.ucl.ac.uk/spm) to produce probability tissue maps that define the probability of occurrences of a given tissue for each voxel of the image. The de-skulled NHP MRI images were segmented into tissue probability images in native space corresponding to gray matter, white matter, and cerebrospinal fluid (CSF) based on the 112RM-SL macaque tissue priors [77]. In this process, the unified segmentation approach uses an objective cost function integrating the prior tissue probabilities, a mixture of Gaussians, and a registration term [76]. Instead of the default settings in the "Segment" tool in SPM8, our algorithm utilized user-defined parameter settings: (i) human tissue priors (ICBM452 T1-weighted average) were replaced by the 112RM-SL macaque tissue priors [77]; (ii) affine regularization was changed to "Average sized template"; (iii) sampling distance was reduced to 2 mm [78]. Manual segmentation of the non-brain regions into 11 tissue compartments, representing skin, muscle, skull spongiosa, skull compacta, vertebrae, spinal cord, lens, eyeball, sclera, optic nerve, and sinus, was carried out using a combination of segmentation editing tools from the ITK-SNAP software [75] and an in-house morphological algorithm [12, 14].

2.4. Electrode and Coil Modeling

2.4.1. ECT Electrode Configurations

To model transcranial electric stimulation, 3-D CAD renderings of the ECT electrodes have to be added at the appropriate positions on the head representation. We added realistically-shaped ECT electrodes to the 3-D head model by intersecting cylindrical or rectangular solid geometries with the head rendering. We modeled three conventional electrode placements (BL, BF, and RUL) [79, 80] and two investigational configurations (FEAST and FM) [81, 82] diagrammed in Figure 2.1. Standard round electrodes (5 cm diameter) for the BL, BF, RUL, and FM ECT electrode configurations were modeled for the human models. Two round electrodes for the BL (3.5 cm diameter) and BF, RUL, and FM ECT (2.5 cm diameter, respectively) configurations were modeled for the NHP models.

For BL ECT, the two electrodes were centered bilaterally at the frontotemporal positions above the midpoint of the line connecting the external canthus and tragus (APA, 2001). For BF ECT, the electrodes were placed bilaterally above the outer angle of the orbit on a line parallel to the sagittal plane (Abrams, 2002). For RUL ECT, one electrode was centered to the right of vertex and the second electrode was placed in the homologous right frontotemporal position (APA, 2001). For FEAST, a wide rectangular electrode (2.5 cm × 6.3 cm) was placed over the right motor strip and a small circular electrode (2 cm diameter) was placed over the right eyebrow. For human FM ECT, one electrode was placed medially on the forehead and the second electrode was placed in front of vertex. For NHP FM ECT, the two electrodes were placed medially on the forehead and posterior to vertex, respectively. Since the conductivity of the steel electrodes is more than five orders of magnitude higher than that of the scalp (see

Chapter 2.6), the electrode surface is effectively equipotential for any practical electrode thickness. Therefore, we did not accurately model the electrode thickness but, for simplicity, kept the outer surface of the electrodes flat, resulting in the electrode thickness between the flat outer surface and the scalp curvature varying from 5 mm to 12 mm. The electrode wires were modeled as current sources respectively sourcing and sinking current in the centers of the outer electrode surface, reflecting the wiring of conventional ECT electrode paddles, even though the high conductivity and the resulting equipotential surface of the electrodes make inconsequential the exact point of injection of current from the wires to the electrodes. Finally, we did not model the electrolyte gel applied to the ECT electrode surface, since the gel's purpose is to stabilize the impedance of the electrode–scalp interface, which is already assumed in the computational model, and since the gel is largely displaced when the electrodes are pressed against the head.

2.4.2. MST Coil Configurations

To model transcranial magnetic stimulation, 3-D CAD renderings of the MST coils have to be integrated with the head models. MST coils consist of copper wire windings covered with layers of high-voltage insulation [83, 84]. The shape of the windings has a key role in determining the distribution of the induced electric field. 3-D CAD drawings of the coils were created in ANSYS (ANSYS Inc., Canonsburg, PA), then were integrated with the head models. The distance between the windings and the head was set to account for the thickness of the insulation [85, 86]. The coil model was validated by comparing the simulated coil inductances to the actual inductances measured with an LCR meter (Model 889A, B&K Precision Corp., Yorba Linda, CA).

For the human models, we modeled a circular coil on vertex (CIRC) MST coil (S/N MP39, Magstim Co, Whiteland, Wales, UK) configuration using manufacturer's data and inductance measurements, selected because it has been used in clinical studies. The CIRC coil consists of two parallel layers of windings connected in series, each with an inner diameter of 44 mm, outer diameter of 120 mm, and 9 turns. The coil conductors were placed above the vertex of the human head model.

For the NHP models, the cap (CAP) MST coil (MagVenture A/S, Farum, Denmark) configuration was modeled using manufacturer's data and inductance measurements, selected because it has been used in preclinical studies. The CAP coil consists of a single-layer, concave circular winding with an inner diameter of 21 mm, outer diameter of 95 mm, and 15 turns. The coil conductors were placed above the vertex of the NHP head models.

2.5. Finite Element Mesh Generation

Once the volumes defining the head tissues and the ECT electrodes and MST coils are rendered, they have to be discretized into a large number of smaller subvolumes (finite elements, FEs) resulting in a 3-D mesh model used to solve the electric field with FEM. For the FE mesh generation, we utilized the Computer Geometry Algorithm Library (CGAL) (http://www.cgal.org). The mesh generator is based on the labeled voxel-volume meshing technique [87] and allows generation of FE tetrahedral meshes which contain one sub-mesh for each sub-domain and surface meshes that approximate the boundaries of the domain and sub-domain. The triangulation algorithm provides a discretized approximation of tissue compartments and their surface boundaries according to the restricted Delaunay triangulation

paradigm [87, 88], resulting in 3-D meshes of each tissue domain and conformal surface meshes for all tissue boundaries and subdividing surfaces.

2.6. Tissue Properties

The physical properties of biological tissues that are relevant to the electric field induced by electric and magnetic stimulation are the conductivity and permittivity. Permeability in biological tissues does not significantly deviate from that of free space. Tissue electrical conductivities were derived from the literature. The permittivity of tissues was assumed to be zero, consistent with the quasistatic approximation discussed in Chapter 2.7. Since the high anisotropy of WM can significantly distort the electric field relative to a model assuming isotropic WM conductivity, we created volume conductor head models by assigning anisotropic electrical conductivities to the white matter compartment, and isotropic conductivities to all other tissue regions. The isotropic electrical conductivities (in S/m) are given in Table 2.1 [68, 89-91].

The estimation of the anisotropic conductivity tensors in the white matter started with preprocessing of the raw DWI head data. The DWI data were processed using FSL's diffusion toolbox (FDT) from the FMRIB Software Library. Artifacts and spatial distortions due to eddy current effects caused by strong diffusion gradients used in the EPI sequence and possible head motion were corrected by performing an affine registration between diffusion-weighted images and non-diffusion-weighted images. For the human and NHP DWI data sets, the diffusion-weighted volumes of each subject were coregistered to the non-diffusion-weighted volume, which was used as the reference volume. A binary brain mask was extracted from the volume with non-diffusion weighting in diffusion space using FSL's BET tool. The segmentation errors

resulting from the automated segmentation algorithm were further corrected to ensure that we only reconstructed diffusion tensors inside the brain rather than the surrounding air. We then computed the diffusion tensors for each voxel of the preprocessed DWI datasets [64]. The resulting diffusion tensor volumes were coregistered to the structural T1-weighted MRI volume using an affine registration with mutual information as the cost function while the orientation of each diffusion tensor was preserved [92].

To estimate the WM anisotropic conductivity tensors, we used the assumption that the conductivity tensors share eigenvectors with the measured diffusion tensors [63, 64]. We deployed the volume constraint approach to estimate the WM anisotropic conductivity with a fixed anisotropy ratio in each WM voxel [90]. The WM anisotropic conductivity tensor σ_{WM} was modeled to be prolate

$$\sigma_{\mathrm{WM}} = \mathbf{S}\ \mathrm{diag}\left(\sigma_{\mathrm{long}}, \sigma_{\mathrm{trans}}, \sigma_{\mathrm{trans}}\right)\ \mathbf{S}^{-1} \tag{2.6}$$

where **S** denotes the orthogonal matrix of unit length eigenvectors of the measured DTs at the barycenter of the WM tetrahedral elements. Parameters σ_{long} and σ_{trans} are the conductivity eigenvalues longitudinal (parallel) and transverse (perpendicular) to the WM fiber direction, respectively, with $\sigma_{\mathrm{long}} \geq \sigma_{\mathrm{trans}}$. We computed σ_{long} and σ_{trans} from the WM isotropic conductivity value of σ_{iso} = 0.14 S/m and the anisotropic factor *k* [90, 93]

$$\sigma_{\mathrm{long}} = \sigma_{\mathrm{iso}} k^{2/3} \tag{2.7}$$

$$\sigma_{\mathrm{trans}} = \sigma_{\mathrm{iso}} k^{-1/3}. \tag{2.8}$$

Another alternative is the volume normalization approach to derive variable white matter anisotropic electrical conductivity tensors using a linear conductivity-to-diffusivity relationship based on the effective medium approach in conjunction with the volume constraint algorithm.

The electrical conductivity tensors σ in the white matter were computed from the measured diffusion tensors *D* and the isotropic white matter conductivity σ_{iso} from the literature using the volume normalized algorithm [57, 93-97]: in each voxel, the diffusion tensor is linearly scaled so that the volume of the resulting conductivity tensor ellipsoid matches that of an isotropic conductivity tensor sphere with radius σ_{iso}

$$\sigma = \frac{\sigma_{iso}}{\sqrt[3]{d_1 \cdot d_2 \cdot d_3}} D \tag{2.9}$$

where d_i are the diffusion tensor eigenvalues. This approach preserves the orientation (eigenvectors) and anisotropy ratios (eigenvalue ratios) of the diffusion tensors.

Table 2.1. Tissue electrical conductivities (S/m)

Tissue	Conductivity	Tissue	Conductivity
Skin	0.43	Lens	0.32
Muscle	0.32	Eyeball	0.5
Skull compacta	0.0063	Sclera	0.5
Skull spongiosa	0.04	Spinal cord	0.15
Cerebrospinal fluid	1.79	Vertebrae	0.012
Gray matter	0.33	Optic nerve	0.14
White matter (iso.)	0.14	Sinus	0
Steel electrode	9.8×10^{5}	Air	1×10^{-15}

2.7. Electric Field Simulation

2.7.1. Theoretical Background

Since the current waveform frequencies in ECT and MST are relatively low (< 10 kHz), electromagnetic field solutions can be obtained by solving the quasi-static Maxwell's equations. This quasi-static approximation involves neglecting wave propagation, inductive and capacitive effects in the conductive medium. This means that the electric field varies with no significant phase differences and the effect of the magnetic field generated by the currents in the tissue can be ignored. The tissue is also considered as a purely resistive medium [98].

In the conductive medium, considering static and dynamic fields and neglecting displacement currents, the following subset of Maxwell's equations apply [99, 100]:

$$\nabla \times \frac{1}{\mu} \vec{B} = -\sigma \vec{E} \tag{2.10}$$

$$\nabla \times \vec{E} = -\frac{\partial \vec{B}}{\partial t} \tag{2.11}$$

$$\nabla \cdot \vec{B} = 0 \tag{2.12}$$

where μ is the tissue permittivity, $\vec{B}$ is the magnetic flux density, σ is the tissue electrical conductivity, and $\vec{E}$ is the electric field.

In the air, the Ampere equation relates the magnetic field $\vec{H}$ with the current density

$$\nabla \times \vec{H} = \vec{J}_s \tag{2.13}$$

$$\nabla \cdot \vec{B} = 0 \tag{2.14}$$

where $\vec{H}$ is the magnetic field intensity and $\vec{J}_s$ is the current density in the simulating coil.

At the exterior boundary of the air model,

$$\vec{B} \cdot \vec{n} = 0 \tag{2.15}$$

which indicates that the normal component of the magnetic flux density is zero at infinity. $\vec{n}$ is a unit vector normal to the surface.

By introducing the electric scalar potential V and magnetic vector potential $\vec{A}$, the magnetic field $\vec{B}$ and electric field $\vec{E}$ can be expressed as follows:

$$\vec{B} = \nabla \times \vec{A} \tag{2.16}$$

$$\vec{E} = -\frac{\partial \vec{A}}{\partial t} - \nabla V \tag{2.17}$$

In the quasi-static limit, the divergence of the induced current density is equal to zero. Then, equations (2.10)-(2.15) can be transformed as follows: in the head,

$$\nabla \times \frac{1}{\mu_0} \nabla \times \vec{A} + \sigma \frac{\partial \vec{A}}{\partial t} + \sigma \nabla V = 0 \tag{2.18}$$

$$\nabla \left(-\sigma \frac{\partial \vec{A}}{\partial t} - \sigma \nabla V \right) = 0 \tag{2.19}$$

At the interface between two regions with different conductivities, the boundary condition follows the continuity of current

$$J_1 \cdot \vec{n}_1 = J_2 \cdot \vec{n}_2 \tag{2.20}$$

In the air,

$$\nabla \times \frac{1}{\mu_0} \nabla \times \vec{A} = \vec{J}_s \tag{2.21}$$

At the air and tissue boundary, the current density normal to the interface is equal to zero and so the scalar potential V must satisfy the boundary conduction

$$(\sigma \nabla V) \cdot \vec{n} = -\left(\sigma \frac{\partial \vec{A}}{\partial t} \right) \cdot \vec{n} \tag{2.22}$$

At the exterior boundary of the air model,

$$\vec{n} \times \vec{A} = 0 \tag{2.23}$$

which indicates that the magnetic field is approximately zero at the model boundary.

Equations (2.18)-(2.23) can be solved in combination with coulomb's gauge

$$\nabla \cdot \vec{A} = 0 \tag{2.24}$$

2.7.2. Harmonic Analysis Using Complex Formalism

In a general dynamic problem, any field quantity, $q(r, t)$ depends on the space r and time t variables. In a harmonic analysis, the time dependence can be expressed by periodic function [101]:

$$q(r,t) = a(r)\cos(\omega t + \varphi(r)) = c(r)\cos(\omega t) - s(r)\sin(wt) \tag{2.25}$$

where ω is the angular frequency of time change, $a(r)$ is the peak amplitude, $\varphi(r)$ is the phase angel, $c(r)$ is measurable field at $\omega t = 0$ degrees, and $s(r)$ is measurable field at $\omega t = -90$ degrees.

The quantities in equations (2.25) are related by

$$c(r) = a(r)\cos(\varphi(r)) \tag{2.26}$$

$$c(r) = a(r)\cos(\varphi(r)) \tag{2.27}$$

$$s(r) = a(r)\sin(\varphi(r)) \tag{2.28}$$

$$a^2(r) = c^2(r) + s^2(r) \tag{2.29}$$

$$\tan(\varphi(r)) = \frac{s(r)}{c(r)} \tag{2.30}$$

In equation (2.25), $a(r)$, $\varphi(r)$, $c(r)$, and $s(r)$ depend on space *r*, independent of time *t*. This separation of variables, space *r* and time *t*, enables us to reduce four (3 space and 1 time) dimensional real problem to a three (space) dimensional complex problem. This can be solved by the complex formalism.

The measurable quantity, $q(r, t)$ can be expressed as the real part of a complex function:

$$q(r,t) = \mathrm{Re}\{Q(r)e^{jwt}\} \tag{2.31}$$

$$Q(r) = Q_r(r) + jQ_i(r) \tag{2.32}$$

where *j* is the imaginary unit, $\mathrm{Re}\{\}$ denotes the real part of a complex quantity. $Q_r(r)$ and $Q_i(r)$ are the real and imaginary parts of $Q(r)$.

The complex exponential function in equation (2.31) can be expressed by sine and cosine functions as

$$e^{jwt} = \cos(\omega t) + j\sin(\omega t) \tag{2.33}$$

Substituting equation (2.33) into equation (2.31) provides equation (2.32)

$$q(r,t) = Q_r(r)\cos(\omega t) - Q_i(r)\sin(\omega t) \tag{2.34}$$

By comparing equation (2.25) with equation (2.34),

$$c(r) = Q_r(r) \tag{2.35}$$

$$s(r) = Q_i(r) \tag{2.36}$$

The complex real part $Q_r(r)$ and imaginary part $Q_i(r)$ are equal to the measurable cosine $c(r)$ and sine function $s(r)$, respectively.

A harmonic analysis provides the real and imaginary components of a complex solution. The magnitude of the real and imaginary parts describe the measurable field at t=0 and at ωt = -90 degrees, respectively.

$$a(r)^2 = Q_r(r)^2 + Q_i(r)^2 \tag{2.37}$$

$$\tan(\varphi(r)) = \frac{Q_r(r)}{Q_i(r)} \tag{2.38}$$

Equation (2.37) expresses the peak amplitude and phase angle of the measurable harmonic field quantities by the complex real and imaginary components.

2.7.3. Quasistatic Electric Analysis

Neglecting the time-derivative of magnetic flux density under the quasi-static approximation, the electric field can be derived as follows [101]:

$$\vec{E} = -\nabla V \tag{2.39}$$

where V is the electric scalar potential.

The constitutive equations for the electric fields become

$$\vec{J} = \sigma\vec{E} \tag{2.40}$$

$$\vec{D} = \varepsilon\vec{E} \tag{2.41}$$

where σ is the electrical conductivity matrix, $\vec{D}$ is the electric flux density vector, and ε is the permittivity matrix.

In a quasi-static electric analysis, the relevant governing equations are equation (2.39) and the continuity equation

$$\nabla \cdot \left(\vec{J} + \frac{\partial \vec{D}}{\partial t} \right) = 0 \tag{2.42}$$

Substituting the constitutive equations (2.40) and (2.41) into equation (2.42), and taking into account equation (2.39), the following differential equation for the electrical scalar potential can be obtained

$$-\nabla\cdot(\sigma\nabla V)-\nabla\cdot\left(\varepsilon\nabla\frac{\partial V}{\partial t}\right)=0 \tag{2.43}$$

Neglecting time-variation of electric potential reduces the governing equation for steady-state electric conduction:

$$-\nabla\cdot(\sigma\nabla V)=0 \tag{2.44}$$

In a time-harmonic electric field analysis, equation (2.43) can be rewritten as

$$-\nabla\cdot(\varepsilon\nabla V)+\frac{j}{w}\nabla\cdot\left(\sigma\nabla V\right)=0 \tag{2.45}$$

where j is the imaginary unit and w is the angular frequency.

2.7.4. Electric Field Computation

The numerical solution of the electric field induced by electric and magnetic stimulation was computed with the FEM software packages ANSYS (ANSYS Inc., PA, USA). Since the current waveform frequencies used in ECT and MST are relatively low (< 10 kHz), we adopted the quasistatic approximation, as described in Sections 2.7.2 and 2.7.3, which essentially ignores the frequency dependence of the tissue impedance when solving the electric field [102-104].

For all ECT electrode configurations, the current was set to 800 mA, corresponding to the conventional setting used with the MECTA Spectrum 5000Q ECT device (MECTA Corp., OR, USA). The electric field was obtained by solving the quasi-static Laplace equation with no internal sources [103, 105, 106]

$$\nabla \cdot (\sigma \nabla V) = 0 \tag{2.46}$$

where V and σ are the electrical potential and the tissue conductivity tensor, respectively. The Neumann boundary conditions apply on the surface of the model

$$(\sigma \nabla V) \cdot \vec{n} = 0 \tag{2.47}$$

where $\vec{n}$ is the unit vector normal to the outer surface of the model, except at the outer centers of the electrodes where current is injected. For each of the electrode configurations, the system of linear equations of the FE method was solved using the preconditioned conjugate gradient solver with a relative tolerance of 10^{-8}. Finally, the electric field distribution was computed by taking the gradient of the scalar potential V.

For the MST coil configurations, a time-harmonic simulation with appropriate boundary conditions was first performed to compute the spatial electric field distribution generated by MST for an arbitrary coil voltage 1 V and frequency $\omega_0 = 2\pi \times 5$ kHz, resulting in electric field distribution with unadjusted amplitude, $E'(r)$. The electric field was then scaled to match the output of the Magstim Theta or MagPro device [86]:

$$E(r) = E'(r) \frac{V_c}{I \omega_0 L} \tag{2.48}$$

where V_c is the nominal energy-storage capacitor voltage at maximum pulse amplitude of the Magstim Theta (V_c = 1.65 kV) or MagPro (V_c = 1.8 kV) device. I is the coil current and L is the coil inductance.

Part II

Translational Applications to Electric and Magnetic Seizure Therapy

Chapter 3

Regional Electric Field Induced by Electroconvulsive Therapy

3.1. Introduction

Electroconvulsive therapy (ECT) is a therapeutic intervention in which electric current is applied through scalp electrodes to induce a generalized seizure in anesthetized patients [79, 80]. Although ECT plays a vital role in the treatment of medication-resistant psychiatric disorders, such as major depression, the use of ECT has been limited by its cognitive side effects (particularly amnesia [20, 107]), by cardiac complications [108], by the need for general anesthesia, as well as by the high rate of relapse [109]. Despite the introduction of various improvements of ECT technique, there is still limited knowledge of how to optimally select electrode placement [110] or stimulus current parameters [111] for maximal efficacy and tolerability. Indeed, the therapeutic action and adverse side effects of ECT are highly dependent upon electrode placement and stimulus current parameters, but a complete mechanistic explanation for these relationships is still lacking. For instance, right unilateral (RUL) ECT leads to fewer cognitive side effects than bilateral frontotemporal (BL) ECT [112], but it is not known

whether this is by virtue of lower electric field (E-field) strength in hippocampus and other regions crucial for memory. Furthermore, alternative ECT electrode configurations such as bifrontal (BF) [79] and focal electrically administered seizure therapy (FEAST) [81] have been proposed with the goal of preferentially targeting frontal brain regions to reduce memory impairment, but the frontal electric field strength relative to the rest of the brain and relative to other electrode placements has not been quantified.

To understand the underlying biophysical mechanisms of ECT, a few early studies undertook measurements of the electric field generated by ECT in human cadavers [113, 114] and in an electrolytic tank containing a human half-skull [115]. However, the electrolytic tank measurements did not account for the geometry and conductivity properties of the scalp and the brain. The intracerebral cadaver measurements were carried out after an uncontrolled interval of time following death, potentially resulting in altered conductivity profile of the head tissues, and the tissues were damaged in the process of inserting the recording probes, potentially altering the paths of current flow generated by the scalp electrodes. Furthermore, neither of the studies produced a high-resolution map of the electric field or the current density distributions in the brain.

In order to provide more detailed field maps, a number of computational studies have simulated the distribution of the electric field or the current density field (which equals the product of electric field and conductivity) in the brain using a volume conductor model of the head. The representation of the head in computational ECT models ranges in detail from concentric spheres [116-118] to low-resolution realistically-shaped representations [119-121] to high-resolution anatomically-accurate models [122, 123]. Furthermore, a substantial number of electric field/current density modeling studies have been published in the context of other

transcranial electric stimulation paradigms, again ranging from simplified to realistic head representations [91, 96, 115, 124-140]. However, these studies have various limitations. The spherical and simplified geometry models do not fully account for tissue inhomogeneity and anisotropy, and the complex geometries of head tissues, including orifices in the skull such as the auditory canals and the orbits. The published anatomically-accurate ECT models [122, 123] consider only isotropic tissue conductivity, explore only a limited set of electrode configurations (BL and RUL), and do not perform region of interest (ROI) analysis of the field distribution in the brain. The computational models of non-ECT transcranial electric stimulation offer some insights into the biophysics of the problem, but do not provide data specific to ECT electrode configurations and stimulus current parameters.

For realistic models of the electric field generated by ECT, the inclusion of anisotropic conductivity of the white matter (WM) may be of particular importance since the electric field induced by ECT is typically widespread and reaches deep brain regions [117, 122], and since depression itself is associated with regionally specific abnormalities of the WM fractional anisotropy [141, 142]. Our and other groups have previously incorporated tissue anisotropic conductivity in models of electroencephalography (EEG) and magnetoencephalography (MEG) [73, 90, 93-95, 97, 143-147], transcranial direct current stimulation (tDCS) [127, 135, 140, 148], deep brain stimulation [149], transcranial magnetic stimulation (TMS) [150, 151], and electrical impedance tomography [152]. These studies demonstrate that anisotropic conductivity of the brain tissue can have a non-negligible effect on the electromagnetic field solutions. However, computational models of ECT have not incorporated tissue conductivity anisotropy to date.

No direct and non-invasive *in vivo* measurement of brain conductivity anisotropy is available, but the similarity between the transportation processes of electrical charge carriers and

water molecules enables estimation of the effective electrical conductivity tensors from the water self-diffusion tensors which can be non-invasively acquired with diffusion tensor magnetic resonance imaging (DT-MRI) [63, 64]. Several methods have been proposed to derive the WM anisotropic conductivity from the measured diffusion tensors. In the effective medium approach [153, 154], the WM anisotropic conductivity tensors were directly calculated by a linear scaling of the diffusion tensors using an empirically determined scaling factor [153-155]. However, Rullmann et al. [147] and Gullmar et al. [93] have pointed out that using this linear scaling approach may lead to extremely large anisotropic ratios in the resulting conductivity tensors. An alternative is the volume constraint approach where the WM anisotropic conductivity tensors are computed with a fixed anisotropic ratio in each WM voxel, under the assumption that the shape of the WM diffusion tensors is prolate (cigar-shaped), rotationally symmetric ellipsoid [90, 156]. With this method, the fixed anisotropic conductivity ratio of the WM tissue can be obtained from direct measurements, e.g., 10:1 for parallel:normal orientation relative to the nerve fibers [157]. Another anisotropy modeling technique is based on the linear conductivity-to-diffusivity relationship in combination with a constraint on the magnitude of the electrical conductivity tensor [94, 95]. A "volume fraction algorithm" considering the partial volume effects of the cerebrospinal fluid (CSF) and the intravoxel fiber crossing structure has also been suggested [158], but no further studies using this approach have been reported.

In summary, existing studies of the electric field or current density resulting from ECT have investigated few electrode configurations in realistic-geometry head models, have not incorporated tissue conductivity anisotropy, and have not carried out analysis of the electric field strength in specific brain ROIs. Addressing these limitations, in the present study we develop an anatomically-accurate finite element (FE) model of the human head incorporating tissue

heterogeneity and WM anisotropic conductivity, based on individual structural MRI and DT-MRI scans. We use the head model to simulate the electric field generated in the brain by the BL, BF, RUL, and FEAST ECT electrode configurations. We quantify the differences in electric field strength among the various ECT electrode configurations in brain ROIs that have putative role in the therapeutic action and/or adverse side effects of ECT. This analysis enables us, for example, to explore whether forms of ECT associated with fewer cognitive side effects induce lower electric field strengths in hippocampus, and to evaluate the degree to which frontal electrode configurations (BF and FEAST) achieve focal frontal stimulation. We also investigate how the WM conductivity anisotropy affects the electric field distribution in the brain. This study demonstrates the utility of anatomically-realistic computational models to provide clinically salient analysis and recommendations for the optimization of ECT.

3.2. Materials and Methods

We simulated the electric field strength and distribution induced by ECT in a realistic finite element head model using the same methods described in Chapter 2.

3.2.1. ECT Finite Element Head Model Generation

An anatomically realistic human head model was created from T1-weighted magnetic resonance imaging (MRI) ($1\times1\times1$ mm^3 voxel) and diffusion tensor imaging ($1.75\times1.75\times2$ mm^3 voxel) data sets of a healthy male human subject. The generation of the human head model started with

preprocessing of the structural T1-weighted MRI images as described in Chapter 2. In this Chapter, for FE volume conductor modeling the T1-weighted MRI was first coregistered to the DT-MRI using SPM5 [76] (Wellcome Department of Cognitive Neurology, Institute of Neurology, University College London) in order to avoid the transformation of the diffusion tensors [94, 95, 150, 152]. In this process, a voxel similarity-based registration technique was applied to acquire coregistered T1-weighted MRI by maximizing mutual information that measures the degree of mutual dependence between the image intensities of corresponding voxels in both images [159]. To generate the FE meshes from the coregistered structural MRI images, the MRI images were segmented into five different sub-regions including scalp, skull, CSF, gray matter, and WM. BrainSuite2 [160] was used to extract brain tissue compartments (gray matter and WM) as well as CSF regions including the ventricles. We then segmented the skull and scalp regions using a skull extraction algorithm [161] based on a combination of thresholding and mathematical morphological operations including opening and closing.

We next modeled three conventional electrode placements (BL, BF, and RUL) [79, 80] and an investigational configuration (FEAST) [81, 82] diagrammed in Figure 2.1. Standard round electrodes (5 cm diameter) were modeled for the BL, BF, and RUL electrode configurations. For BL ECT, the two electrodes were centered bilaterally at the frontotemporal positions located 2.5 cm above the midpoint of the line connecting the external canthus and tragus [80]. For BF ECT, the electrodes were placed bilaterally 5 cm above the outer angle of the orbit on a line parallel to the sagittal plane [79]. For RUL ECT, one electrode was centered 2.5 cm to the right of vertex and the second electrode was placed in the homologous right frontotemporal position [80]. For FEAST, a wide rectangular electrode (2.5 cm × 6.3 cm) was

placed over the right motor strip and a small circular electrode (2 cm diameter) was placed over the right eyebrow.

Finally, we applied adaptive finite element meshing technique to the human head model incorporating the stimulation electrodes [88]. The resulting FE mesh of the human head and the ECT electrodes consists of approximately 1.6 million tetrahedral elements.

3.2.2. Electrical Conductivity Assignment

To evaluate the effect of WM anisotropy on the electric field, we simulated the electric field in a model with WM anisotropic conductivity as well as in a model with fully isotropic conductivity. In the isotropic head model, the electrical conductivities were assigned to 9.8×10^5 S/m for the steel electrodes, 0.33 S/m for scalp, 0.0132 S/m for skull, 1.79 S/m for CSF, 0.33 S/m for gray matter, and 0.14 S/m (nominal) for WM [73, 89, 90]. In the anisotropic model, all tissues except WM were assumed to be isotropic, since the WM has the most significant anisotropic microstructure [157, 162]. Another tissue that is often treated as anisotropic is the skull [96, 115, 135, 146, 148, 163]. However, the effective skull anisotropy originates from the macroscopic skull structure consisting of a soft (spongiform) bone layer enclosed by two hard (compact) bone layers [163, 164]. Therefore, the most accurate approach is to model the skull as three discrete isotropic layers [138, 165-167]. In the present study, however, we modeled the skull as a single isotropic layer, since the low MRI signal from bone makes accurate skull layer segmentation difficult [168], and since the mostly radial flow of current in the skull justifies the compound three-layer conductivity to be approximated by an effective radial conductivity value [165, 166].

We estimated the WM anisotropic conductivity tensors under the assumption that the conductivity tensors share eigenvectors with the measured diffusion tensors [63]. We applied the volume constraint approach to derive the WM anisotropic conductivity with a fixed anisotropy ratio in each WM voxel [90]. The detailed methodology of deriving the WM anisotropic conductivity tensors is described in Chapter 2. In the present study, we used a fixed anisotropy ratio of 10:1 (k = 10) (Nicholson, 1965), yielding σ_{long} = 0.65 S/m and σ_{trans} = 0.065 S/m.

To investigate how well isotropic models approximate the anisotropic model, we also simulated models with isotropic WM conductivity ranging from the transverse (low) conductivity estimate, σ_{iso} = 0.065 S/m, to the longitudinal (high) conductivity estimate, σ_{iso} = 0.65 S/m, including the nominal volume-constraint value of σ_{iso} = 0.14 S/m.

3.2.3. Electric Field Analysis

To determine the electric field distribution and magnitude in the brain induced by each ECT electrode configuration, the quasi-static Laplace equation was solved using the preconditioned conjugate solver in ANSYS (ANSY Inc., Canonsburg, PA, USA) (for the details see Chapter 2).

The electric field was sampled in specific brain ROIs thought to be associated with therapeutic action of ECT, including frontal pole, orbitofrontal cortex (OFC), dorsolateral prefrontal cortex (DLPFC), thalamus, hypothalamus, and subcallosal cingulate cortex (SCC) [79, 81, 169-173], or with side effects of ECT, including hippocampus and insula [36, 174-176]. We also examined the electric field in primary motor cortex (specifically, the first dorsal interosseous (FDI) motor area) and brainstem, which are thought to be relevant to seizure initiation and motor manifestations of the seizure, respectively [177, 178]. These ten anatomically defined ROIs were

manually segmented from coronal MRI sections, based on human brain atlases and definitions in the literature [179-186], and were verified with the BrainParser software [187]. We then computed descriptive statistics of the electric field strength (median, 25th and 75th percentiles, and minimum and maximum) in each of these ROIs as well as in the whole left and right hemispheres for the BL, BF, RUL, and FEAST electrode configurations.

We assessed the effect of the WM anisotropic conductivity on the induced electric field qualitatively by plotting maps of the electric field magnitude and current density vectors, and quantitatively by calculating the relative difference in electric field magnitude between the two solutions in various ROIs. The difference between the isotropic and anisotropic solutions was quantified by the statistical measure of relative error, defined as

$$\text{Relative Error} = \sqrt{\frac{\sum_{i=1}^{n}(E_i^{\text{iso}} - E_i^{\text{aniso}})^2}{\sum_{i=1}^{n}(E_i^{\text{aniso}})^2}} \tag{3.1}$$

where n is the number of samples in the respective ROI, and E^{iso} and E^{aniso} denote the electric field magnitude in the isotropic and anisotropic models, respectively [71, 73, 127, 188, 189].

3.3. Results

3.3.1. 3-D Finite Element Head Model

The human head model used for the electric field simulation is displayed in Figure 3.1. Figure 3.1(a) shows a cut-away 3-D rendering of the head model. The cropped section illustrates the five segmented tissue types—scalp (yellow), skull (blue), cerebrospinal fluid (CSF, green), gray

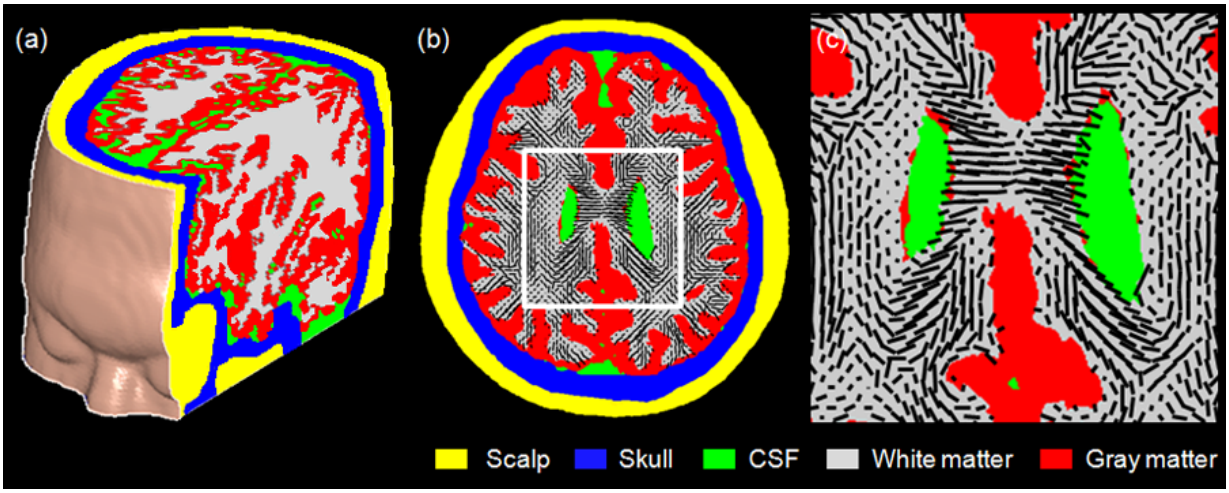

Figure 3.1. 3-D finite element head model: (a) Partial volume rendering of the human head model. The cropped section shows the five segmented tissue compartments. (b) A transaxial conductivity map with the principal orientations (the largest eigenvectors) of the WM conductivity tensors projected as black bars onto the WM regions. (c) Enlarged view of the region framed in white in (b).

matter (red), and WM (gray). Figure 3.1(b) shows a transaxial conductivity map with the principal orientation of the electrical conductivity tensors (corresponding to the orientation of the WM fibers) projected as black bars onto the WM regions. For clarity, a portion of the conductivity map framed in white in Figure 3.1(b) is magnified in Figure 3.1(c).

3.3.2. Comparison of ECT Electrode Configurations

Figure 3.2 shows a set of results for the spatial electric field magnitude distribution in the head model incorporating a fixed WM anisotropy ratio of 10:1. A qualitative comparison of the spatial electric field distributions in Figure 3.2 indicates that the different ECT electrode configurations result in distinct electric field distributions in the brain. As expected, the strongest electric field

tends to occur in the brain volume under and between the two electrodes, although the detailed distribution is complex and depends heavily on the head anatomy. The symmetric ECT electrode configurations (BL and BF) have comparable electric field strength in both hemispheres, whereas the lateralized configurations (RUL and FEAST) generate higher electric field magnitude in the right hemisphere. Similarly, configurations with anterior electrodes (BF and FEAST) induce stronger electric fields in the anterior portions of the brain than the other configurations with more posterior electrodes (BL and RUL).

Figure 3.3 shows descriptive statistics of the electric field strength (median, 25th and 75th percentiles, and minimum and maximum) in various ROIs in the left and right hemispheres of the anisotropic head model for each ECT electrode configuration. The median electric field strength in the whole brain is 3.9, 1.5, 2.3, and 2.6 V/cm, and the right-to-left hemisphere median electric field ratio is 1.0, 1.0, 2.1, and 1.9 for the BL, BF, RUL, and FEAST configurations, respectively. Besides generating the strongest electric field overall, BL ECT produces the highest median electric field in the hippocampi (4.8 V/cm), which is 1.5–2.8 times stronger than the hippocampal electric field of the other electrode configurations. In comparison to BL, RUL ECT has weaker median electric fields in all regions except in the right FDI motor area, where it is 1.4 times stronger. The ratio of the frontal (frontal pole, OFC, and DLPFC) to temporal (hippocampus) median electric field is 0.9, 3.5, 0.9, and 1.7 for the BL, BF, RUL, and FEAST configurations, respectively. Due to its frontal electrode placement, BF ECT has the highest frontal-to-temporal field ratio (3.5) among the configurations, inducing the strongest electric field in the frontal pole as well as substantial field strength in the OFC and DLPFC. Compared to the BF and RUL electrode placements, FEAST produces stronger median electric field stimulation in thalamus, hypothalamus, SCC, and insula. Moreover, compared to all of

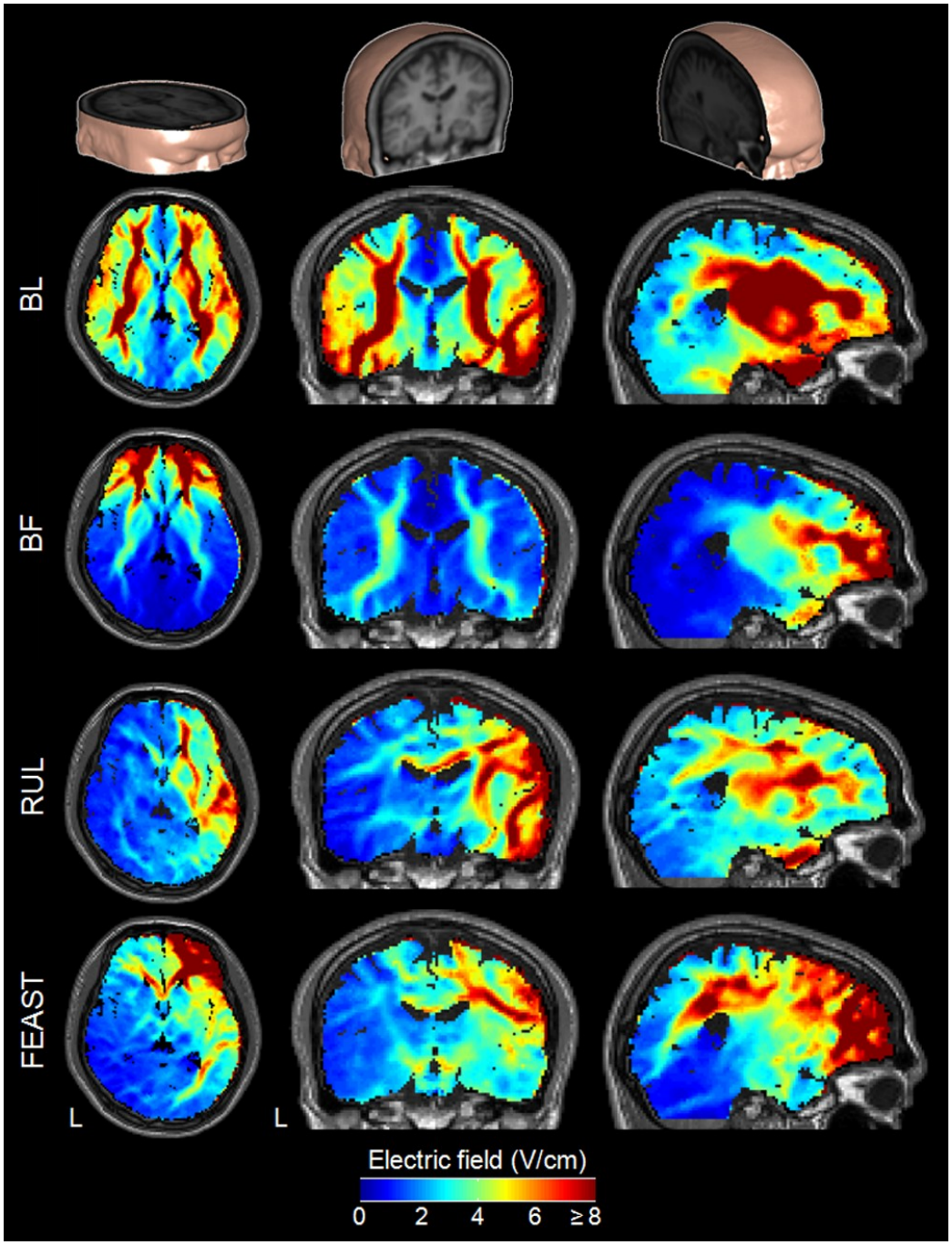

Figure 3.2. Cut-away 3-D rendering of the head model (top row) and the E-field magnitude spatial distribution in the anisotropic head model for BL, BF, RUL, and FEAST electrode configurations (second to bottom rows, respectively) with 800 mA current. Columns from left to right show axial, coronal, and sagittal views, respectively. The color map is clamped at an upper limit of 8 V/cm for good visibility of the electric field distribution. L: left.

the other configurations, FEAST induces 1.2–2.0, 1.4–2.4, and 1.6–2.2 times stronger electric fields in the right OFC, DLPFC, and SCC, respectively.

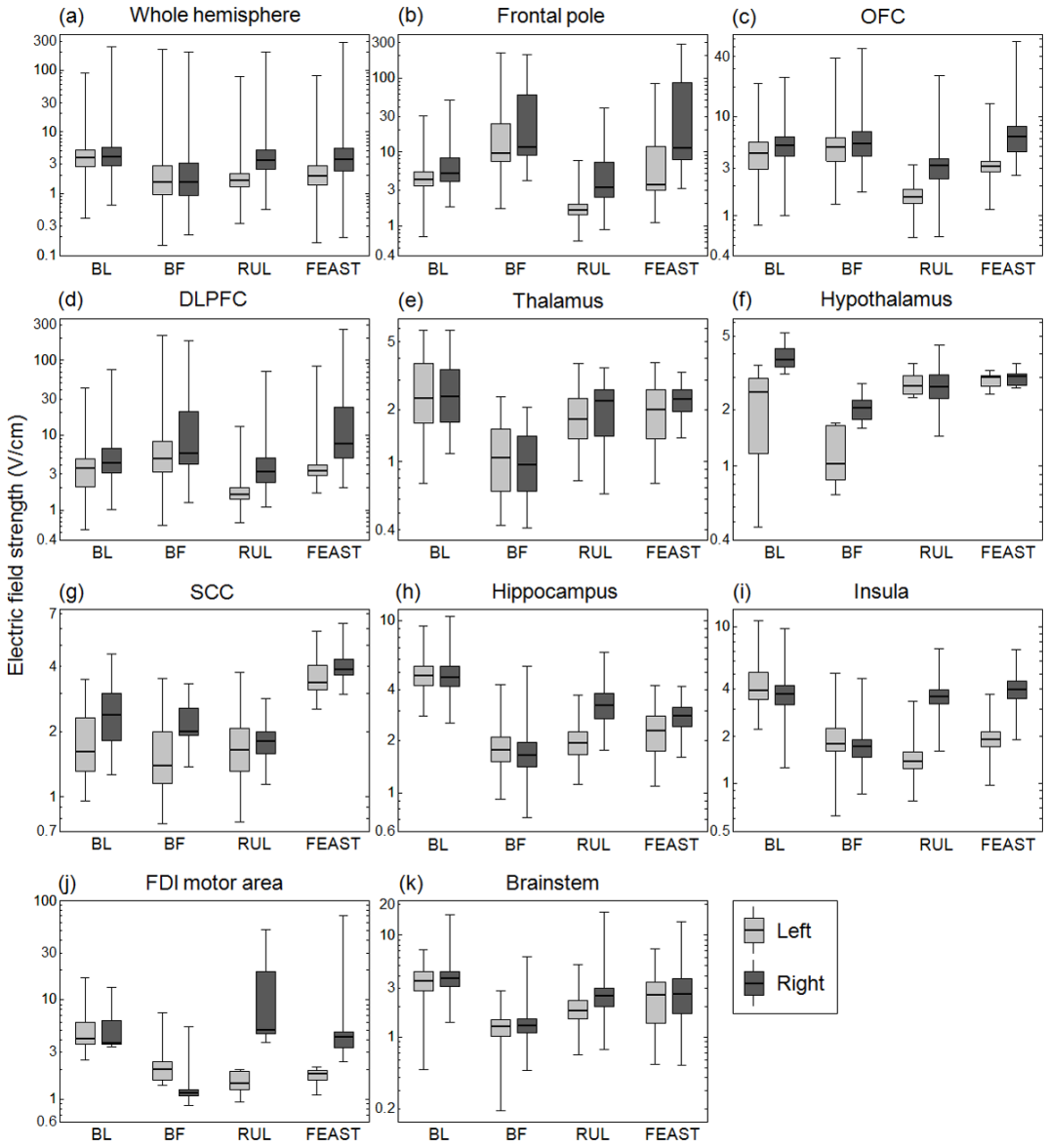

Figure 3.3. Descriptive statistics of the regional E-field magnitude generated by the four ECT electrode configurations in the left and right hemispheres of the anisotropic head model. The E-field strength (y-axis) is shown on a logarithmic scale. The boxes indicate the interquartile range (25th to 75th percentile) with the median marked by a thick horizontal black line. The whiskers delimit the minimum and maximum of the regional E-field distribution.

3.3.3. Effect of White Matter Anisotropic Conductivity

To demonstrate the effect of WM anisotropy on the electric field and current density solutions, in Figure 3.4 we plotted maps of the electric field magnitude and the current density vector field in a coronal slice (same as in Figure 3(middle row)) for BL and RUL ECT in the nominal isotropic (WM σ_{iso} = 0.14 S/m) and anisotropic head models. In this slice, the BL and RUL configurations generate, respectively, predominantly mediolateral and inferosuperior current flow. In both the isotropic and anisotropic models, the high conductivity of CSF-filled structures tends to channel current flow, as illustrated by the larger arrows in the lateral ventricles in Figures 3.4(c) and (d) and in the longitudinal fissure in Figures 3.4(e) and (f). Despite the higher current density in CSF-filled structures, the electric field magnitude there is relatively low (blue color) due to the high conductivity. Compared to the isotropic models (Figures 3.4(c) and (e)), in the anisotropic models (Figures 3.4(d) and (f)) additional channeling effects emerge as a result of the WM fiber orientation. For example, when the current flow is partially aligned with the orientation of the WM fibers, the anisotropic model enhances the current alignment with the fibers, as demonstrated by the curving of the current flow along the WM fibers in the corpus callosum and in the regions inferior to the lateral ventricles in BL ECT (Figure 3.4(d) versus Figure 3.4(c)). Furthermore, long stretches of fibers aligned with the current flow can result in denser current along the fibers, as demonstrated by the concentrated current flow along the inferosuperior-oriented internal capsule fibers in both hemispheres in RUL ECT (Figure 3.4(f) versus Figure 3.4(e)). On the other hand, current flowing in direction transverse to the WM fiber orientation generates a relatively high electric field magnitude due to the lower electrical conductivity across

the WM fibers, as exemplified by the regions well demarcated in red color in the BL electric field map (Figure 3.4(d) versus Figure 3.4(c)) corresponding to lateromedial current flow across inferosuperior and anteroposterior oriented pyramidal tract fibers.

Quantitatively, the electric field magnitude relative error over the whole brain of the nominal isotropic model (WM σ_{iso} = 0.14 S/m) compared to the anisotropic model is 18%, 7%, 7%, and 6% for BL, BF, RUL, and FEAST ECT, respectively. Figure 3.5 breaks these data down for distinct ROIs in the left and right hemispheres. The largest ROI error (39%) is observed in the left FDI motor area for RUL ECT, and the lowest error (1%) occurs in the left frontal pole for BL ECT. In prefrontal and frontal areas including frontal pole, OFC, and DLPFC in Figures 3.5(b)–(d), the maximal error of 19% occurs with RUL ECT in the left OFC. The SCC in Figure 3.5(g) exhibits relatively large differences compared to other ROIs, ranging from 14% (FEAST) to 39% (RUL). In hippocampus and insula, the largest errors are 25% and 34%, respectively.

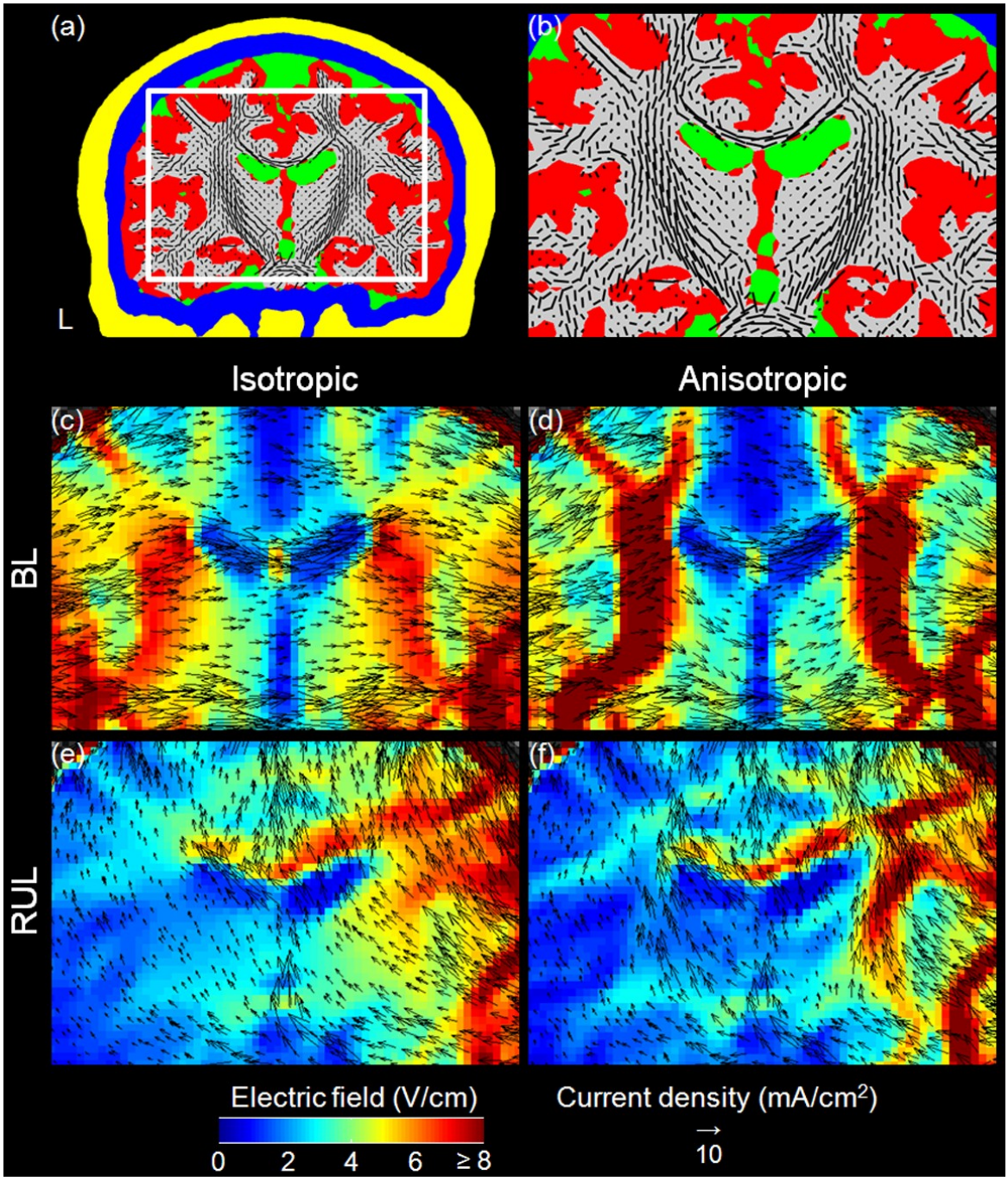

Figure 3.4. Comparison of the isotropic and anisotropic model simulations. (a) A coronal slice conductivity map using the same display conventions as in Fig. 2. (b) Enlarged view of the region framed in white in (a). (c–f) View corresponding to (b) of the E-field magnitude distribution (in color scale) and current density vector field of the isotropic (left) and anisotropic (right) head models for BL (middle row) and RUL (bottom row) electrode configurations. L: left.

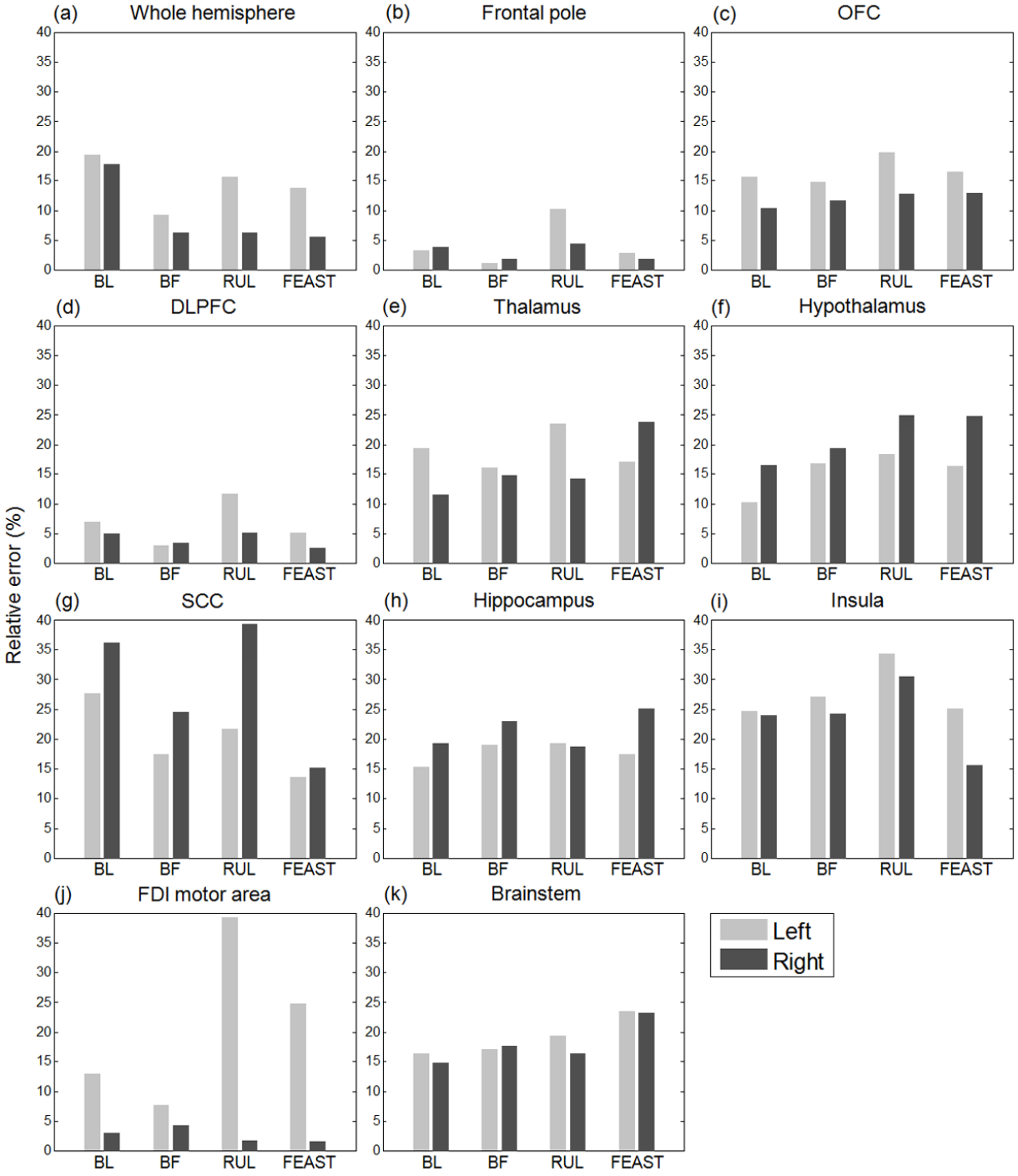

Figure 3.5. Relative error of the electric field magnitude in the isotropic versus the anisotropic head model for the various brain ROIs and ECT electrode configurations. Relative error is defined in equation (3.1).

Figure 3.6 shows the relative error in electric field magnitude over the whole brain between the isotropic and anisotropic models as a function of the WM conductivity in the isotropic model. The largest errors occur with the highest isotropic conductivity of 0.65 S/m for all configurations. The lowest errors, indicating the "best" isotropic model match to the anisotropic model, are at σ_{iso} = 0.11 S/m for BL and BF ECT and at σ_{iso} = 0.18 S/m for RUL and FEAST ECT, which are close to but distinct from the volume-constraint value of σ_{iso} = 0.14 S/m.

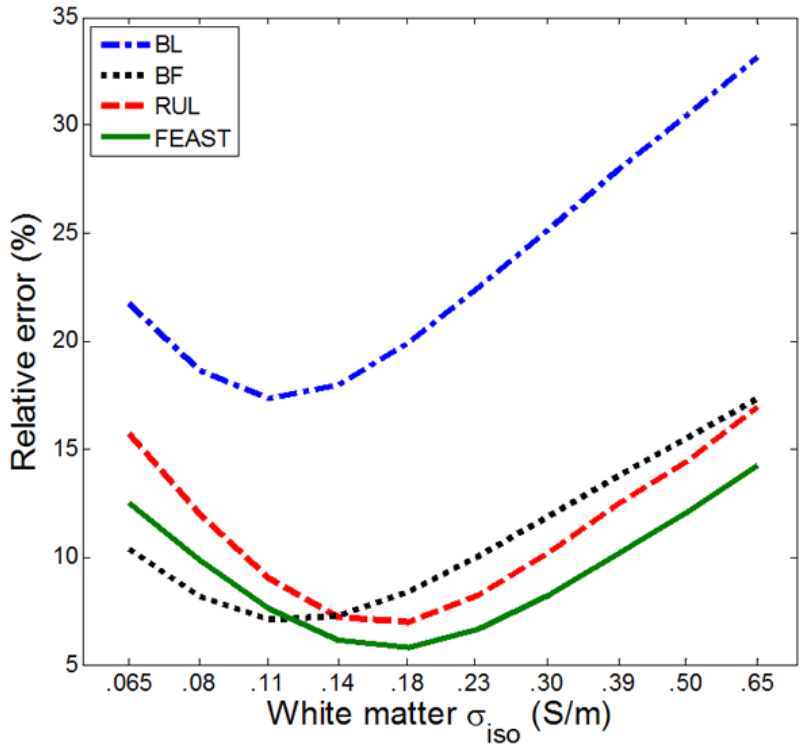

Figure 3.6. Electric field magnitude relative error in the whole brain between the anisotropic head model (WM σ_{long} = 0.65 S/m and σ_{trans} = 0.065 S/m) and the isotropic model with WM conductivity ranging from σ_{iso} = 0.065 S/m to 0.65 S/m. The four curves correspond to the four ECT electrode configurations.

3.4. Discussion and Conclusions

Even though the electric field spatial distribution is a key aspect of dosage in ECT, it has not been accurately characterized. The spatial distribution of the electric field strength is a determinant of which brain regions are directly activated by the electric stimulation delivered by various ECT electrode configurations. This work represents the first quantitative study investigating the regional differences in electric field strength resulting from variations in the ECT electrode configuration in an anatomically realistic head model.

3.4.1. Implications for ECT Technique

It has been suggested that the flow of electric current and a resultant robust seizure expression in the prefrontal cortex is requisite to the antidepressant effects of ECT, as demonstrated, for example, by the superior efficacy of BL ECT compared to low dose RUL ECT [81, 169, 190]. This view has motivated electrode configurations designed to target the prefrontal cortex, such as BF and FEAST. The results from our model confirm that BL ECT generates stronger electric field in anterior portions of the brain compared to RUL ECT. Our results further indicate that BF and FEAST generally produce higher electric field strengths in prefrontal structures compared to BL and RUL ECT (see Figures 3.2 and 3.3). In particular, compared to the other electrode configurations, BF produces the highest electric field magnitude in the frontal poles. Furthermore, FEAST produces the strongest electric field in the right OFC, DLPFC, and SCC—likely a consequence of current flow through the orbits which represent low impedance paths into the brain. Significantly, DLPFC and SCC are targets for other forms of brain stimulation

with reported antidepressant efficacy. The right DLPFC has been targeted with low-frequency (inhibitory) repetitive TMS for the treatment of depression [191]. There is evidence that focal stimulation of the SCC via deep brain stimulation reduces elevated SCC activity and normalizes aberrant network activity in depression, with resultant antidepressant effect [173, 192]. The frontal pole and OFC have strong anatomical and functional connectivity with the SCC and the rest of the dysfunctional brain network associated with depression [173, 193-195] and therefore are potential targets for stimulation as well.

Another prevailing hypothesis on the mechanism of action of ECT focuses on diencephalic stimulation. This hypothesis states that for optimal antidepressant efficacy, the seizure must be sufficiently generalized to involve diencephalon centers, particularly the thalamus and hypothalamus [79, 169]. Cortical–thalamocortical interactions are crucial for the initiation, propagation, and behavioral manifestations of generalized seizures [196, 197]. Thalamic processes that inhibit cortical function have been hypothesized to play a role in the antidepressant effect of ECT [170, 197-199]. Our results show that BL ECT produces stronger electric field in the thalamus and hypothalamus compared to BF and RUL ECT, consistent with the superior antidepressant efficacy of BL ECT as compared with low dose RUL ECT, but does not explain how adequately-dosed RUL ECT matches the efficacy of BL ECT. Notably, FEAST produces electric field strengths in the diencephalon centers that are higher than in BF and RUL, and approach those in BL. However, whether this confers high antidepressant efficacy to FEAST is unknown since FEAST clinical data has not been reported.

It has been suggested that retrograde amnesia may be related to seizure activity in the medial temporal lobe [175, 200, 201] and consequently it was proposed that techniques inducing seizures with reduced current spread to this area may cause less memory side effects [81]. The

medial temporal structure specifically associated with amnesia is the hippocampus, which has been shown to be uniquely affected by induced seizures, and to have a low seizure threshold [175]. Of all configurations in our model, BL ECT produces the strongest electric field in the hippocampi, consistent with its greater acute cognitive impairment [36, 174] and short- and long-term retrograde amnesia [175, 176] compared to BF and RUL ECT. Our results may be particularly useful for predicting the clinical effects of ECT paradigms for which clinical data is not yet available, such as FEAST. For example, the electric field strength generated by FEAST is lower than RUL in the right hippocampus, but is higher than RUL in the left hippocampus, and is higher compared to BF in both hippocampi. Therefore, one might predict that FEAST may have memory side effects lower than in BL but higher than in BF (assuming identical current levels in all configurations); this is yet to be tested clinically.

The electric field model could also inform the mechanisms behind cardiac effects of ECT. Accumulating evidence indicates that cardiovascular regulation receives significant input from cortical structures, especially the insula [202]. Direct electrical stimulation of the left caudal anterior insula leads to increased occurrence of bradycardia and depressor responses as a result of parasympathetic activation, whereas right anterior insular stimulation leads to tachycardia and diastolic blood pressure elevation as a result of sympathetic activation [203, 204]. Data from patients with insular lesions are consistent with left insular cardioinhibitory representation and right insular cardioexcitatory representation [203]. During the stimulus delivery phase of ECT, a higher likelihood of heart rate reduction and longer duration of asystole were observed with RUL compared to BL and BF ECT [205]. Since RUL ECT produces nearly three times higher electric field strength in the right insula compared to the left insula (Figure 3.3(i)), we hypothesize that the right insula is preferentially inhibited during stimulation

compared to the left insula, resulting in sympathetic withdrawal. In contrast, BL and BF ECT induce similar electric field strengths in left and right insula, thus the sympathovagal balance is less affected, consistent with the lower rates of asystole observed clinically [206, 207]. Other brain regions, such as the hypothalamus and brainstem, are also known to be involved in cardiac regulation [208]; therefore, the electric field characteristics in these regions (Figures 3.3(f) and (k)) may also contribute to cardiac effects.

Our results indicate that the electric field strengths induced by RUL are exclusively weaker than in BL ECT except in the right motor strip where the electric field magnitude induced by RUL ECT is about 38% stronger compared to BL. This observation is consistent with the lower seizure threshold of RUL compared to BL ECT, since the motor strip is thought be the likely site for seizure initiation [178]. We also found that BL and FEAST generate higher electric field strengths compared to BF and RUL in the brainstem which mediates the motor manifestations of generalized tonic-clonic seizures [177].

The above observations illustrate how the realistic ECT electric field model can contribute to a biophysical explanation of reported clinical differences among conventional electrode placements (BL, BF, and RUL), as well as to the evaluation and optimization of investigational configurations (e.g., FEAST). For example, the realistic head model can be coupled with an optimization algorithm to select scalp electrode locations and current strengths to target specific brain structures [209, 210]. Ultimately, this work may guide the development of novel stimulation paradigms with improved risk/benefit ratio.

3.4.2. Influence of Tissue Conductivity Anisotropy

The second objective of this study was to evaluate the influence of WM conductivity anisotropy on the electric field simulation. Our results, summarized in Figures 3.4 and 3.5, indicate that neglecting WM conductivity anisotropy and using instead the volume-constraint WM isotropic conductivity value of 0.14 S/m leads to relative errors in the electric field magnitude up to 18% for the whole brain and up to 39% within the considered ROIs. The maximum relative error was found in the left FDI motor area for RUL ECT. In addition, our results indicate that the electric field differences between the isotropic and anisotropic models depend upon the specific ECT electrode configuration used. For example, ignoring WM anisotropy produces errors in the FDI motor area electric field up to only 8% for the BF configuration, but up to 39% for the RUL configuration. Furthermore, the WM isotropic conductivity value that gives the best approximation of the anisotropic case, in terms of the lowest overall relative error, varies with electrode configuration, as shown in Figure 3.6. Specifically, the optimal WM isotropic conductivity value for the lateralized configurations (0.18 S/m for RUL and FEAST) is 64% higher than that for the bilaterally symmetric configurations (0.11 S/m for BL and BF). A possible explanation for this difference is that in the lateralized electrode configurations the electrical current is more aligned, on average, with the orientation of the WM fibers than in the bilaterally symmetric configurations. The results in Figure 3.6 also indicate that the volume-constraint WM isotropic conductivity (0.14 S/m) yields relative errors within 0.7% of the optima achievable with the isotropic models and is, therefore, a reasonable choice for isotropic models. Generally, the electric field magnitude errors and their sensitivity to the electrode configuration motivate the inclusion of the WM conductivity anisotropy in computational electric field models for increased accuracy.

Another important observation is that the error in the electric field strength between the isotropic and anisotropic models usually increases for brain regions that are farther away from the ECT electrodes. For example, the electric field errors in deep brain structures such as thalamus, hypothalamus, insula, and SCC (10%–39%) are higher than the errors in more superficial areas such as frontal pole and DLPFC (1%–12%) which lie closer to the scalp electrodes. Furthermore, although the overall relative error in the whole brain is higher for BL than for BF, the relative error is larger for BF than for BL in ROIs such as hypothalamus, hippocampus, insula, and brainstem that are farther away from the BF electrodes. Similarly, in the lateralized electrode configurations (RUL and FEAST), the electric field errors for highly lateralized ROIs (whole hemisphere, DLPFC, insula, and FDI motor area) are significantly larger on the left side than on the right side (where the electrodes are placed). The electric field error increase away from the electrodes could be explained in terms of the longer paths that the electrical current has to traverse from the electrodes to distant brain regions, which results in a larger cumulative error of all the differences in the conductivity tensors along the current path. Thus, incorporation of WM conductivity anisotropy in ECT electric field models is crucial for analysis of the electric field characteristics in brain regions that we try to avoid stimulating by placing the electrodes away from them. Often these are brain regions thought to be associated with adverse side effects of ECT, and thus the degree to which they are stimulated is of particular relevance to studies that evaluate ECT techniques aimed at improving safety. This observation further supports the inclusion of WM anisotropic conductivity in ECT models.

The comparison of the isotropic and anisotropic model simulations in Figure 3.4 provides insight into how the orientation of WM fibers affects the current density and electric field distributions. The current flow generally follows the path of least electrical impedance.

Consequently, compared to the isotropic model, current flow along the WM fibers in the anisotropic model is denser and follows the fiber orientation. In some cases the channeling of current along WM fiber tracts increases the local electric field strength, but in other cases this effect is offset by the lower impedance along the fibers, leading to reduced electric field strength. The current may steer away from segments of increased impedance resulting from the passage of WM fibers perpendicular to the current flow. However, when current comes across wide stretches of fibers perpendicular to its flow, the current cannot steer away and is forced to cross this high impedance barrier, resulting in high electric field magnitude. Thus, increased electric field strength in the anisotropic model compared to the isotropic model can result from either concentration of current flow along WM fibers that is not offset by the low impedance along the fibers, or from increased impedance for current flow perpendicular to WM fibers.

In support of our findings, other bioelectric head modeling studies have reported comparable effect sizes associated with the inclusion of WM conductivity anisotropy. We previously studied the impact of WM anisotropy on the current density distribution generated by tDCS and found relative errors of 53% and 19% in current density magnitude in the WM and gray matter, respectively [127]. Similarly, Sadleir et al. [91] concluded that the inclusion of the WM anisotropic conductivity in a tDCS model would result in differences up to 39% in the median current density magnitude. De Lucia et al. [150] found that WM anisotropy contributes a difference of 10% in the peak TMS-induced electric field, which is consistent with the findings of Thielscher et al. [151]. (It should be noted that the TMS electric field is substantially more superficial than the electric field in ECT and tDCS; therefore, the lower error associated with WM anisotropic conductivity in TMS is expected). Finally, Wolters et al. [90] reported that the inclusion of WM anisotropic conductivity results in up to 30% difference in the magnitude of

electroencephalographic scalp potentials generated by dipole sources within the brain. Thus, the differences between the isotropic and anisotropic model results in these studies are comparable to the relative errors up to 39% found in our study.

It has been reported that depression itself is associated with changes in the volume of specific brain structures [211, 212] and with regionally specific abnormalities of the WM fractional anisotropy [141, 142]. Patients with major depressive disorder showed a fractional anisotropy reduction up to 14% in WM, with an 8% decrease in the superior longitudinal fasciculus associated with the DLPFC [141]. Neglecting WM anisotropy in our model, which is associated with fractional anisotropy reduction of 100%, results in up to 39% difference in electric field strength. Extrapolating from these data, a pathological 14% decrease in fractional anisotropy could result in approximately 6% difference in the electric field strength. Even though this effect is relatively small, tissue conductivity anisotropy and other pathological brain structure changes should be considered as a potential source of electric field variability, as their compounded effect may be significant.

3.4.3. Model Validity and Limitations

Validation of brain stimulation electric field simulations remains a challenging problem due to the unavailability of methods for high-resolution *in vivo* electric field measurements. Nevertheless, our results in the brain (electric field strength median of 1.5–3.9 V/cm and range of 0.1–300 V/cm) are in good agreement with published modeling and experimental measurements. In the references to other studies below, the electrode current was scaled to 800 mA to allow comparison with our data. In their anatomically-realistic computational model of BL ECT,

Nadeem et al. [122] did not report statistics on the electric field distribution, but the figures suggest a brain electric field magnitude ranging from approximately 0.1 V/cm to as high as 700 V/cm. Rescaling the current from Sadleir et al.'s [91] and Parazzini et al.'s [131] anatomically-realistic tDCS models and converting current density to electric field strength, the average of their reported median values is 2.5 V/cm and 2.7 V/cm, respectively. Studies using simplified model geometries or low-resolution experimental measurement techniques generally reported lower electric field strengths [113-115, 117]. For instance, a recent simulation study by our group of BL, BF, RUL, and FEAST ECT in a spherical head model obtained median and maximum brain electric field strength ranges of 0.6–1.2 V/cm and 2.1–2.5 V/cm, respectively [117]. Rush and Driscoll's [115] measurements of a frontal-occipital electrode configuration in a half-skull immersed in an electrolytic tank yielded maximum electric field in the range of 1.5–2.5 V/cm. Intracerebral measurements in cadaver heads with stimulation current applied through bifrontotemporal electrodes produced maximum electric field strength estimates of 0.7–1.8 V/cm [113, 114]. A likely factor contributing to the lower electric field strengths reported in these studies is the effective averaging out of the spatial distribution of the electric field resulting from the simplified head models and/or from the low-resolution spatial sampling of the electric potentials in the cadaver measurements. Indeed, a study comparing head models for TMS found a ~ 51% increase of the maximum electric field strength in the anatomically-realistic model compared to simplified spherical models [151].

A limitation of the present study that may impact the electric field strength and distribution is the truncation of the head model. The T1-weighted MRI data was only acquired for the portion of the head above the level of the auditory canal. The truncated head model eliminates shunting of the ECT stimulus current in the lower portion of the head, resulting in

increased electric field magnitude in the brain. Further, the head model truncation has differential effects for various ECT electrode placements. For example, in our ECT analysis using a spherical head model (data not shown), we observed that truncation of the head model results in a 52% and 27% increase in the median electric field and a 41% and 14% increase in the peak electric field for BL and RUL ECT, respectively. Therefore, future ECT head models should be based on structural MRI and DT-MRI data set of the whole head including the skull base and a portion of the neck underneath.

Uncertainty about the thickness, structure, and conductivity of the various tissues in the model can contribute to inaccuracies of the simulated electric field and to discrepancies among various models and experimental measurements [213], but it is difficult to assess the extent of these uncertainties since, as discussed in the beginning of this section, there are no adequate empirical data to compare simulations to. For example, we observed overall comparable electric field strength in the left and right hemispheres for the symmetric ECT electrode configurations (BL and BF). However, certain regions such as hypothalamus, SCC, and FDI motor area produced asymmetric results of the median electric field magnitude (see Figure 3.3). This may be due to intrinsic anatomical asymmetry and/or errors in the tissue segmentation and the ROI boundary definition between the two sides of the head, but it is difficult to determine how much each of these factors is contributing.

There are two distinct sources of uncertainty that confound the conclusions of modeling studies: first, naturally occurring anatomical variability in the population and, second, errors in the tissue segmentation and tissue conductivity within the modeled individual(s). We have previously investigated the effect on the induced electric field in a spherical head model of varying the thickness and conductivity of various tissue layers within ranges reported in the

literature [45]. That study reported that, for example, individual male scalp and skull thickness variation, which can be as high as 58% and 34% of the average, resulted in up to 76% and 20% changes of the peak brain electric field, respectively [45]. The present study does not account for anatomical variability in the population since it is based on imaging data of a single individual; this limitation has to be considered when applying these results to interpret clinical ECT data obtained from various individuals. Nevertheless, the methods presented in this paper are general and can be applied to any individual with appropriate MRI data.

The second source of uncertainty is modeling errors of the tissue structure and electrical properties within an individual model. For example, the average thickness of the scalp, skull, and CSF underlying the skull are about 5.5 mm, 7 mm, and 3 mm, respectively [45], and the T1-weighted structural MRI data used to create our model has spatial resolution of 1 mm. Therefore, the MRI resolution contributes potential error of approximately 18%, 14%, and 33% to the thickness of the scalp, skull, and CSF, corresponding to estimated errors in the peak brain electric field up to 24%, 11%, and 14%, respectively, based on our perturbation data in the spherical male head model [45]. Further, even though a single skull layer is a reasonable choice for spherical models, the nonuniformity of the compact and spongiform layers in a real skull motivates the segmentation of these layers in a high-accuracy model [166], which may require coregistering the MRI scan with a computed tomography scan that provides substantially stronger signal from bone [168]. There is also a wide spread of tissue conductivity values reported in the literature, especially for the skull [116], and it is not known how much of this variability is attributable to individual variation and how much—to measurement error. For example, in this study we used skull conductivity value of 0.0132 S/m whereas other studies have used lower values, e.g., 0.0083 S/m [117]. Compared to a simulation of our realistic head

model with the lower skull conductivity of 0.0083 S/m (data not shown), the nominal model with skull conductivity of 0.0132 S/m increases the median electric field magnitude in the brain by 13%, 10%, 16%, and 16% for BL, BF, RUL, and FEAST ECT, respectively. These estimates of electric field variability due to potential tissue thickness and conductivity errors are commensurate with the electric field relative errors up to 18% overall and up to 39% in specific ROIs that result from neglecting WM anisotropy in the present study. Therefore, it could be argued that accounting for WM anisotropy is as important to electric field strength estimation as accurate tissue segmentation and conductivity assignment. Beyond that, anisotropic models may give more accurate electric field directionality information, as suggested by Figure 3.4, which may be particularly relevant if the electric field data were coupled with neural models which are direction sensitive [214, 215].

In our anisotropic volume conductor modeling, we adopted the volume constraint algorithm to estimate the WM anisotropic conductivity tensors with the assumption of a fixed anisotropy ratio of 10:1 in each WM voxel [90]. However, this approach may overestimate the actual ratio of the WM anisotropic conductivity tensors [94, 95]. In reality, the ratio of longitudinal to transverse WM conductivity varies. For example, the fractional anisotropy map shown in Figure 2.1 (Chapter 2) indicates that strong anisotropy is present in the pyramidal tracts and corpus callosum. On the other hand, cortical brain regions include lower degree of WM anisotropy, which is associated with lower anisotropic conductivity ratios. Recently, Bangera et al. [216] conducted an experimental validation of anisotropic head models by measuring intracranial electric potentials generated by stimulation with an implanted dipole source in the human brain [216]. Two different anisotropic models using, respectively, the effective medium approach [153, 154] and the volume constraint approach with fixed 10:1 anisotropy ratio [90]

were compared revealing that the former results in a better fit to the experimental data than the latter. In the present study, we did not examine alternative approaches for estimating the anisotropic conductivity tensors such as the effective medium approach [153, 154] and its constrained version [94, 95]. Our model allows a relatively uncomplicated incorporation of various anisotropy estimation approaches which could be investigated in future studies.

It should be also acknowledged that the present simulations address only the electric field distribution and not the direct neural activation and the resultant seizure, the topography of which is also considered to be a major contributor to clinical outcome. At present there are no computational models that can realistically simulate the induction and propagation of seizures throughout the whole brain. Because we cannot realistically simulate the neural response to ECT, we did not explore the effect of various parameters of the ECT stimulus current such as the current amplitude, pulse width, and frequency. Nevertheless, since the electric field strength is directly proportional to the stimulus current amplitude, our data can be straightforwardly scaled to other current intensities. Furthermore, systematic data on the clinical effects of various current amplitudes is presently lacking as ECT is done exclusively with fixed current amplitudes of 800 mA or 900 mA [111]. We have previously used the assumption of a single neural activation threshold throughout the brain to explore the effect of the stimulus current amplitude on the focality of direct neural activation in a spherical head model, and have suggested that reduction and individualization of the current may be productive strategies for better targeting of ECT [111, 117, 217]. However, more empirical data linking the electric field characteristics to seizure induction have to be accumulated to support the incorporation of neural dynamics in the realistic head model, which would, in turn, enable explanation of the effect of the stimulus current parameters.

Chapter 4

Electric Field Characteristics of ECT and MST

4.1. Introduction

Electroconvulsive therapy (ECT) has unparalleled antidepressant efficacy in the treatment of severe major depression [79]. ECT induces a generalized seizure under anesthesia for therapeutic purposes using electric current delivered through electrodes placed on the scalp. However, cognitive side effects of ECT such as retrograde amnesia limit its clinical use [20]. Variations in ECT technique have been introduced in an attempt to improve the risk to benefit ratio of ECT by manipulating stimulation parameters including electrode placement and stimulus current parameters [218]. For instance, high dose right unilateral (RUL) ECT has a comparable efficacy to bilateral (BL) ECT with a significant decrease in amnesia [38]. Alternative approaches have included bifrontal (BF) ECT [219] and two experimental electrode configurations, focal electrically administered seizure therapy (FEAST) [220] and frontomedial (FM) ECT [221], to target prefrontal cortex while sparing certain brain regions (e.g., hippocampus) thought to be associated with adverse side effects of ECT [20]. Another alternative is magnetic seizure therapy

(MST) which is a means to achieve more focal seizure induction using repetitive transcrnaial magnetic stimulation (rTMS) [1, 222].

Previously, using a spherical head model, we compared the suprathreshold direct stimulation strength and volume (focality) of ECT and MST configurations [86], showing that the electric field strength relative to threshold for MST is 3–6 times weaker and 10–60 times more focal compared with conventional ECT with 800 mA, 0.3 ms pulses. Spherical head models, however, are limited by the substantial simplification of the head anatomy and anisotropic tissue properties. In Chapter 3, in a realistic head model we quantified the induced electric field strength in various brain regions of interest (ROIs) by the BL, RUL, BF, and FEAST ECT electrode configurations [55]. However, that study used a truncated human head model and the electric field characteristics of FM ECT and MST have not been investigated directly.

In this Chapter, we investigate the characteristics of the electric field induced in the brain by ECT and MST. We create an anatomically realistic finite element model of the whole head to simulate the electric field distribution induced by various ECT electrode and MST coil configurations. We determine the stimulation strength and focality relative to an estimated neural activation threshold to compare the electric field characteristics generated by ECT to those by MST. The comparison of the electric field stimulation strength and focality of various ECT and MST modalities could help the interpretation of clinical ECT and MST studies and may guide the improvement of ECT and MST dosing paradigms for reduced side effects.

4.2. Materials and Methods

We simulated the electric field induced by ECT and MST in a realistic human head model. The modeling methods are described in detail in Chapter 2 and summarized here.

4.2.1. ECT and MST Head Model Generation

One healthy human subject (male, age=34 years) participated in this study. T1-weighted magnetic resonance imaging (MRI) and diffusion-tensor imaging (DTI) of this subject, including the skull base and a portion of the neck underneath, were acquired on a 3 T Philips Achieva scanner (Philips Medical Systems, Best, Netherlands) using an 8-channel head coil. The electric field induced by five ECT electrode configurations including bifrontotemporal (BL), bifrontal (BF), right unilateral (RUL), and investigational anterior–posterior focal electrically administered seizure therapy (FEAST) and frontomedial (FM) electrode configurations as well as an MST coil configuration (circular) was computed in an anatomically realistic finite element model of the human head. All tissue regions were considered electrically isotropic except the white matter. We used electrical conductivity values given in Table 2.1 for the isotropic tissue compartments. We deployed the volume normalized technique to derive the white matter conductivity tensors (for details see Chapter 2).

4.2.2. Electric Field Simulation

The methods to simulate the electric field strength induced by ECT and MST are described in detail in Chapter 2 and are summarized here. Since the current waveform frequencies in ECT and

MST are relatively low (<10 kHz), the electric field solutions were obtained by deploying the quasi-static approximation using the finite element analysis software ANSYS (ANSYS Inc., Canonsburg, PA, USA). The spatial distribution of the electric field induced by each of the five ECT electrode configurations was computed at a current of 800 mA using the preconditioned conjugate gradient solver. A time-harmonic simulation with appropriate boundary conditions was performed to compute the spatial electric field distribution generated by CIRC MST at maximum output of the Magstim Theta device [86, 223].

4.2.3. Stimulation Strength and Focality Analysis

In addition to the electric field magnitude, other factors affecting neural response include pulse shape, pulse width, and direction, as well as the neuronal morphology and membrane properties, and the state of the neuron and the neural network connected to it, which could be affected by anesthesia. We calibrated the electric field simulation to an empirically-derived neural activation threshold, E_{th}, by normalizing the electric field spatial distribution to that threshold, $E(\mathbf{r})/E_{th}$. Neurons in brain areas where $E(\mathbf{r})/E_{th} > 1$ are likely to be robustly depolarized and generate action potentials, whereas regions where $E(\mathbf{r})/E_{th} < 1$ are unlikely to produce a strong response. Such calibration of the electric field simulation to an empirically determined neural response threshold can largely take into account the various factors affecting the neural response listed above, and can partially compensate for inaccuracies in the tissue property modeling, since the neurons respond to the real electric field in the brain. For example, if frequency dispersion effects in the conductivity and permittivity result in distortion of the electric field pulse

compared to the stimulus pulse shape [85, 102] and/or if the assumed tissue conductivity is inaccurate, these effects will be factored in E_{th}.

We simulated the electric field strength for current amplitude of 800 mA for BL, RUL, and BF ECT (conventional in clinical practice); 612 mA for FEAST (average current amplitude in [220]); and 500 mA for FM ECT (as used in [221]). MST was simulated for maximum current amplitude of a Magstim Theta device (as used in clinical studies) [1, 86].

We calculated the stimulation strength relative to a neural activation threshold by dividing the electric field magnitude in the brain by the electric field threshold, E/E_{th} [61, 62, 86]. We used estimates of the electric field thresholds for ECT and MST derived in our previous study: 0.25 V/cm for ultrabrief ECT (rectangular pulse width=0.3 ms) and 0.64 V/cm for CIRC MST (cosine pulse duration=0.4 ms), respectively [86]. We quantified the focality of stimulation by calculating the brain volume exposed to electric field magnitude stronger than the neural activation threshold, i.e., the volume where $E/E_{th} \geq 1$ [61, 62, 86].

4.3. Results

4.3.1. Individual Realistic Head Model

An individual human head model used for the ECT and MST electric field simulation is displayed in Figure 4.1. The segmented tissue regions corresponding to skin, skull compact, muscle, sclera, vertebrae, gray matter, lens, eyeball, optic nerve, white matter, and spinal cord are labeled in Figure 4.1.

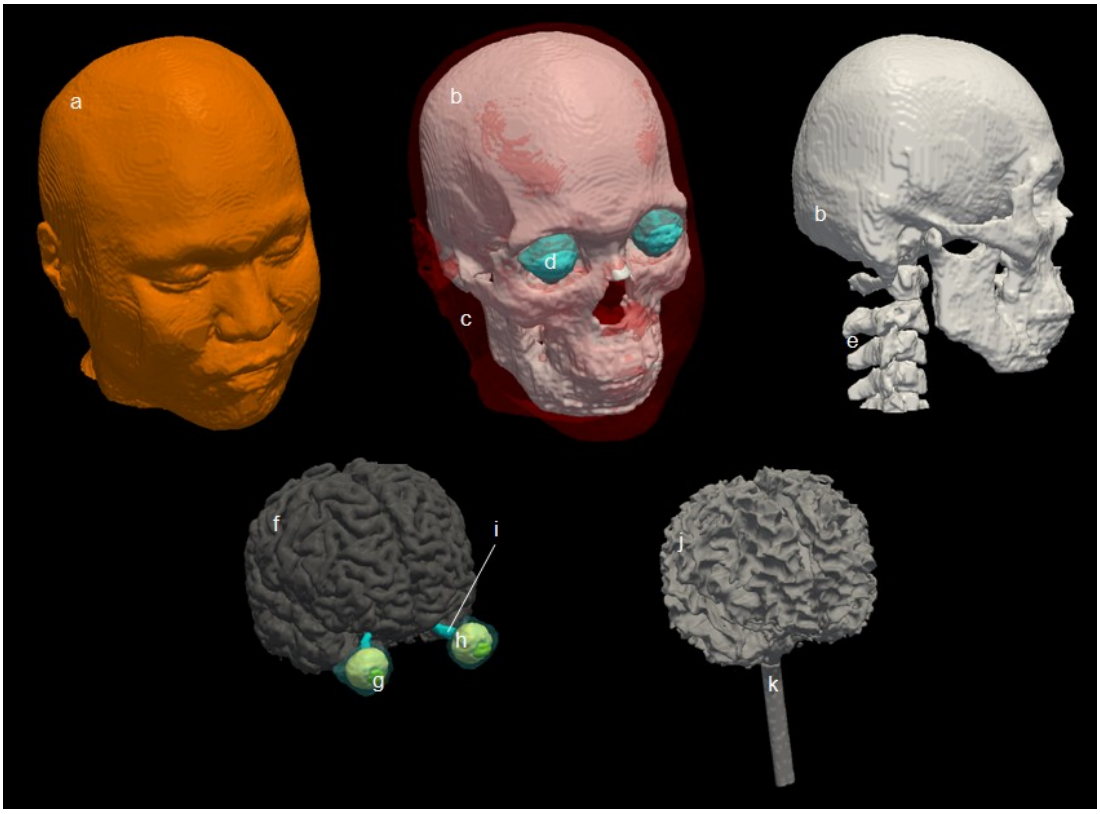

Figure 4.1. An individual realistic head model of the human subject. The various conductivity compartments are labeled including (a) skin, (b) skull compacta, (c), muscle, (d) sclera, (e) vertebrae, (f) gray matter, (g) lens, (h) eyeball, (i) optic nerve, (j) white matter, and (k) spinal cord.

4.3.2. Electric Field Distribution Relative to Neural Activation Threshold

Figure 4.2 shows the simulated BL, BF, RUL, FEAST, and FM ECT electrode configurations as well as the CIRC MST coil configuration, and corresponding cortical surface maps as well as coronal cross-sectional maps of the electric field distributions relative to the neural activation threshold E_{th} at current of 800 mA for the BL, BF, and RUL ECT, 612 mA for FEAST, 500 mA for FM ECT, and at 100% stimulator output for the CIRC MST.

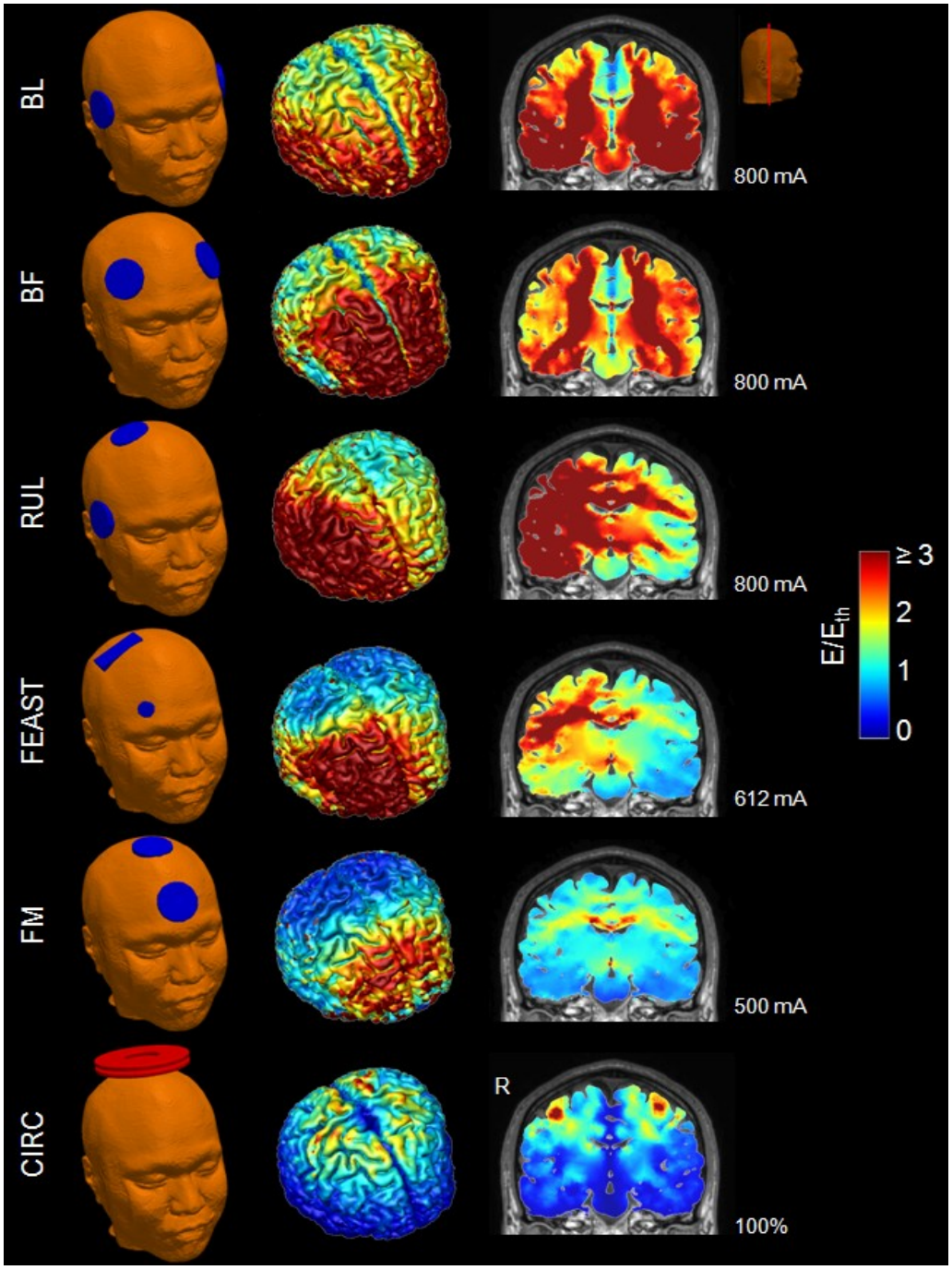

Figure 4.2. Simulation models of BL, BF, RUL, FEAST, and FM ECT as well as CIRC MST (left column). Electric field stimulation strength relative to neural activation threshold (E_{th}) at current of 800 mA for BL, BF, and RUL ECT, 612 mA for FEAST, 500 mA for FM ECT, and 100% Magstim Theta output for CIRC MST coil configuration on the cortical surface (middle column) and in a representative coronal slice (right column). E_{th} is 0.25 V/cm for ECT and 0.64 V/cm for MST. R: right.

4.3.3. Stimulation Strength and Focality

Figure 4.3(a) shows descriptive statistics on the electric field magnitude relative to the neural activation threshold in the whole brain at current of 800 mA current for the BL, BF, and RUL ECT, 612 mA for FEAST, 500 mA for FM ECT, and 100% stimulator output for the CIRC MST coil configuration. The results indicate that the stimulation strength of ECT relative to the neural activation threshold is substantially higher than that of MST. The median ECT induced electric field strength ranges from 0.8 to 3.4 times threshold, corresponding to FM and BL ECT, respectively, whereas for CIRC MST it is only 0.3 times threshold (0.07 V/cm). Furthermore, the maximum electric field strength relative to threshold induced by ECT is 1.2–7.3 times higher than that by MST. The percentage of brain volume stimulated above electric field threshold for neural activation is shown in Figure 4.3(b). Among the ECT paradigms, BL at 800 mA stimulates the largest brain volume (99.8%), while FM at 500 mA produces the most focal brain stimulation (47 %). CIRC MST produces more focal stimulation (21%) than all of the ECT modalities. Thus, the stimulation by MST is 3–11 times weaker (in median value) and 2–5 times more focal than the ECT paradigms.

Figure 4.4(a) shows the 3-D masks of subcortical structures including thalamus, hippocampus, and insula. Figures 4.4(b) and (c) show the left and right hippocampal regions onto a transaxial MRI slice and corresponding 3-D surface renderings of left and right hippocampal regions, respectively.

Figure 4.5 shows descriptive statistics on the electric field magnitude relative to the neural activation threshold in the left and right hippocampal regions for the various ECT and MST modalities. As observed in Figure 4.3(a), the stimulation strength of ECT relative to the neural activation threshold in hippocampus is also substantially higher than that of MST. The

median ECT induced electric field strength in hippocampus ranges from 0.9 to 3.8 times threshold, corresponding to FM and BL ECT, respectively, while for CIRC MST it is only 0.2 times threshold (0.12 V/cm). Thus, the stimulation strength in hippocampus by MST is 5–20 times weaker (in median value) than the ECT paradigms.

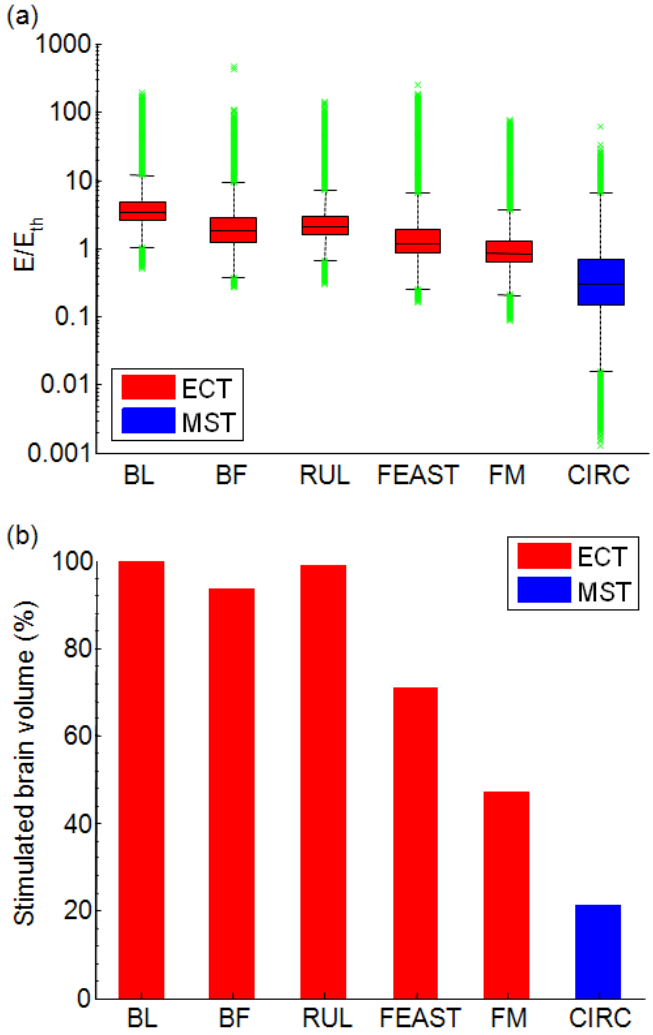

Figure 4.3. (a) Descriptive statistics of E-field magnitude relative to neural activation threshold at current of 800 mA for BL, BF, and RUL ECT, 612 mA for FEAST, 500 mA for FM ECT, and 100% stimulator output for CIRC MST coil configuration. Boxes indicate the interquartile range (25th to 75th percentile) with the median marked by a horizontal black line. Whiskers delimit approximately the 99.3 percentile of the E-field distribution. Outliers beyond this range are plotted in green. (b) Percentage brain volume stimulated above neural activation threshold ($E \geq E_{th}$).

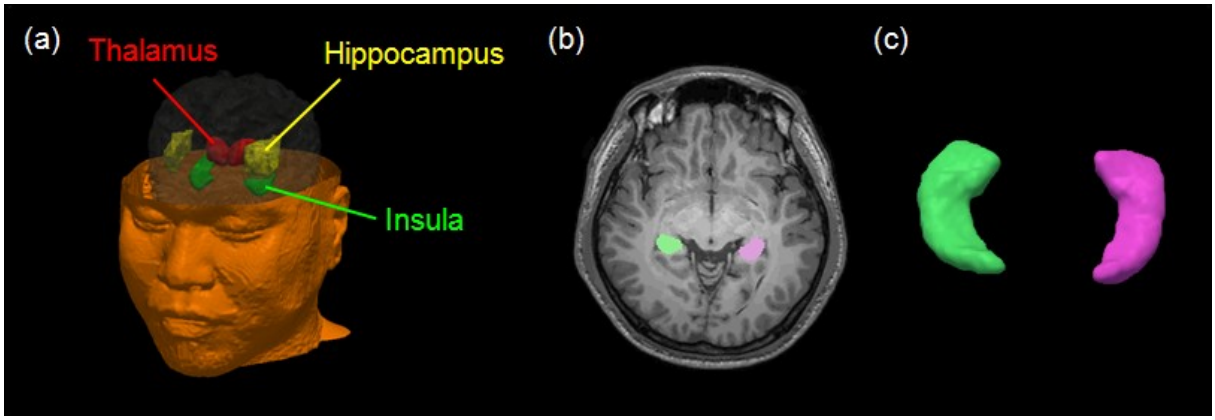

Figure 4.4. (a) 3-D segmentation masks of subcortical structures representing thalamus, hippocampus, and insula. (b) Hippocampal regions onto a transaxial MRI slice and (c) corresponding surface renderings of hippocampus.

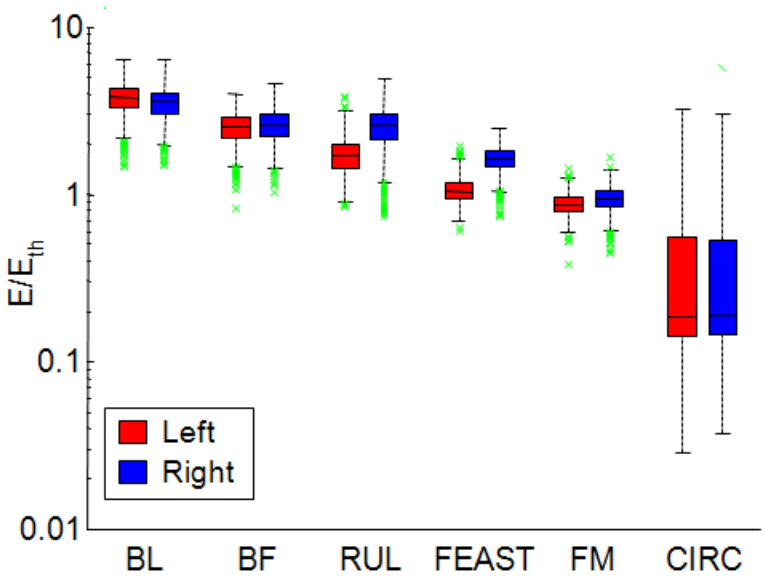

Figure 4.5. Descriptive statistics of electric field magnitude relative to neural activation threshold in hippocampus at current of 800 mA for BL, BF, and RUL ECT, 612 mA for FEAST, 500 mA for FM ECT, and 100% stimulator output for CIRC MST coil configuration. Boxes indicate the interquartile range (25th to 75th percentile) with the median marked by a horizontal black line. Whiskers delimit approximately the 99.3 percentile of the E-field distribution. Outliers beyond this range are plotted in green.

4.4. Discussion and Conclusions

We examined the electric field stimulation strength and focality of various ECT electrode and MST coil configurations using a high-resolution, anatomically accurate, finite element model of a whole human head. The results in Figure 4.2 demonstrate the different patterns of stimulation in the brain for the various ECT electrode and MST coil configurations. The substantially different electric field exposure of the brain suggests that seizure initiation and modulation by the stimulus train may have different spatial profiles across the various modalities.

Consistent with our previous findings [10], this study indicate that at the high current amplitude (800 mA) used in clinical ECT practice, the electric field in the brain exceeds the threshold for neural activation by more than 2-fold and stimulates more than 94% of the brain volume, much higher than necessary for seizure induction and possibly contributing to adverse side effects of ECT. While experimental modalities like FEAST and FM ECT produce more focal and closer to threshold stimulation by virtue of the electrode configuration and lower current amplitude, these modalities still stimulate directly more than 47% of the brain. On the other hand, CIRC MST induces the weakest, most superficial electric field, stimulating only 21% of the brain volume. Thus, MST produces very focal stimulation, that is nevertheless capable of inducing generalized seizures [8].

At conventional current amplitude of 800 mA, all standard ECT electrode configurations result in direct stimulation of hippocampus. BL and RUL ECT electrode configurations generate the strongest and weakest hippocampal electric field, respectively. The results demonstrate that direct hippocampal stimulation can be avoided by reducing stimulus current 2–4 fold. Of the evaluated ECT electrode configurations, the novel FM configuration with lower current amplitude (500 mA) results in the weakest direct stimulation of hippocampus. On the other hand,

CIRC MST produces the weakest hippocampal stimulation compared to the various ECT modalities.

Taken together, these observations support exploring ECT paradigms with current amplitude lower than the minimum of conventional ECT devices (500 mA) as a means of reducing side effects. Reduced stimulus current may decrease side effects, but may also compromise therapeutic efficacy. Our study further demonstrates the utility of computational electric field models to examine and compare various stimulus delivery paradigms for electric and magnetic seizure therapy, including novel electrode/coil and current amplitude configurations (e.g., FEAST and FM ECT, and CIRC MST).

Chapter 5

Effect of Anatomical Variation on Individual Transcranial Electric Stimulation Threshold

5.1. Introduction

Electroconvulsive therapy (ECT) is a therapeutic intervention that induces a generalized seizure in anesthetized patients by administering electric current to the brain via scalp electrodes. ECT is a highly effective treatment for medication-resistant psychiatric disorders such as major depression, however its use is limited by cognitive side effects [25]. The tolerability of ECT can be improved by using right unilateral (RUL) versus bifrontotemporal electrode configuration [112] as well as briefer current pulses [28, 224], both of which make the electric field induced in the brain more focal [111]. The current amplitude is another parameter that controls the electric field focality and therefore could potentially be used to make the stimulation more focal and to compensate for individual anatomical variability in order to reduce side effects [217].

Motor threshold (MT) is the threshold pulse amplitude required to elicit a muscle twitch. It is commonly used in transcranial magnetic stimulation (TMS) to individualize the amplitude of stimulus trains in repetitive TMS paradigms and to select frequency and train duration to reduce the risk of inadvertent seizure [225], since it captures the effect of anatomical variability on the electric field induced in the brain as well as individual variation in neural excitability. Similarly, the MT can be determined with transcranial electric stimulation (TES) delivered through the electrodes used for ECT [226]. TES in an awake subject can be uncomfortable, but ECT-titrated MT could readily be determined in subjects under anesthesia immediately prior to seizure induction [226].

If the MT data is coupled with a model of the electric field induced in the brain, the threshold electric field strength for neural activation can be estimated [227]. The electric field strength induced by TES in the brain can be simulated by computational models, ranging from concentric spheres [116, 117] to realistic head representation [68, 228] using the finite element method (FEM). Since the electric field distribution is strongly affected by individually variable head geometries, a realistic, individual head model provides more accurate predictions of the electric field induced in the brain compared to the simplified spherical models. The stimulus current corresponding to individual MT can be injected into the model, resulting in electric field strength in the motor cortex controlling the target muscle that corresponds to the neural activation threshold. Previously we introduced an electric field simulation model incorporating a waveform-specific neural activation threshold [86], however that study is limited by the five-layer concentric spherical model and neural activation threshold estimated from studies done under different conditions than ECT procedures.

Due to the physiological and behavioral similarities between human and nonhuman primate (NHP), the NHP models are invaluable for understanding the mechanisms of therapeutic interventions [82, 229]. The NHP models can then be used to empirically estimate the neural activation threshold and to address clinically salient question about the rational dosing for seizure therapy [82]. Such NHP models have been widely used to optimize stimulation parameters for efficient seizure induction [226], characterize cognitive side effects of ECT [229], and study underlying mechanisms of action of ECT [230]. The growing use of the NHP models has generated strong interest in developing a realistic NHP head model based on structural magnetic resonance imaging (MRI) data. In generating an anatomically-accurate NHP model, one critical requirement is tissue segmentation of the head to represent complicated geometries and material properties of the head tissues. However, several challenges exist for the segmentation of the NHP head. There are a plethora of available segmentation tools to extract different tissue compartments from the human MRI images, but the existing software packages have been developed and fine-tuned for the human brain MRI data. As such, such tools still need to be adapted and optimized for the NHP brains. Furthermore, since the NHPs have relatively smaller brain sizes and somewhat different brain anatomy than humans, the segmentation tools developed for human brain MRI are not well adapted for processing the NHP MR images.

The spatial distribution of the electric field resulting from subject-specific NHP computational models for TES has not been accurately characterized. An accurate estimate of the electric field distribution based on an individual realistic-geometry head is needed, since *in vivo* electric field measurements with high spatial resolution are currently not feasible. At present, the electric field or current density fields are best estimated using computational forward models [68, 111, 116, 117, 227, 231-235]. Although there is a dearth of direct validation of these models,

attempts have been recently made to validate the accuracy of the FEM forward models of the human by comparing to neurophysiological measurements [232, 233]. For instance, the simulated electric field strength by TMS was compared to the MEP amplitudes in response to single pulse TMS, revealing that the electric field magnitudes resulting from subject-specific models correlated with physiologically observed MEP amplitudes [233]. Scalp surface potentials generated by the FEM simulation of TES were correlated with induced scalp voltages by low-intensity TES [232]. In fact, a substantial number of electric field/current density modeling studies with the human FEM models have been published in the context of various TES and TMS paradigms [58, 68, 91, 96, 117, 124, 131, 137, 150, 151, 228, 232-234, 236-240]. However, there remains a dearth of modeling effort using the animal models such as NHP [82] or mouse [241], although the utility of these animal models of transcranial stimulation is increasing to help to understand the biophysical mechanisms of transcranial stimulation techniques [82, 226, 241].

In the present study, we develop realistic volume conductor modeling of the four NHP heads incorporating tissue heterogeneity and tissue conductivity anisotropy using the finite element method (FEM). We utilize individual-specific NHP models to compute the spatial distribution of the electric field strength generated by a right unilateral (RUL) ECT electrode configuration. We investigate the effect of anatomical differences on the electric field strength in the brain across four subjects at a fixed stimulus current amplitude. We also aim to derive an empirical estimate of the neural activation threshold by coupling the simulated electric field strength with individually-titrated RUL TES MT and to evaluate how well a simple TES MT titration procedure could be used for individualizing the current amplitude by accounting for individual anatomical variability in a NHP model of ECT. Finally, we test whether individual differences in TES MT can be predicted by individual anatomical variability as captured by

structural MRI data and subject-specific electric field simulation models. Our findings could be further used with realistic human models [68] and in clinical studies to explore novel ECT dosing paradigms, and as a novel noninvasive means to determine individual dosage requirement for ECT. Preliminary results from this study were previously presented in part in conference proceedings [242].

5.2. Materials and Methods

We simulated the electric field induced by RUL TES in realistic finite element NHP head models using the same methods described in Chapter 2. The modeling methods are described in detail in Chapter 2 and are summarized here.

5.2.1. TES Finite Element Model Generation

The generation of a NHP head model started with preprocessing of the structural T1-weighted MRI images. As a first step, we extracted the monkey head regions from background noise and artifacts using a morphological processing technique including thresholding, opening, and closing of the head binary masks [6]. The head MRI images were upsampled ($0.5\times0.5\times0.5$ mm^3 voxel) and were spatially oriented along manually-defined anatomical landmarks, corresponding to anterior commissure, posterior commissure, and fiducials for inter-hemispheral midline. The MRI image intensities were corrected for bias field inhomogeneity [11]. We then applied content-preserving anisotropic diffusion filtering to remove the image noise while preserving

content details and enhancing tissue boundaries [9]. Finally, non-brain regions were removed using the skull-stripping algorithm in FSL [10]. As a second step, we implemented an automatic algorithm that adopts the "unified segmentation" approach in SPM8 [12]. The de-skulled MRI images were automatically segmented into tissue probability images corresponding to gray matter, white matter, and cerebrospinal fluid (CSF) based on the macaque tissue priors [13]. The non-brain regions were manually segmented into 11 different tissue compartments, including skin, muscle, skull spongiosa, skull compacta, vertebrae, spinal cord, lens, eyeball, sclera, optic nerve, and sinus, using an in-house segmentation algorithm and the ITK-SNAP software [14]. As a third step, we modeled the RUL electrode placement which is standard in clinical ECT. The electrodes are round with a diameter of 2.5 cm diameter (half of the diameter of human electrodes due to the smaller size of the NHP head). One electrode was centered 1.25 cm to the right of vertex and the second electrode was placed in the homologous right frontotemporal position (see Figure 5.1). The contact surface between each electrode and the skin was defined by the outer surface of the NHP head. As a last step, we applied adaptive finite element meshing technique to the individual NHP head models incorporating the stimulation electrodes. The individual-specific TES finite element models of the four heads were created by means of the restricted Delaunay tessellation algorithm [15], each consisting of approximately 1.8 million tetrahedral elements.

5.2.2. Electric Field Computation

We created volume conductor head models by assigning anisotropic electrical conductivities to the white matter compartment, and isotropic conductivities to all other tissue regions. The

isotropic electrical conductivity values are listed in Table 2.1 [6]. The conductivity tensors in the white matter were computed using the volume normalized approach [16, 17], where the eigenvalues of the conductivity tensor match the eigenvalues of the diffusion tensor, and the conductivity tensor is scaled so that its volume equals that of an isotropic conductivity tensor with conductivity given in Table 2.1 (volume constraint).

Each of the realistic TES finite element models along with the electrical conductivity values was imported into the finite element analysis software ANSYS (ANSYS Inc., Canonsburg, PA, USA). Due to the low frequency content (< 10 kHz) of the stimulus current of conventional TES and ECT devices, the quasi-static approximation can be deployed to simplify the electric field simulation by neglecting wave propagation, capacitive, and inductive effects [105, 243]. Thus, the electric field solutions were obtained by solving the Laplace equation with no internal sources [68]. The linear equation system of the finite element method was solved using the preconditioned conjugate gradient solver (relative tolerance=1×10^{-8}) within ANSYS. The electric field distribution was determined by taking the gradient of the scalar potential V.

5.2.3. *In Vivo* Motor Threshold Titration

We determined the MT corresponding to the amplitude of a single TES pulse required to elicit a motor response in sedated NHPs [226]. The NHP subjects were sedated with ketamine (5–10 mg/kg i.m.) and xylazine (0.35–0.7 mg/kg i.m.) [44]. The electrode sites were prepared by cleaning with alcohol to remove scalp oils and then rubbing with an abrasive gel (NuPrep, Weaver & Co., Aurora, CO) to reduce impedance. Thymapad adhesive electrodes (Somatics, LLC, Lake Bluff, IL) were cut down to 2.5 cm circles. The MT was titrated by stepping the

amplitude of single stimulus pulses (pulse width = 0.2 ms) delivered through the RUL ECT electrodes with a DS7AH high-voltage constant-current stimulator (Digitimer, Welwyn Garden City, Hertfordshire, UK). Electromyography (EMG) was measured with needle electrodes from the first dorsal interosseous (FDI) muscle in the left hand, since the RUL electrode configuration predominantly stimulates the right hemisphere [68]. We determined the MT as the lowest stimulus pulse amplitude needed to achieve a 50 μV peak-to-peak motor evoked potential (MEP) for at least five out of ten trials [244]. In each subject, the MT was titrated three times on three separate days. Each titration session included determination of two MTs corresponding to the two current polarities applied to the electrodes, which were then averaged to produce a single MT value per session. This average bidirectional MT is relevant to ECT since the ECT stimulus consists of current pulses with alternating polarity [111].

5.2.4. Neural Activation Threshold Estimation

Individual neural activation threshold was estimated from the median electric field strength in the FDI representation of motor cortex at the stimulus pulse amplitude corresponding to the individual MT. To sample the simulated electric field in the FDI regions, we created an anatomical template map that includes the FDI areas, which were manually delineated on the published macaque brain "F99" atlas [245] based on the rhesus macaque brain stereotaxic atlases [246, 247] and the web-based Scalable Brain Atlas (http://scalablebrainatlas.incf.org). The primary motor cortical representation area of the hand at the precentral gyrus "hand knob" was determined from coronal MRI slices and verified in the axial plane [248, 249]. For segmentation of multiple NHP subjects, we developed an automatic algorithm for atlas-based region of interest

(ROI) segmentation using subroutines of SPM8 (http://www.fil.ion.ucl.ac.uk/spm). Each individual brain volume was warped to the atlas template in the least squares sense, thus minimizing the sum of squares difference between the subject and template image. This process computed a spatial transformation matrix that best registers the individual brain volume to the template [76]. Subsequently, the brain volume was aligned to the template map enclosing the FDI labels, and each voxel was labeled with the FDI structure label using the transformation matrix. Finally, the individual FDI volume labels were created by transforming back into the native space through the inverse of the deformation field.

5.2.5. Anatomical Predictors of Motor Threshold

To identify anatomical predictors of the individual MT, we examined relations between the individual average MT and electrode-to-cortex distance under the electrode centers, skin-to-cortex distance at vertex, brain volume, and the ratio of the electrode current to the median FDI electric field strength. The Pearson's linear correlation coefficient was computed for correlation analysis.

5.2.5.1. Tissue Thickness

Since the tissue thickness between the electrode and cortex is a critical determinant of the amount of stimulus current reaching the cortex [116, 250], we examined the relations between the measured MT and the electrode-to-cortex distance under the electrode centers as well as the skin-to-cortex distance at vertex. Calculation of these distances was performed in three

dimensions using the outer skin and cortical surface meshes. The distance from slice views in two dimensions would result in overestimation of the skin-to-cortex distance, since a closer distance could be found out-of-plane [251]. Therefore, for each node on the tessellated skin surface, we searched for the intersection along the direction of the surface normal at that node and the cortical surface. The skin-to-cortex thickness was then determined as the shortest distance between the two surfaces [252].

5.2.5.2. Brain Volumes

Volumes of gray and white matter and extracerebral CSF excluding lateral ventricles were computed by multiplying the mean voxel value across the partial volume image by the total volume of that image (total volume = number of voxels × voxel size ($0.5\times0.5\times0.5$ mm^3)). The total brain volume was determined by summation of each tissue volume fraction, finally divided by 1000 to obtain brain volume in milliliters (mL).

5.2.5.3. Electrode-current to electric-field-strength Ratio

Based on the FEM model simulations, we calculated the ratio of the electrode current to the median FDI electric field strength, $I_{electrode}/E_{FDI}$, for each subject. This ratio is expected to be correlated with the individual MTs since it characterizes the amount of current that has to be applied so that the FDI region in motor cortex reaches an approximately fixed neural activation threshold. The underlying assumption here is that the electric field threshold for neural activation, estimated by the median E_{FDI} value at the individually-titrated MT current, is comparable across subjects and would be expected to have less interindividual variability than

the individual MTs. The extent to which this is the case will be evaluated as described in Section 5.2.4.

5.3. Results

5.3.1. Individual TES Head Models

The four individualized NHP head models (subjects MA, CH, DY, and RZ) used for the TES electric field simulation are displayed in Figure 5.1. The segmented tissue regions corresponding to skin, muscle, vertebrae, skull compacta, sclera, gray matter, lens, eyeball, optic nerve, spinal cord, and white matter as well as the RUL electrode montage are labeled in Figure 5.1. Inter-electrode (electrode center-to-center) geodesic distances for subjects MA, CH, DY, and RZ were estimated to be about 53.7, 46.7, 57.9, and 47.3 mm, respectively, due to interindividual differences in anatomy between the four subjects.

5.3.2. Interindividual Variations in Electric Field Strength

The interindividual variation in electric field strength due to the anatomical differences between the subjects was investigated at fixed current amplitude of 800 mA (conventional current amplitude for ECT). Figure 5.2 shows descriptive statistics (1st, 25th, 50th (median), 75th, and 99th percentiles) of the electric field strength in the left and right brain regions for the four subjects. The median electric field values for the whole brain as well as the ratio between the

median electric field in the right and left brain are summarized in Table 5.1. Subject RZ has the highest median electric field strength (1.59 V/cm), whereas subject CH has the lowest electric field (1.01 V/cm), thus resulting in a 57% variation in median electric field value across the four subjects.

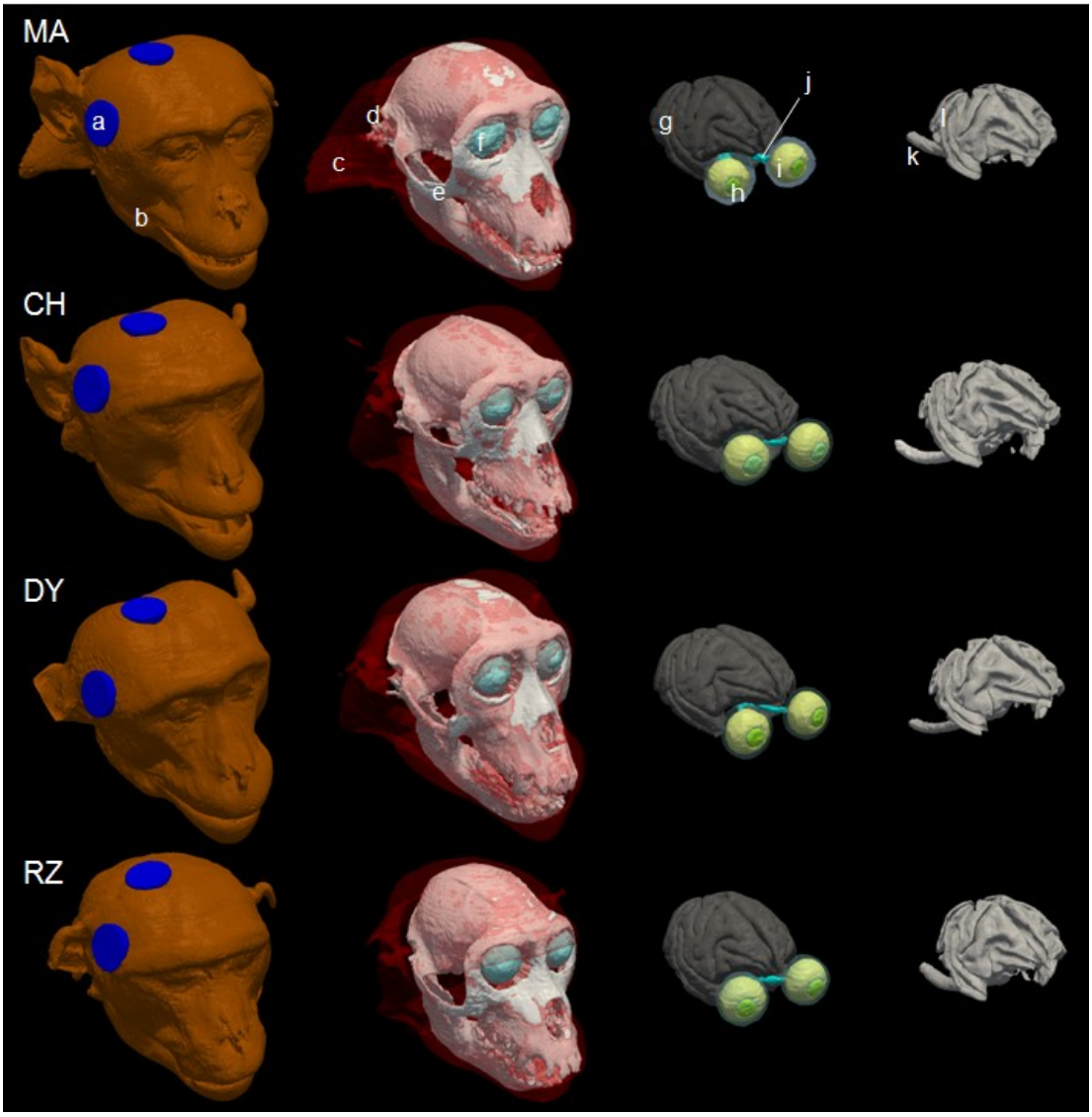

Figure 5.1. Individual TES head models of the four subjects (MA, CH, DY, and RZ, top to bottom rows, respectively). The various conductivity compartments are labeled including (a) RUL stimulation electrodes and tissue segmentation masks including (b) skin, (c) muscle, (d) vertebrae, (e) skull compacta, (f) sclera, (g) gray matter, (h) lens, (i) eyeball, (j) optic nerve, (k) spinal cord, and (l) white matter.

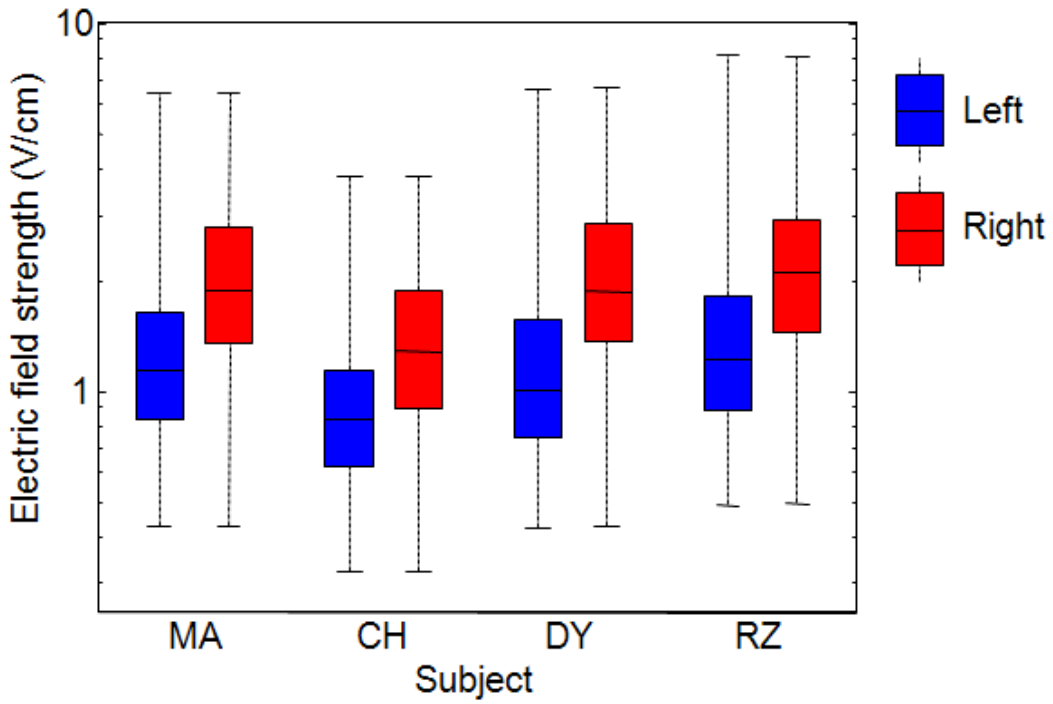

Figure 5.2. Descriptive statistics of the electric field strength in the left and right brain regions induced by the RUL electrode configuration at 800 mA current for the four NHP subjects. The electric field strength (y-axis) is shown on a logarithmic scale to normalize the skewed electric field distribution. Boxes indicate the interquartile range (25th to 75th percentile) with the median marked by a horizontal line, and whiskers delimit the 1st and 99th percentiles of the electric field distribution in the left and right brain regions.

Table 5.1. Median electric field strength (V/cm) in the whole brain and right-to-left brain median electric field ratio induced by RUL TES at 800 mA.

Subject	Whole brain	Right/left brain electric field ratio
MA	1.46	1.68
CH	1.01	1.54
DY	1.44	1.89
RZ	1.59	1.75

5.3.3. Neural Activation Threshold

The electric field threshold for neural activation was empirically estimated by coupling the simulated electric field strength induced in the brain with the measured MT. Figure 5.3(a) shows the RUL TES MTs for each subject. The average MT across the four NHP subjects is 80.33 mA, with a range of 50–120 mA (2.4-fold variation) and coefficient of variation of 0.37. The repeated measures analysis of variance (ANOVA) analysis of the combined dataset from all MT titration sessions yielded a significant difference on MTs between the four subjects ($F = 18.65$, $df = 3$, $p = 0.0006$). Figure 5.3(b) shows the corresponding estimates of the electric field threshold for neural activation for each subject, which are also summarized in Table 5.2. The average electric field threshold across the four NHP subjects is 0.45 V/cm (standard deviation = 0.07, coefficient of variation = 0.16). A comparison of the mean threshold values between the subjects shows that subject CH has the highest electric field threshold (0.52 V/cm), whereas subject MA has the lowest electric field threshold (0.35 V/cm). We found no significant effect of NHP subject on the electric field thresholds ($F = 3.15$, $df = 3$, $p = 0.0866$).

Table 5.2. Individual neural activation threshold (V/cm) for the four NHP subjects. SD: standard deviation

	MA	CH	DY	RZ	Mean (SD)
E_{th}	0.35	0.52	0.44	0.48	0.45 (0.07)

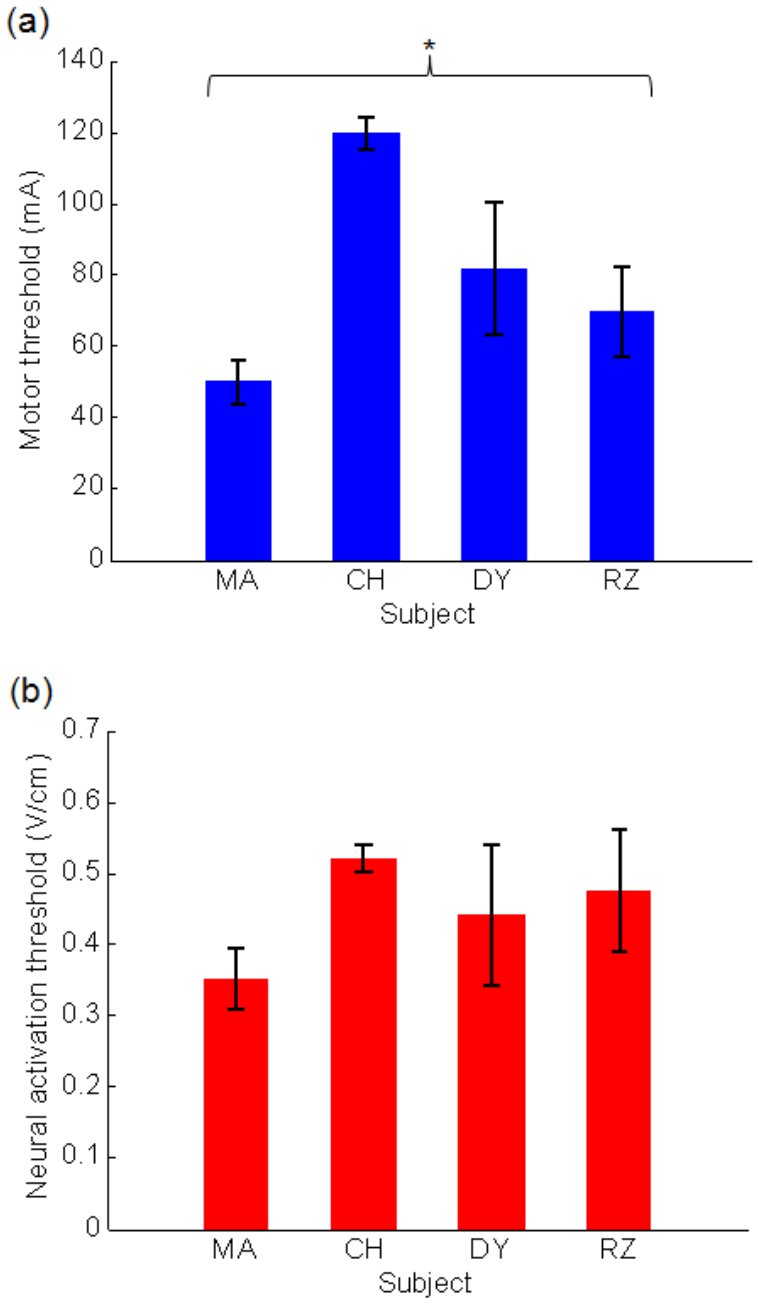

Figure 5.3. (a) Individual amplitude-titrated RUL TES motor threshold (MT) for 0.2 ms pulse width for the four NHP subjects. (b) Corresponding estimated electric field neural activation threshold in the motor cortex representation of FDI. Bars show mean values and error bars show standard deviations. An asterisk represents significant difference between the NHP subjects at a threshold of $p < 0.05$ in an ANOVA.

5.3.4. Electric Field Distribution at Motor Threshold

Figure 5.4 shows a set of representative views for the spatial electric field magnitude distribution at current strength corresponding to the individual MT for the four NHP subjects. The results in Figure 5.4 demonstrate that, as expected, the lateralized RUL electrode configuration predominantly stimulates the upper regions of the right hemisphere, thus yielding stronger electric field magnitude most localized to the right FDI areas of the motor cortex. Nevertheless, the detailed distribution of the electric field is complicated due to the complex electrical conductivity structure of the head and interindividual variations in the head anatomy.

5.3.5. Anatomical Correlates of Motor Threshold

Figure 5.5 shows individual maps of the distance from the skin surface to the cortex surface in the four subjects. The maps of the skin-to-cortex distance clearly indicate individual differences in anatomy. There are also differences in the skin-to-cortex distance at various points on the scalp—lateral areas have larger skin-to-cortex distance compared to the vicinity of the vertex.

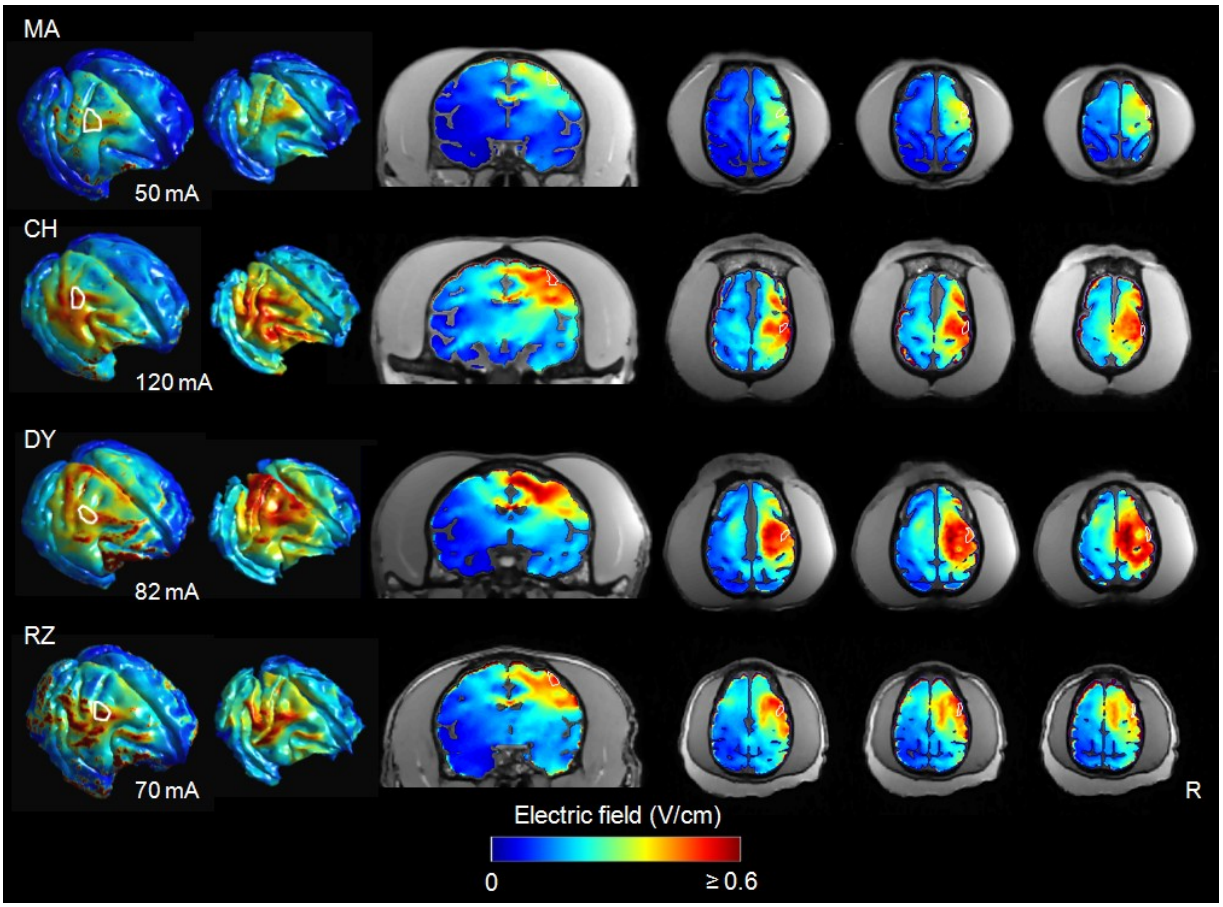

Figure 5.4. Electric field distribution at current strength corresponding to the individual MT for the four NHP subjects (top to bottom rows, respectively). Shown are electric field maps on the cortical surface (CSF–gray matter interface; first column), white matter surface (gray matter–white matter interface; second column), representative coronal slice (third column), and transaxial slices (fourth to six columns; 1.5 mm inter-slice distance). The structural MRI images of the extracerebral brain tissues are shown in gray around the slices as a reference to the anatomical results in Figure 5.6. Region-of-interest outlines in white show FDI motor area. Individual average MT is shown on the left below each row. R: right

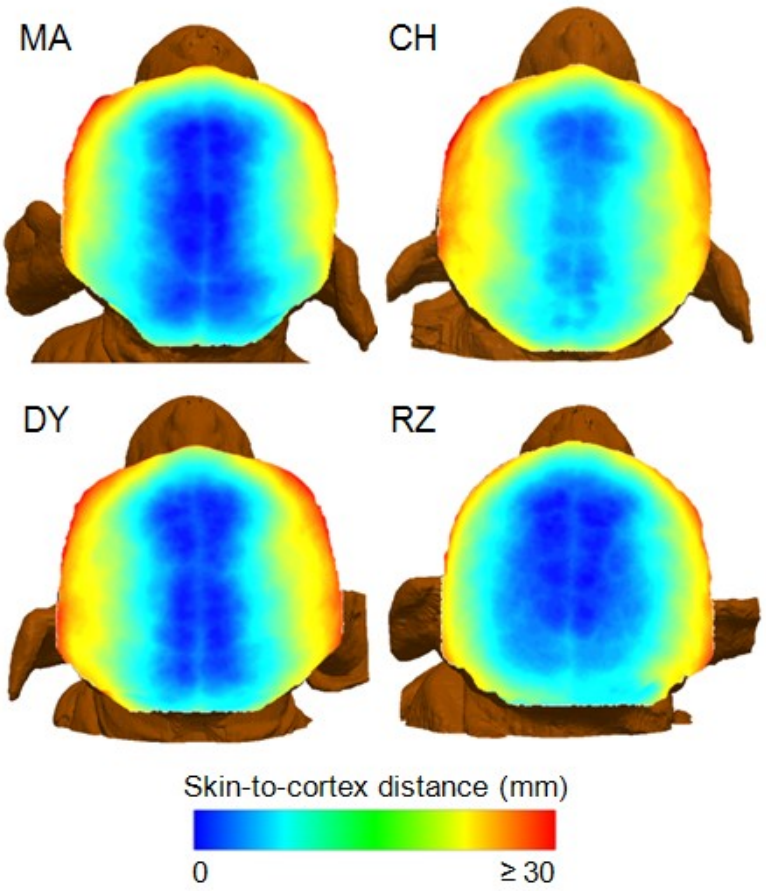

Figure 5.5. Maps of the distance from the skin surface to the cortex surface plotted overt eh head surface for the four subjects.

Figure 5.6 shows the correlation between the measured MT and various anatomical and electric field model measures. There are strong correlations ($r^2 > 0.92$, $p < 0.05$) between the measured MT and the superior electrode-to-cortex distance, vertex-to-cortex distance, brain volume, and $I_{electrode}/E_{FDI}$ ratio computed from the individual FEM simulation. On the other hand, there was no significant correlation between MT and the electrode-to-cortex distance for the right frontotemporal electrode ($r^2 = 0.27$, $p = 0.476$), which is 2–4 times further from the cortex than the superior electrode.

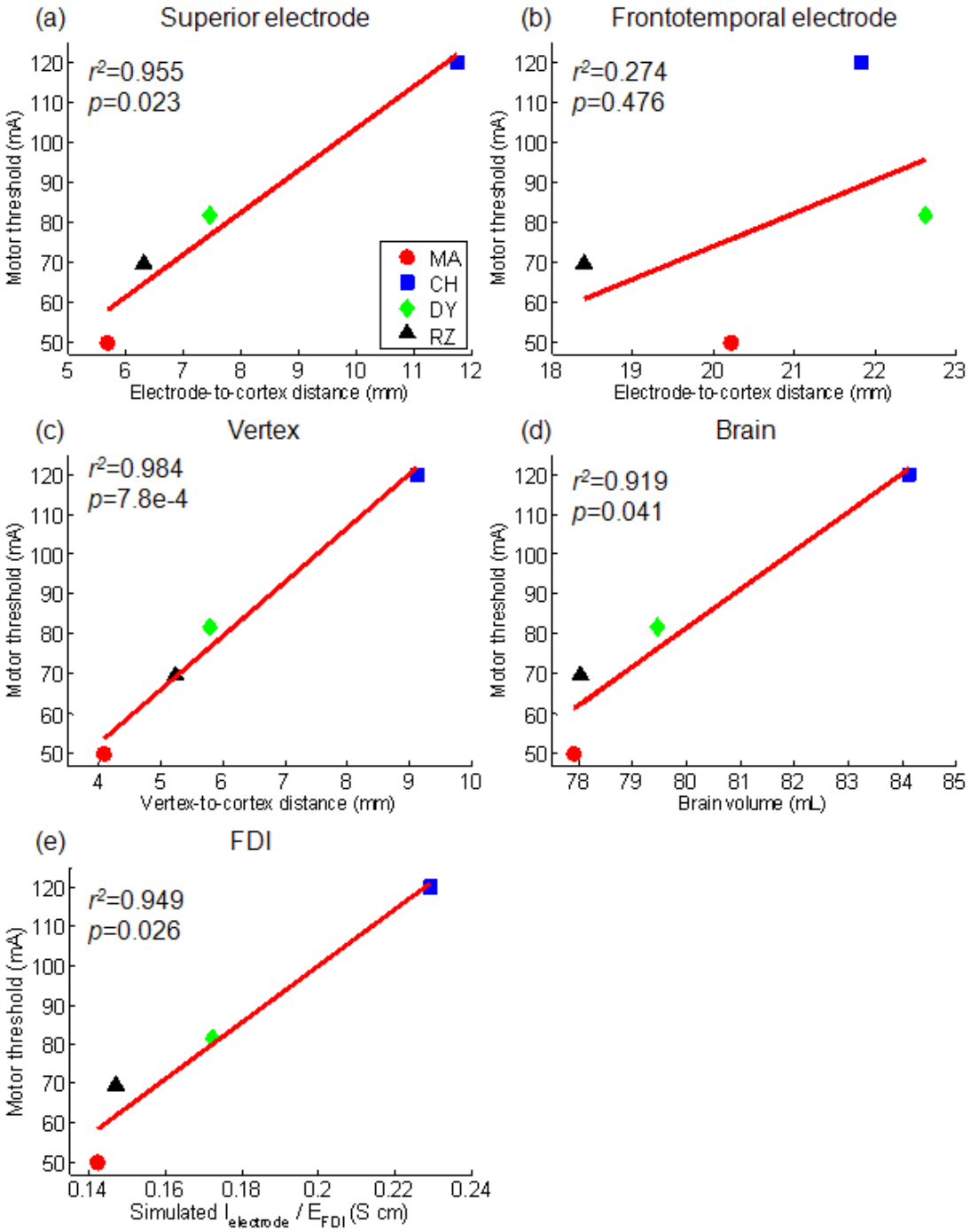

Figure 5.6. Correlation between average measured MT and electrode-to-cortex distance under (a) superior or (b) frontotemporal electrodes, (c) vertex-to-cortex distance, (d) individual brain volume, and (e) $I_{electrode}/E_{FDI}$ ratio computed from individual TES simulation models. Pearson's correlation r^2 and p values are given in each correlation plot.

5.4. Discussion and Conclusions

We presented an optimized processing pipeline intended particularly for generating an anatomically realistic FEM forward model of the NHP head incorporating complex tissue geometries and white matter anisotropic conductivities. Our modeling platform can be also used for modeling of other forms of brain stimulation such as TMS and transcranial direct current stimulation (tDCS). The spatial distribution of the electric field in a realistic NHP head model generated by TES has not been directly investigated. In this study, using the model developed, we (i) computed the spatial distribution of the electric field induced by the RUL ECT/TES electrode configuration in four NHP heads, (ii) examined the influence of anatomical differences on the electric field strength in the brain across multiple subjects at a fixed TES current amplitude, (iii) estimated the neural activation threshold by coupling the simulated electric field strength with individually-titrated RUL TES MT, and (iv) showed that individual anatomical variability as captured by structural MRI and the electric field model predicts individual differences in MT. This work represents the first computational study investigating the electric field characteristics of TES with RUL electrode configuration concurring with ECT stimulation paradigm using high-resolution realistic models of the NHP subjects.

5.4.1. Interindividual Variation in Electric Field Strength Stemming from Anatomical Variability

Our findings clearly reveal that the spatial distributions of the electric field vary due to anatomical differences across four NHP subjects. The results shown in Figure 5.2 (1.6-fold variation in electric field strength in the whole brain) are consistent with a published modeling study in the context of transcranial direct current stimulation (tDCS) that reported 1.5-to-3-fold variations in peak cortical current density in normal human subjects [231], and extra ~10% variability in peak cortical current density by virtue of the head fat in obese individuals [234]. Moreover, it was reported that head anatomy difference resulted in ~2.4-fild variation in peak cortical electric field strength during tDCS in healthy human individuals [228]. It is well-established that variations in head anatomy and tissue layer thickness influence the electric field/current density fields in the brain during TES [116, 231, 234, 253]. Our results support that morphological and anatomical difference in head anatomy is a significant source of the electric field/current density variability in TES. As such, applying the identical stimulus current amplitude and electrode montage to varied populations, such as distinct age or gender groups, can result in variable patterns of electric field/current density in the brain, yielding inconsistent clinical outcomes that include therapeutic efficacy and adverse side effects. In this regard, we have proposed that individualizing and lowering current amplitude could serve as a means of compensating for interindividual variability in head geometry and neurophysiological

excitability, thus expecting to reduce side effects and clinical outcome variability [111, 116, 226, 227].

5.4.2. Neural Activation Threshold

Based on the individual MTs of the left FDI muscle and the individual realistic electric field models, the neural activation threshold was estimated to be 0.45 ± 0.07 V/cm for the 0.2 ms rectangular pulses. The electric field threshold from previous studies using TMS with a figure-8 coil ranges from 0.3 to 1.3 V/cm [254-257]. The MT elicited by TES in anesthetized humans produced the electric field threshold range of 0.45-1.12 V/cm for the 0.05 ms pulse width [258]. Despite differences in stimulation modality or stimulus current parameters (e.g., pulse wide and current amplitude/polarity), our estimates of the electric field threshold for neural activation are consistent with previous modeling and experimental measurements [254-258]. On the other hand, our previous work reported the neural activation threshold estimate as 0.29 V/cm for the 0.2 ms pulse width [117]. This value is lower than the average electric field threshold (0.45 V/cm) estimated in the present study. This discrepancy could be explained by the fact that the results in that study were estimated based on the average human TMS MT data for the figure-8 coil from the literature.

We observed the variation in the neural activation threshold (16%) across subjects that is smaller than the variation in the MT (37%), indicating that the individualized FEM models indeed account for interindividual differences in head anatomy. Further, possible errors in the modeling of the precise electrode position on the scalp may yield errors in the electric field threshold estimates. The variability in the neural activation threshold estimate could be also

explained by individual differences in neural excitability or brain anatomy in the FDI motor area, and/or to modeling errors. Furthermore, we cannot exclude that neural stimulation may have occurred along the corticospinal tract away from the cortical representation of FDI. Nevertheless, the strong correlation between the MT and the electric field in the cortical FDI control area as well as the superior-electrode-to-cortex and vertex-to-cortex distances, as shown in Figure 5.6, does support cortical origin of the MEPs.

5.4.3. Individual Differences in TES MT are Correlated with Anatomical Variability

The MT is traditionally used to measure the excitability of cortical neurons and corticospinal pathways in TMS studies despite a remarkable variation both within an individual subject and between subjects [259]. It is already used as a standard in the TMS field to standardize the simulation intensity across subjects [235]. It has been reported that the coil-to-cortex distance or scalp-to-cortex distance affect the MT in response to TMS [260-266]. Individual scalp-to-cortex distance has been considered as a significant determinant of interindividual variations in TMS-elicited MT [263-267]. In addition to previous studies based on TMS, it is of particular interest to study whether individual differences in MT elicited by TES could be explained by individual anatomical variability. To address this question, here we examined the correlation between several anatomical variables and individually determined MT data. We found that interindividual variation of the TES-elicited MT is significantly correlated with the variation in skin-to-cortex distance under the superior electrode center and at vertex, and in individual brain volume, but not

skin-to-cortex distance under the right frontotemporal electrode center. The lack of correlation between individual MT and the distance between the frontotemporal electrode and cortex could potentially be explained by the significantly larger electrode-to-cortex distance at that location compared to the vicinity of vertex. This may be due to the large lateral muscles in the NHP head, which result in less penetration of the electrode current into the intracranial space at lateral in comparison to superior locations. The large variations of the skin-to-cortex distance at superior and lateral regions are clearly shown in Figures 5.4 and 5.6(a). This may also relate to the longer distance between the lateral electrode and the FDI cortical motor area. The distance between the electrode and cortex is a critical anatomical parameter to determine the optimal TES current, since electrical current delivered by TES travels through the various head tissue compartments, as shown in Figure 5.1, to excite sufficient volume of the brain. If the electrode-to-cortex is small, low stimulus current will be sufficient to elicit the physiological activity, whereas the identical current will not induce any activity at longer distance.

Of note, this study revealed that the $I_{\text{electrode}}/E_{\text{FDI}}$ ratio determined using individualized electric field models is significantly correlated with individual MT. This strong correlation between the MT and the simulated $I_{\text{electrode}}/E_{\text{FDI}}$ ratio suggests that the subject-specific computational models could predict variations in the individual current required for neural stimulation in TMS, ECT and in other transcranial stimulation applications. These findings do suggest that to compensate for individual anatomical variability, either individual MRI, individual MT, or individual electric field simulation could be used to choose the individual ECT current amplitude. This concept should be tested clinically.

5.4.4. Limitations and Future Work

Several potential limitations need to be addressed. First, despite potential significance of the present study, possible source of errors related to use of electric field models includes uncertainty in tissue electrical conductivity. It is well-established that the accuracy of the electric field/current density fields induced in the head by TES is influenced by tissue electrical properties [68, 98, 116, 235]. Since direct and non-invasive *in-vivo* conductivity measurements still remain a challenging problem, a number of published modeling studies have used a wide range of tissue conductivity values reported in the literature. It should be noted that variation in tissue conductivity can contribute to inaccuracies of the simulated electric field/current density fields in the head. Furthermore, other important factors (e.g., tissue segmentation or head anatomy variations) that are potential sources of electric field/current density variability in the modeling studies were discussed in our previous paper (for the details see [68]). Nevertheless, in this paper the NHP head models incorporating the realistic WM anisotropic conductivity distributions and isotropic conductivities are sufficient to predict the electric field spatial distributions in an individual basis. In addition, the strong correlation between individual MT and the $I_{\text{electrode}}/E_{\text{FDI}}$ ratio determined from the RUL TES focal stimulation indirectly supports the validity of our developed model [228, 232, 233].

Second, the small number of subjects in the present study could affect the correlation and statistical analyses. Based on our correlation results from four NHP subjects, our interpretation concerning the issue if individual anatomical variability is predictive of individual differences in TES MT should be cautious in drawing generalized conclusion. Nonetheless, we presented significant strong correlations between individual anatomical factors and individual MT. We also conducted multiple experiments to measure individual MT in each subject and created the

individual FEM computational models for each subject based on the individual MRI and DTI. Therefore, we believe the present results do provide important insight that can be confirmed and expanded in future studies in larger populations.

We also estimated the neural activation threshold that is independent of the electric field direction. It is known that the electric field direction relative to the stimulated neural population may influence the neural activation threshold [117, 214]. Inclusion of the electric field direction would affect our estimates of neural activation threshold, thus the spatial patterns of electric field stimulation strength estimate. Nevertheless, as discussed in section 5.4.2, this study represents the first attempt at deriving the neural activation threshold by linking empirically measured MT with the simulated electric field magnitude from the realistic NHP models. If the electric field direction data becomes available in future studies, it can be easily incorporated with our electric field models. Our model incorporating white matter anisotropic conductivity can also provide more accurate electric field directional information compared to the model with fully isotropic conductivity.

In summary, we developed the high-resolution individual-specific FEM models of the NHP heads for the purpose of predicting the electric field strength in the brain generated by the RUL electrode configuration. Knowledge of the electric/current density field characteristics derived from such realistic head models can help to interpret the existing ECT paradigms, and can be useful in optimizing stimulation techniques. This study indeed presents that the NHP animal models could be used to characterize the induced electric field distributions in the brain at individually-titrated MT and to derive an empirical estimate of the electric field threshold for neural activation in conjunction with physiologically measured TES MT. Ultimately, this work

may guide the development of a novel therapeutic intervention for the treatment of major depression and other psychiatric disorders.

Chapter 6

Electric Field Characteristics of ECT with Individualized Current Amplitude

6.1. Introduction

Electroconvulsive therapy (ECT) remains the most effective treatment for severe major depression [79, 80]. ECT induces a generalized seizure under anesthesia by delivering electric current to the brain via electrodes placed on the scalp. However, the biophysical mechanisms responsible for the effects of ECT are still unknown, and the use of ECT is impeded by cognitive side effects such as amnesia [20]. Various ECT technique modifications have been proposed to reduce adverse side effects of ECT while maintaining therapeutic efficacy. For example, the shift from sine wave to rectangular brief pulses [27, 107, 268] as well as the shift from brief to ultrabrief pulse width [36, 269, 270] resulted in diminished side effects of ECT without sacrificing efficacy. Moreover, high dose right unilateral (RUL) ECT represented a comparable efficacy to bilateral frontotemporal (BL) ECT with a significant decrease in amnesia [112].

Bifrontal (BF) and an experimental frontomedial (FM) configuration have been proposed to preferentially focus the electric field in prefrontal regions to maximize efficacy and limit side effects [79, 227, 271]. However, there is still limited knowledge of how to optimally determine the dosing of ECT. The ECT dose includes electrode placement/shape and stimulus current parameters (e.g., current amplitude or polarity) that affect the electric field induced in the brain [111]. The distribution of the electric field in the brain also depends upon the geometry of the head and electrical properties of head tissues [68, 116, 117, 227].

In practice, ECT is applied with a fixed high current amplitude of 800 or 900 mA for all patients [111]. The high, fixed current amplitude in conventional ECT produces widespread direct stimulation in the brain that exceeds the neural activation threshold by several fold, potentially contributing to side effects [68, 111, 117, 217]. Furthermore, using a fixed current amplitude in conventional ECT for all patients may lead to variable clinical outcomes due to individual anatomical and neurophysiological variation [111]. Indeed, there is considerable variability in clinical outcomes, including efficacy as well as adverse cognitive side effects, which at present do not have a known anatomical or physiological explanation. Therefore, we have proposed that lowering and individualizing stimulus current amplitude could serve as a means of reducing side effects and clinical outcome variability [217, 226, 227, 271]. Reduced ECT current amplitude improves the focality of stimulation, potentially decreasing side effects of seizure therapies [111, 217, 227, 272, 273]. Lowering the current amplitude could avoid direct hippocampal stimulation, potentially reducing adverse effects on memory [274]. However, the capability of these paradigms to focus on the electric field strength coupled with *in vivo* neurophysiological data has not been fully demonstrated.

Knowledge about the strength and spatial distribution of the electric field induced by ECT may help to unravel the mechanisms determining the efficacy and side effects seen with various ECT paradigms, and may inform novel techniques for improvement of spatial targeting of ECT which could lead to improved risk/benefit ratio [68]. However, the electric field distribution alone is insufficient to characterize the degree of induced neural stimulation, since the neural response is also dependent on other parameters such as the pulse shape and width [111, 117]. To overcome this limitation, we proposed previously, using a spherical head model, an electric field model incorporating a waveform-specific neural activation threshold to determine the suprathreshold direct stimulation strength and volume (focality) in ECT [117, 217]. This approach allows us to reveal what brain areas are directly stimulated by various stimulation modalities, and to compare stimulations with different pulse characteristics such as between brief and ultrabrief pulse ECT [117]. The spherical model consisting of several layers of concentric spheres, however, cannot account for detailed anatomical tissue features, individually variable head geometries, and anisotropic tissue properties. The electric field solution computed from significantly simplified spherical model is approximate. Thus, the interpretation about the electric field characteristics in the brain generated by the spherical electric field model should be careful, and simple extrapolation from the spherical head modeling studies may be inadequate. Furthermore, that study used a neural activation threshold estimated from the literature.

Investigations using invasive or noninvasive brain stimulation techniques in macaques have provided us with extensive knowledge about the functional or structural organization of the primate brain. The macaque monkey model has been becoming a rational basis for much of our understanding of the human brain. Indeed, nonhuman primate (NHP) models have proven to be valuable for advancing our understanding of the human brain in convulsive therapies [82, 229],

for optimizing ECT stimulation parameters for efficient seizure induction [226], and for characterizing neurophysiological effects of electrically and magnetically induced seizures [230].

In this Chapter, we aim to investigate the electric field characteristics of various forms of ECT with individualized current amplitude in four NHP subjects. The electric field distributions in the brain induced by the various ECT modalities including the BL, BF, RUL, and FM ECT electrode configurations are computed in anatomically realistic finite element models of four NHP heads. We estimate the neural activation threshold from individually measured motor threshold (MT) and simulated electric field strength. For each ECT electrode configuration, we determine the stimulation strength and focality relative to an empirical electric field threshold for neural activation at individually-titrated seizure threshold (ST) and at fixed current amplitude corresponding to the average ST. We quantify the focality of stimulation to evaluate the effect of the stimulus current amplitude on the brain volume stimulated above the neural activation threshold. Understanding the induced electric field characteristics and their individual variability could help identify potential causes of the differences in clinical outcome, and could support the development of ECT dosing paradigms with fewer side effects. Preliminary results from this study were previously presented in part in conference proceedings [227, 273].

6.2. Materials and Methods

We simulated the electric field induced by ECT in realistic finite element NHP head models using the same methods described in Chapters 2 and 5. The modeling methods are described in detail in Chapters 2 and 5 and are summarized here.

6.2.1. ECT Head Model Generation

In Chapters 2 and 5, we described an optimized processing pipeline for generating a realistic finite element model of a NHP head incorporating tissue heterogeneity and tissue conductivity anisotropy [227, 273]. The processing framework consists of four main components: image preprocessing, tissue segmentation, stimulation electrode placement, and finite element mesh generation.

The preprocessing of the structural MRI images includes image resampling (0.5×0.5×0.5 mm^3 voxel), anterior and posterior commissures (AC-PC) spatial alignment, bias field correction, nonlinear anisotropic diffusion filtering, and skull stripping [71, 227]. Next, individual tissue probability maps corresponding to gray matter, white matter, and cerebrospinal fluid (CSF) were automatically produced using SPM8 (Wellcome Department of Cognitive Neurology, Institute of Neurology, University College London, UK, http://www.fil.ion.ucl.ac.uk/spm) based on the 112RM-SL macaque tissue priors [77]. Manual segmentation of the non-brain regions into 11 tissue compartments, representing skin, muscle, skull spongiosa, skull compacta, vertebrae, spinal cord, lens, eyeball, sclera, optic nerve, and sinus, was carried out using a combination of tools from the ITK-SNAP software [75] and an in-house morphological processing algorithm [57, 68, 71]. Subsequently, we modeled three standard ECT electrode placements (BL, BF, and RUL) [79, 80] and an investigational configuration (FM). Two round electrodes were modeled for the BL (3.5 cm diameter) and BF, RUL, and FM (2.5 cm diameter, respectively) ECT configurations (see Figure 6.1). For BL ECT, the two electrodes were placed bilaterally at the frontotemporal positions located at 2 cm above the midpoint of the line connecting the external canthus and tragus [80]. For BF ECT, the electrodes were positioned bilaterally 2.5 cm above the outer angle of the orbit on a line parallel to the sagittal plane. For RUL ECT, one electrode was

placed in the right frontotemporal position and the other electrode was centered 1.25 cm to the right of vertex [80]. For FM ECT, the two electrodes were placed medially on the forehead and posterior to vertex, respectively. Finally, adaptive finite element meshes were generated for each subject using the restricted Delaunay tessellation algorithm [88], resulting in the four subject-specific ECT finite element models of the rhesus macaque heads and electrodes, each consisting of approximately 1.8 million tetrahedral elements.

6.2.2. Electric Field Computation

To compute electric field strength induced by each of the four different ECT electrode configurations, the dielectric properties of tissues were incorporated into the ECT models. The volume conductor models were created by assigning the anisotropic electrical conductivities into the white matter regions, and the isotropic conductivities into all the other tissue compartments. The isotropic electrical conductivity values are listed in Table 2.1. The white matter anisotropic conductivity tensors were derived by means of a direct transformation approach with volume normalization [57, 93-97]. The electric field distribution in each ECT head model was obtained by solving the quasi-static Laplace equation using the preconditioned conjugate solver with a relative tolerance of 1×10^{-8} within ANSYS (ANSYS Inc., Canonsburg, PA, USA) [68].

6.2.3. *In Vivo* Motor and Seizure Threshold Titration

Four different ECT electrode montages for *in vivo* MT and ST titration experiments corresponded to the conditions used in the individual ECT computational models. The

methodology of titrating MT and ST in NHPs was previously published by our group [226, 273, 274]. In summary, we determined the MT corresponding to the amplitude of a single pulse required to elicit a motor response in sedated NHPs, and the ST corresponding to the amplitude for a train of pulses to elicit a seizure in the same session for each of the ECT electrode configurations [226]. The NHP subjects were sedated with ketamine (5–10 mg/kg i.m.) and xylazine (0.35–0.7 mg/kg i.m.) [44]. The electrode sites were prepared by cleaning with alcohol to remove scalp oils and then rubbing with an abrasive gel (NuPrep, Weaver & Co., Aurora, CO) to reduce impedance. Thymapad adhesive electrodes (Somatics, LLC, Lake Bluff, IL) were cut down to 3.5 cm circles for BL and 2.5 cm circles for BF, RUL, and FM. MT and ST were titrated by stepping current amplitude (pulse width = 0.2 ms) in the anesthetized NHPs. For MT, electromyography was measured with needle electrodes from the first dorsal interosseous (FDI) muscle in both hands for all ECT conditions, but only from the left hand in the RUL ECT condition since the stimulation is predominantly unilateral in the right hemisphere [68]. The MT was determined for both current polarities. The MT was defined as the minimum stimulus pulse amplitude needed to achieve a 50 μV peak-to-peak motor evoked potential (MEP) for at least five out of ten trials.

ST was determined by an ascending method-of-limits titration of the stimulus pulse amplitude, while holding all the other stimulus parameters fixed. The stimulus train consisted of 500 pulses delivered at 50 pulses per second resulting in train duration of 10 s. ST titrations for BL and RUL ECT used unidirectional pulse trains (cathode on right side) whereas the ST titrations for BF and FM ECT used a conventional bidirectional train (alternating pulse polarity). Seizures were determined by observing the motor seizure manifestations in the left arm and the

EEG as a secondary criterion. The MT and ST titration was repeated three times for each ECT condition in each subject.

6.2.4. Stimulation Strength and Focality Analysis

In addition to the electric field magnitude, other stimulation factors affecting neural response include pulse amplitude, shape, and width, and train frequency and duration [111]. The impact of the pulse waveform characteristics such as pulse shape and width on the induced electric field by ECT has been discussed in our previous study [111]. In this study, we aimed to examine the effect of pulse stimulus amplitude on the electric field strength and directly activated brain volume above threshold. The electric field magnitude is directly proportional to the ECT electrode current [111]. We calibrated the electric field magnitude to an empirically-derived neural activation threshold, E_{th}, by normalizing the electric field spatial distribution to that threshold, E/E_{th}. Such calibration of the electric field distribution to an empirically determined neural response threshold can largely take into account the various factors affecting the neural response listed above, and can partially compensate for inaccuracies in the tissue property modeling [111]. An individual neural activation threshold, E_{th}, was determined from the median electric field strength in the FDI representation of the motor cortex at stimulation current corresponding to the individual MT for the RUL electrode configuration, which produces electric field distribution most localized to the FDI areas [68, 227]. The electric field at threshold produces a weak motor response corresponding to the recruitment of a small fraction of neurons in the FDI regions of primary motor area [111]. The individual cortical FDI representations were

determined based on the monkey brain stereotaxic atlases [246, 247] and the Scalable Brain Atlas (http://scalablebrainatlas.incf.org).

We generated maps of the electric field strength relative to the threshold for neural activation by dividing the electric field magnitude distribution in the brain by the electric field magnitude corresponding to threshold motor response, and determined the stimulation strength and focality at individualized current amplitude corresponding to ST for each ECT electrode configuration in the four NHP subjects [117, 227]. This metric reflects the approximate level of neuronal depolarization relative to the action potential threshold [111, 117]. We quantified the focality of stimulation by the percentage of the brain volume that is exposed to electric field strong enough to produce suprathreshold depolarization in the majority of neurons, i.e., the volume where $E/E_{th} \geq 1$ [117, 227]. In addition, we evaluated the effect of current amplitude on the percentage brain volume stimulated above the electric field threshold as a function of current amplitude. Finally, to test whether current amplitude individualization could reduce inter-individual variability in head anatomy and neurophysiological excitability, we compared the coefficient of variation of the stimulated brain volume among the four subjects for individualized ST current amplitude as well as for fixed current amplitude corresponding to the average ST.

6.2.5. Finding Electric Field Correlates to Individual Differences in ECT Seizure Threshold

To test the hypothesis whether individual differences in ECT ST is predicted by subject-specific electric field computational models, we computed the ratio of the stimulation electrode current to

the median electric field strength in the whole brain, $I_{electrode}/E_{brain}$, for each ECT electrode configuration in each subject. This ratio characterizes individual amplitude-titrated ST variability from the ECT electric field simulation models, because the electric field strength in the entire brain was determined from the individual electric field model simulations, thereby reflecting individual anatomical variability. We then evaluated a linear correlation between $I_{electrode}/E_{brain}$ ratio resulting from individually-simulated electric field models and individually-titrated ST data.

6.3. Results

6.3.1. Individual ECT Head Models

The individual ECT head models used for the electric field simulation are displayed in Figure 6.1. Figure 6.1 shows the simulated conventional ECT electrode configurations including BL, BF, and RUL, as well as an investigational configuration of FM ECT in one representative NHP head model (subject CH). The segmented tissue regions corresponding to skin, muscle, vertebrae, skull compacta, sclera, gray matter, lens, eyeball, optic nerve, spinal cord, and white matter as well as the ECT electrode montages are labeled in Figure 6.1.

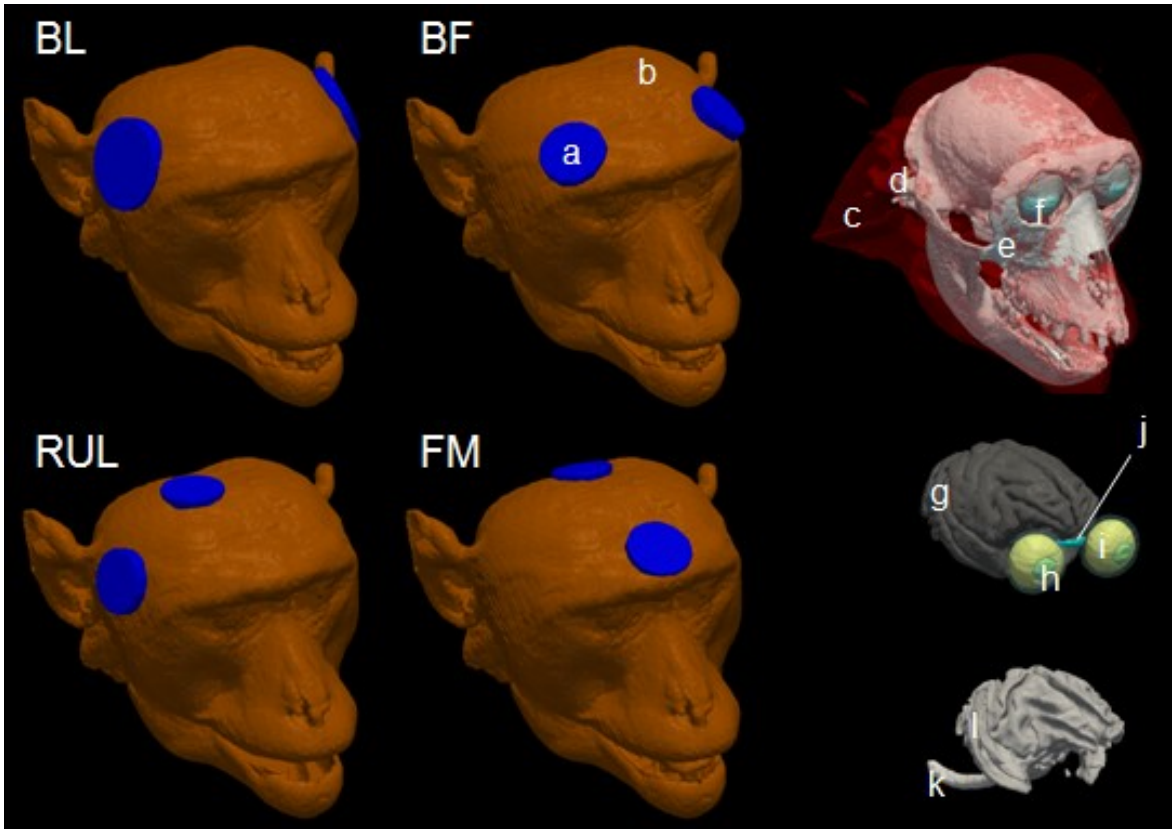

Figure 6.1. Representative individualized ECT models (subject CH) for the bilateral frontotemporal (BL), bifrontal (BF), right unilateral (RUL), and frontomedial (FM) ECT electrode configurations (left and middle columns). The various conductivity compartments are labeled including (a) ECT stimulation electrodes and tissue segmentation masks including (b) skin, (c) muscle, (d) vertebrae, (e) skull compacta, (f) sclera, (g) gray matter, (h) lens, (i) eyeball, (j) optic nerve, (k) spinal cord, and (l) white matter (right column).

6.3.2. Electric Field Distribution Relative to Neural Activation Threshold

Table 6.1 gives the individually measured RUL MTs and the amplitude-titrated STs for the four ECT electrode configurations in the four NHP models. All values are the

Table 6.1. Individually measured average motor threshold (mA) and average seizure threshold (mA) for the four ECT electrode configurations in the four NHP subjects. SD: standard deviation

Subject	Motor Threshold (mA)	Seizure Threshold (mA)			
	RUL	BL	BF	RUL	FM
MA	0.43	111	89	107	89
CH	0.32	215	190	284	141
DY	0.0063	222	196	190	128
RZ	0.04	164	146	141	92
Mean (SD)	0.14	178 (52)	155 (50)	181 (77)	113 (26)

averages of the three measurements. Based on the median electric field strength in the FDI area for RUL at MT, we estimated the individual neural activation threshold to be E_{th} = 0.35, 0.52, 0.44, and 0.48 V/cm for subject MA, CH, DY, and RZ, respectively. Average electric field threshold for neural activation across four subjects is 0.45 V/cm (standard deviation = 0.07). The individual electric field threshold for each subject was used to determine the electric field stimulation strength and focality for all ECT electrode configurations.

Figure 6.2 shows maps of the E-field strength relative to the neural activation threshold at current strengths corresponding to individually amplitude-titrated STs (see Table 6.1) for the various ECT electrode configurations in the four NHP models. The simulated conventional ECT electrode montages including BL, BF, and RUL, as well as an investigational configuration of FM ECT for sample subject CH are displayed (top row). The maps of the E-field magnitude distributions relative to the neural activation threshold at current amplitudes corresponding to individual STs are visualized on the surface (gray matter-white matter interface) as well as in a representative coronal slice for each individual subject. A qualitative comparison of the electric

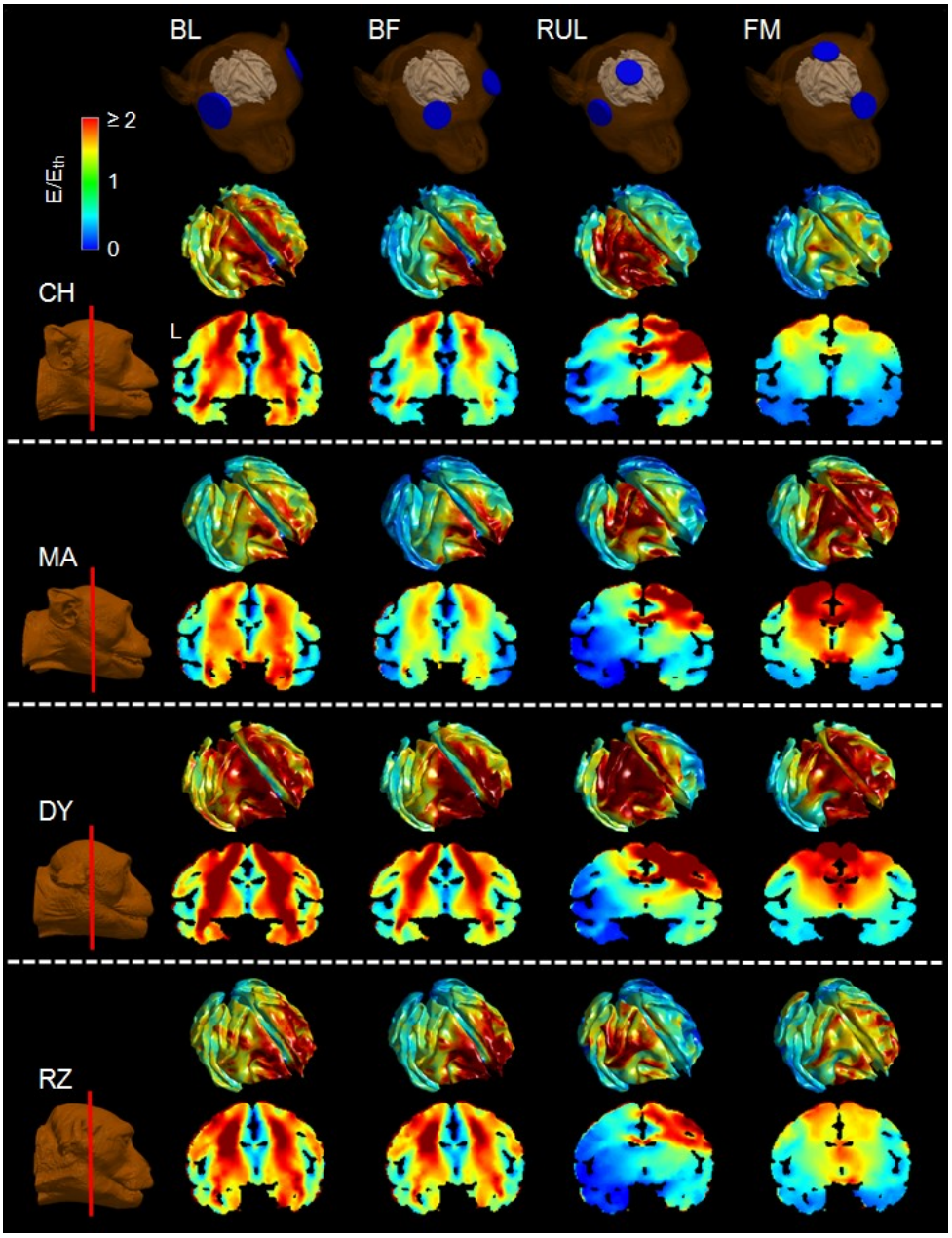

Figure 6.2. Electric field stimulation strength relative to neural activation threshold (E_{th}) at current amplitude corresponding to amplitude-titrated ST (see Table 6.1) for BL, BF, RUL, and FM ECT configurations (second to fifth columns, respectively) in four NHP models—subject CH, MA, DY, and RZ (top to bottom rows). Representative ECT simulation models (subject CH) are shown (top row). Electric field distributions relative to individual threshold at individual ST are plotted on the surface (gray matter-white matter interface) and in a representative coronal slice. The E/E_{th} color map is clamped at an upper limit of 2 for good visibility of the electric field stimulation. L: left.

field stimulation strength relative to the threshold for neural activation indicates that the symmetric ECT electrode configurations (BL, BF, and FM) stimulate comparable brain volume in both hemispheres. On the other hand, the asymmetric RUL electrode configuration directly activates the right brain regions while sparing the left brain sides.

6.3.3. Effect of Current Amplitude

Figure 6.3 shows the effect of current amplitude on the percentage of the brain volume with electric field strength above the neural activation threshold for the four ECT electrode configurations. Both averages and standard deviations of the stimulated brain volume above threshold across four subjects are plotted for all ECT electrode configurations. At individual STs (100% ST), the results in Figure 6.3(a) indicate that BL ECT stimulates, on average, the largest brain volume (63 ± 10%), whereas RUL ECT produces the most focal stimulation (25 ± 7%). An experimental FM configuration at ST stimulates the brain volume (36 ± 14%) that is slightly smaller than that by BF ECT (40 ± 11%). The induced electric field distributions vary linearly with current amplitude. Thus, the electric field stimulation strength relative to the neural activation threshold and directly stimulated brain volume are controlled by the current amplitude. As a result, the directly stimulated brain volume above threshold increases with higher current amplitude as shown in Figure 6.3(b), indicating that lowering the current amplitude reduces the activated brain volume. Consistent with the results in Figure 6.3(a), BL ECT activates the largest brain volume, while RUL is the most focal for a range of ST current amplitudes.

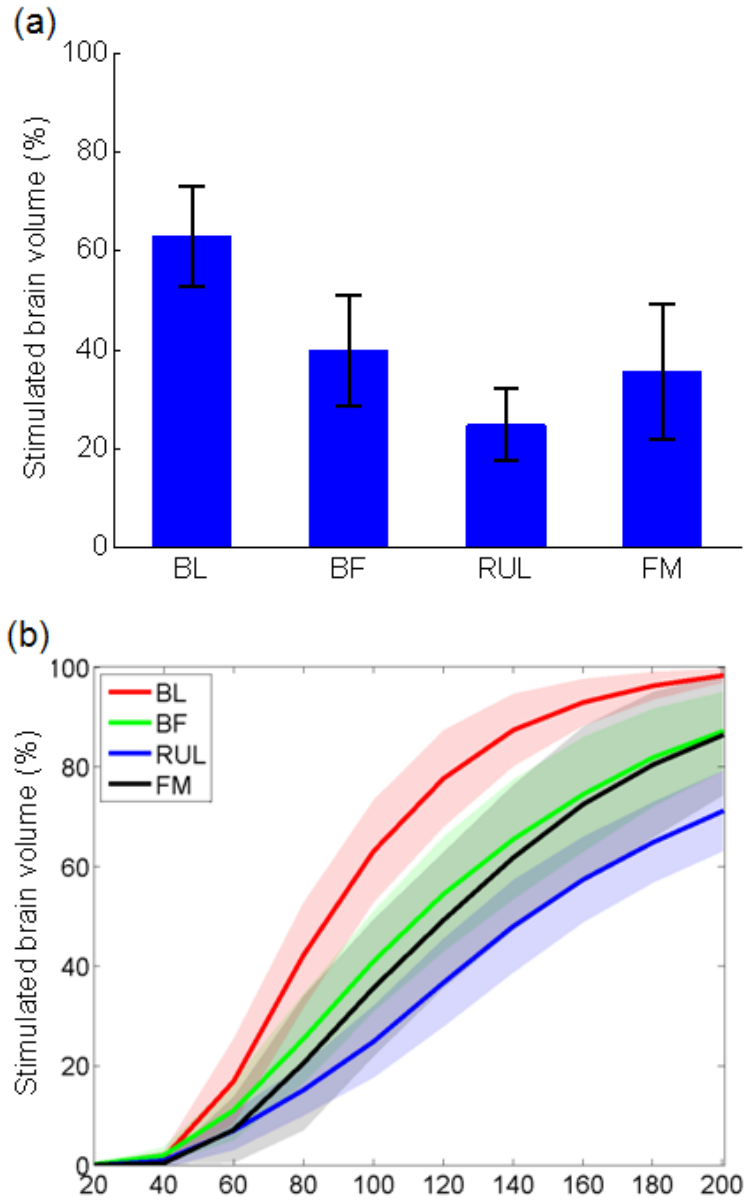

Figure 6.3. Effect of current amplitude on the percentage directly stimulated brain volume above the neural activation threshold ($E \geq E_{th}$) (a) at individual STs (100% ST) and (b) as a function of current amplitude (pulse width = 0.2 ms) relative to the neural activation threshold for the BL, BF, RUL, and FM ECT electrode configurations. In (a), averages and standard deviations (error bars) of directly stimulated brain volume at individual STs across four subjects for each ECT electrode configuration are plotted. In (b), each color band represents the averages (solid lines) and standard deviations (shades) of the percentage stimulated brain volume across four subjects for each ECT electrode configuration with a range of current amplitudes.

6.3.4. Effect of Current Amplitude Individualization

Figure 6.4 compares the coefficient of variation of the stimulated brain volume above the threshold among four subjects between ECT with individualized and group-average (fixed) ST current amplitude. Group-average ST current strengths for each ECT electrode configuration were used as the fixed current amplitude for estimating the directly stimulated brain volume above threshold (see Table 6.1). The results in Figure 6.4 indicate that for all ECT electrode configurations, individualized current amplitude results in less variability of the stimulated brain volume across subjects (16-39%) compared to ECT with fixed, average ST current amplitude (29-64%).

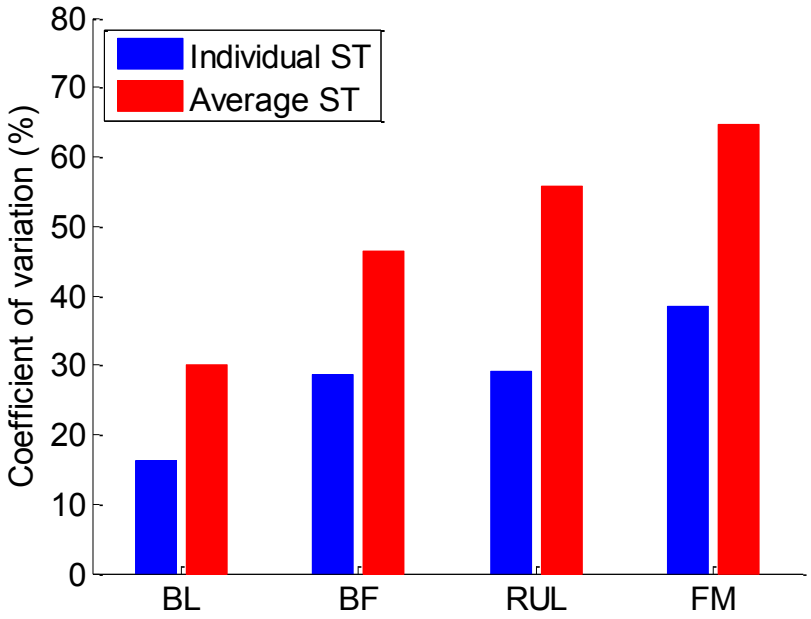

Figure 6.4. Comparison of coefficient of variation of the stimulated brain volume above threshold among four NHP individual models between ECT with individual and group-average (fixed) ST current amplitude for the four ECT electrode configurations.

6.3.5. Electric Field Correlates of Individual Differences in ECT Seizure Threshold

The interindividual variation in electric field strength due to the differences in head anatomy and size between the four subjects was examined at fixed current amplitude of 800 mA. Figure 6.5 shows averages and standard deviations of the median electric field magnitude in the whole brain across four NHP models. The averages of the median electric field strength across four subjects are 2.2, 1.9, 1.4, and 2.6 V/cm for the BL, BF, RUL, and FM ECT electrode configurations, respectively. Furthermore, we found that there is 1.22-, 1.47-, 1.57-, and 1.90-fold variation in the median electric field magnitude between the four individual subjects for the BL, BF, RUL, and FM electrode configurations, respectively. The variation of the electric field magnitude implies the variability of the electric field characteristics in the brain due to the head anatomical differences. Using the electric field strength in the whole brain at simulated electrode current, we tested the hypothesis if individual differences in ECT ST can be explained by the individual electric field variability.

Figure 6.6 shows the correlation between the $I_{electrode}/E_{brain}$ ratio computed from the individual ECT simulation models and the amplitude-titrated ST. We found there is no significant correlation between the individual electric field strength and individual ST data, but there is a positive correlation trend (r^2=0.665-0.902) for all electrode configurations that does not reach significance likely due to the small number of subjects.

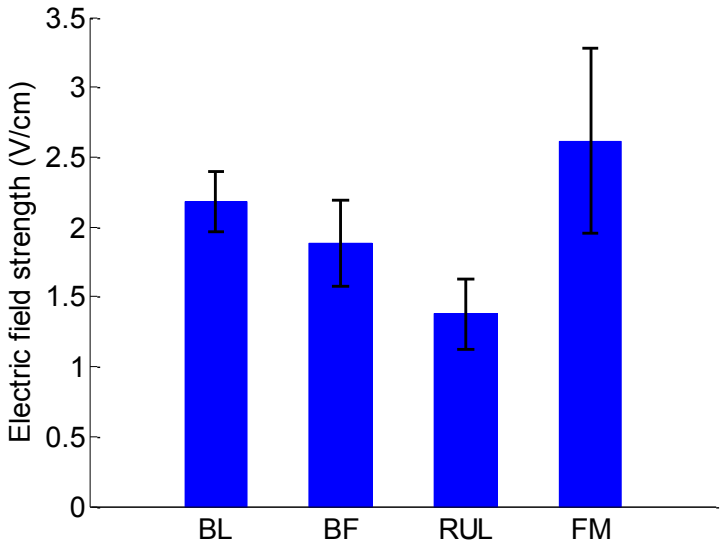

Figure 6.5. Averages and standard deviations (error bars) of the median electric field strength in the whole brain across four NHP head models at 800 mA current.

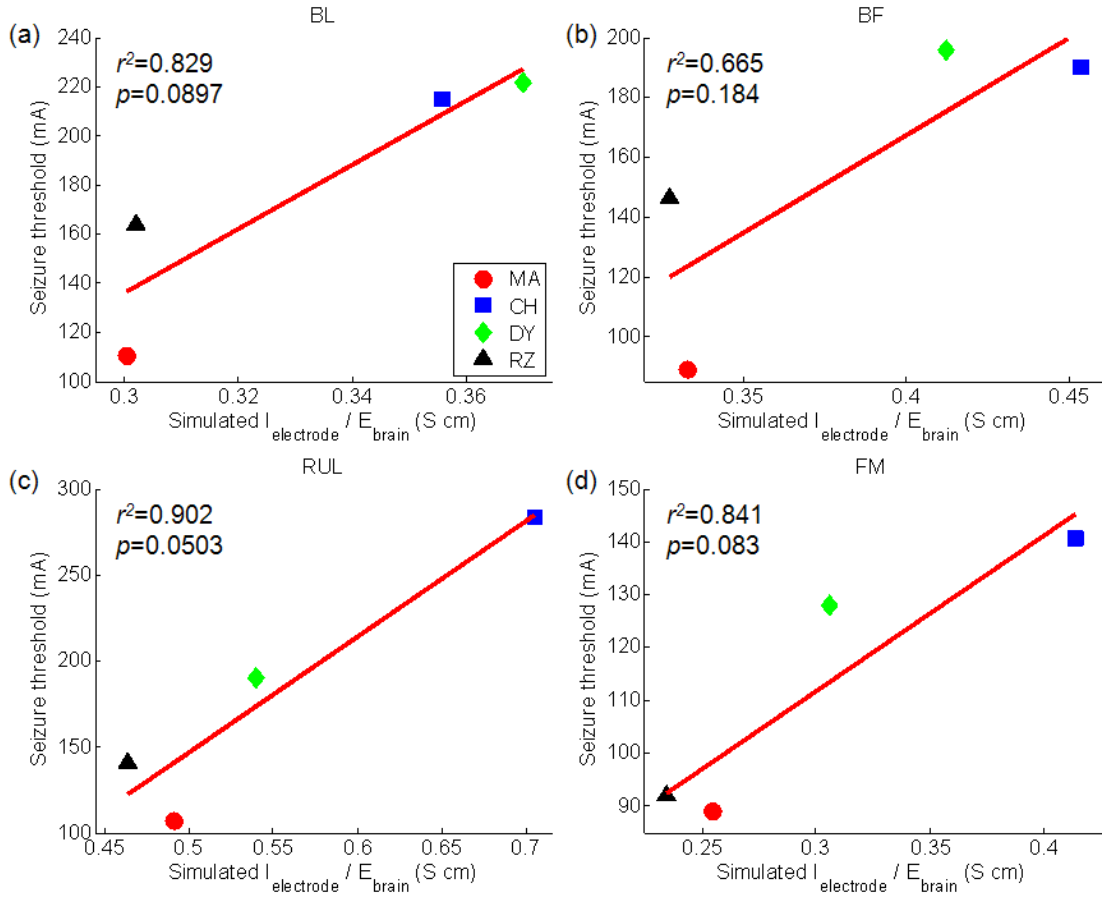

Figure 6.6. Correlation between amplitude-titrated ST and $I_{electrode}/E_{brain}$ ratio computed from individual ECT electric field simulation models.

6.4. Discussion and Conclusions

Even though the electric field strength is thought to play a key role in seizure induction in ECT technique, it has not been completely understood. The spatial distributions of the induced electric field strength by various ECT electrode configurations determine which brain regions are directly stimulated for seizure induction. The stimulus current amplitude is a critical aspect of dosage in ECT, as it controls the electric field magnitude and the volume of brain tissues directly activated by the electric stimulation delivered by different ECT electrode montages. The impact of individualizing and reducing current amplitude on the magnitude and distributions of the electric field induced by ECT has not been fully characterized, while ECT with low, individualized current amplitude is still capable of inducing a generalized seizure, potentially minimizing adverse side effects of ECT. This work represents the first quantitative study investigating the electric field characteristics of ECT with low, individualized current amplitude using anatomically-realistic computational NHP head models by combining with neurophysiological measurements acquired during *in vivo* MT and ST titration procedures.

6.4.1. Implications for ECT Dosing

Findings from the present study support the view that ECT induces the electric field distribution in the brain that varies in strength depending upon the ECT stimulus parameters including the position of stimulation electrodes, stimulus pulse amplitude, as well as pulse shape and width [68, 111, 117, 217]. Our results, shown in Figure 6.2, confirm that the spatial distributions of the induced electric field are determined by the shape of the ECT electrodes and their position on the

head, which is consistent with previous studies [68, 111, 217]. The results are further associated with the electrical responses of neuronal membranes. The externally applied electric fields by ECT affect neural activity by depolarizing and hyperpolarizing neuronal membranes [111]. Stimulation with extracellular electric fields leads to the depolarization of a large number of neurons, resulting in modulation of the neural activity and seizure induction [41, 111]. In this respect, the novelty of this study is that the electric field distributions resulting from various ECT paradigms were computed from the anatomically-accurate head models of four different NHP subjects, each with incorporating the individually measured MT and ST data that represent neurophysiological responses, in order to examine the benefits of individualizing and lowering current amplitude in ECT. This was achieved by quantifying and comparing the strength and focality of stimulation, which was estimated by comparing the electric field strength to an estimate of the threshold for neural activation. There has been no modeling study dedicated to investigating the advantages of individualizing and lowering current amplitude as a novel means of improving the safety of seizure therapies. The understanding of the electric field characteristics of various forms of ECT is of particular importance for unraveling the mechanisms of action of ECT and for optimizing its dosage.

The electric field distribution and individual MT and ST were utilized to estimate the strength of stimulation and directly stimulated brain volume above threshold for seizure induction. Using the median electric field strength in the left FDI motor area determined from the most focal stimulation (RUL ECT) as well as the individual MT data, we estimated the neural activation threshold to be 0.45 ± 0.07 V/cm for the 0.2 ms rectangular pulses. Our estimates of electric field threshold for neural activation are consistent with published estimates of threshold electric field strength [254-258], indirectly supporting the validity of our electric field model,

albeit differences in the stimulus parameters (e.g., pulse width, frequency, and number of pulses) and other factors of the ECT procedure (e.g., anesthesia) [111]. As proposed here, calibrating the electric field solution to an empirical estimate of the neural activation threshold could largely compensate for modeling errors from the quasistatic assumption, so that we could reveal what regions of the brain respond to the induced electric fields and are directly activated by various stimulation modalities. We could further determine what the delivered dosage is relative to the neural activation threshold. The electric field stimulation strength exposure of specific brain areas is electrode montage and current amplitude specific, as illustrated in Figures 6.2 and 6.3. The results in Figure 6.2 demonstrate different electric field stimulation characteristics in the brain resulting from the various ECT electrode configurations even when the current strength is at the lowest level required to induce a seizure (ST). Different electric field patterns suggest different loci of seizure induction which may be important for focal brain stimulation. Thus, our study demonstrates the utility of the physiologically-calibrated computational electric field models to analyze various stimulus delivery paradigms, and may inform improved ECT technique with individually-titrated dosage.

It has been reported that conventional ECT delivered with high, fixed current amplitude of 800/900 mA results in excessive direct brain stimulation at markedly suprathreshold levels, potentially contributing to adverse side effects [68, 111, 117, 217]. A substantial number of early experimental studies have been published in order to address that generalized seizures could be induced with lower current amplitudes than traditional high current levels [268, 271, 275-277]. Our results in 6.3(a) show that the largest portion of the brain is directly stimulated by BL ECT even at the lowest current strength that induces a seizure (63 ± 10%). In contrast, the RUL ECT electrode configuration with the lowest current results in the most focal stimulation (25 ± 7%)

and electric field distribution shifted to the right hemisphere, thereby sparing left hemisphere regions from side effects of stimulation (see Figure 6.2). An important observation from our results is that seizure induction with a combination of a relatively focal electrode configuration (RUL) and individually titrated current (ST) produces an electric field distribution with magnitude below the neural activation threshold in, on average, about 75% of the brain. This suggests that the regions of the brain that may be critical to cognitive side effects such as the left temporal lobe may be spared, since the electric field strength there is well below the neural activation threshold, potentially minimizing adverse side effects of ECT. On the other hand, the robust therapeutic effectiveness of BL ECT may stem from the relatively even spread of the electric field and associated large volume of stimulated brain tissues even at ST. The experimental FM configuration with the goal of targeting frontal and superficial brain regions stimulated a slightly smaller brain volume (36 ± 14%) at ST than BF ECT (40 ± 11%), which is also designed to target the prefrontal cortex to reduce memory impairment. However, whether the FM electrode configuration can be used as a means of enhancing antidepressant efficacy and reducing adverse effects is not known yet. Therefore, further clinical studies should evaluate the therapeutic efficacy and adverse effect profile of FM ECT with potentially reduced and individualized current amplitude.

Notably, the stimulated brain volume at amplitude-titrated ST are substantially smaller than the brain volume stimulated with conventional high, fixed current amplitude that may reach as high as 100% [68, 117, 217, 274]. Computational human modeling studies using the spherical and realistic head models demonstrated an excessive stimulation of large portions of the brain at fixed current amplitude of 800 mA, the average of stimulated brain volume is 94%, 84%, and 90% for the BL, BF, and RUL ECT configurations, respectively [68, 117, 217, 274]. Our NHP

modeling results shown in Figure 6.3(b) show the effect of current amplitude on the percentage volume of brain directly activated. Increasing the current amplitude by a factor of 2 (200% ST) stimulated 1.6-2.9 times larger brain volume compared to 100% ST. At the 2×ST current levels, on average, about 98% of the brain volume was exposed to suprathreshold electric field in BL ECT, whereas about 71% of the brain was stimulated by RUL ECT, producing the most focal stimulation even at 2×ST compared to the other electrode configurations. Figure 6.3(b) also demonstrates that reducing current amplitude decreases the activated brain volume. In support of our findings, a recent pilot clinical study reported that seizures were successfully induced in several patients by an investigational electrode configuration for focal electrically administered seizure therapy (FEAST), which is similar to our FM configuration, with current amplitude as low as 400 mA [220]. Another case study with 5 patients showed that generalized seizures were induced by the RUL electrode configuration with 500 mA stimulus current, which is just more than half of conventional level of 800 or 900 mA [271]. As such, the electric field magnitude in the brain induced by ECT with higher currents significantly exceeds the neural activation threshold, potentially higher than necessary for seizure induction. Seizures, in turn, can be generated with lower currents, corresponding to more focal stimulation than those in standard ECT practice. This modeling study suggests that the focality of stimulation can be enhanced by means of reduction of the current amplitude along with the use of focal electrode configurations, thereby achieving more targeted stimulation in ECT. All these observations may provide a rational basis for future clinical studies with various electrode placements and lowered current amplitude. Future work will evaluate the clinical impact of such manipulations.

The fixed current amplitude used in present clinical ECT for all patients results in variable electric field strength and focality among patients due to interindividual differences in head size

and anatomy [111, 116, 226]. As indicated in Table 6.1, there is a substantial individual variability in ST value across subjects. This motivates that ECT stimulus amplitude should be individualized. The objective of current amplitude adjustment would be to obtain comparable intracranial electric field characteristics for various subjects. Figure 6.4 indicates that ECT with individualized ST current strength results in variation in the brain volume stimulated above the neural activation threshold across subjects that is ~1.6–1.9 times smaller than the variation for fixed, average ST current strength. This suggests that current amplitude individualization could be a means of compensating for interindividual variability in anatomy and neurophysiological excitability. Individualizing current amplitude further improves consistency in delivered dose. This observation supports exploring individualization of the ECT stimulus current amplitude in clinical studies. Therefore, ECT with low, individualized current should be evaluated as a means of reducing side effects and outcome variability in clinical studies.

Since the subject-specific model captures the individual anatomical variability, the computational electric field model developed here can be potentially used to estimate the selection of the stimulus current amplitude for dose individualization. Our results in Figure 6.5 indicate that different electric field characteristics in the brain arise due to interindividual variations in head anatomy between four NHP subjects. Based on these individual electric field estimates, we tested if the individual electric field models can be used to predict individual variations in amplitude-titrated ST. As shown in Figure 6.6, we found no significant correlation between estimate of individual amplitude-titrated ST variability from individual electric field models and amplitude-titrated ST for all ECT electrode configurations likely due to a small number of subjects. However, we observed that there is a positive correlation trend (r^2=0.665-0.902), and individual electric field variability is meaningfully related to individual ST variations

between subjects. Our results demonstrate that anatomical variability is a primary factor driving individual differences in ST, and thus dosing requirements for ECT. This suggests that the individual electric field model could be used as a predictor of ST to individualize the stimulus current amplitude in ECT without the need to induce a seizure. Moreover, individual dosage requirement can be predicted by titrating MT without having to induce a seizure, since amplitude-titrated ST and MT are strongly correlated [226]. Both MT titration and individual electric field modeling approaches should be evaluated whether those can serve as safer alternatives to empirical ST titration for dosage individualization.

6.4.2. Limitations and Future Work

As previously discussed by our group [68], any modeling study has several limitations. As the accuracy of the electric field or current density fields in the brain generated by electrical stimulation is limited by accurate representation of head anatomy and dielectric properties of the tissues, errors may arise from a limited number of tissues as well as uncertainty in their electrical conductivity values [68]. However, our electric field modeling approach that couples with empirical data of MT and ST (see Section 2.6) could partially compensate for possible errors in the tissue property modeling [111]. The threshold for neural activation estimated here is independent of the direction of electric field, which is known to affect the neural activation threshold [214, 278-280]. However, if precise electric field threshold data of the other brain regions of interest relative to motor cortex, which also can take into account the electric field direction relative to activated neural population, becomes available in the future, they can be easily incorporated with our model [111]. Future studies will need to integrate the actual neural activation threshold measured in humans into the electric field model, ultimately allowing for

optimizing treatment parameters of seizure therapies and maximizing its antidepressant effects. Finally, our conclusion from a pilot correlation study is limited due to the small sample size. As discussed in Section 4.1, non-significant results are likely due to the small number of subjects, which precludes any generalized conclusions. Nevertheless, there do appear to be a positive correlation trend, motivating further research with larger sample size.

Chapter 7

Electric Field Characteristics of MST with Individualized Current Amplitude

7.1. Introduction

Electroconvulsive therapy (ECT) remains the most effective treatment and rapidly acting antidepressant for severe major depression [79], but its cognitive side effects may be persistent [20]. Various improvements in ECT technique have reduced its side effects without sacrificing efficacy [38, 281, 282]. Modifications in ECT technique that resulted in diminished side effects include pulse shape – shift from sine wave to rectangular brief pulses [26-28] and shift from brief to ultrabrief pulse width [29, 283, 284], electrode placement – introduction of right unilateral (RUL) [31, 32, 282], and individualized dosage – with dosing the number of pulses relative to individual seizure threshold (ST) [35, 38, 285]. Despite these successful modifications in ECT technique, its adverse side effects still arise in many patients. As an alternative form of convulsive therapy, magnetic seizure therapy (MST) has been introduced to achieve more focal

seizure induction for therapeutic efficacy while lowering adverse cognitive side effects associated with ECT. MST involves the induction of a therapeutic seizure in patients under anesthesia using repetitive transcranial magnetic stimulation (rTMS). Recent studies suggest that MST can deliver focal brain stimulation that produces the electric field confined to superficial cerebral cortex and offers a higher side effect profile than conventional ECT [1].

Conventional ECT is applied with a fixed high current amplitude (800 or 900 mA) that results in excessive direct stimulation in the brain than necessary electric field neural activation threshold [86], possibly contributing to adverse side effects of ECT. Recent studies suggest that pulse current amplitude in convulsive therapy be lowered and individualized to improve the risk/benefit ratio of convulsive therapy and to reduce clinical outcome variability [111, 226]. This view is supported by observations that ECT with lower, individualized current amplitude could improve spatial targeting of electric field and compensate for individual anatomical variability [227, 273, 274]. Previously, in multiple nonhuman primate (NHP) models we examined the suprathreshold direct stimulation strength and volume (focality) of various forms of ECT with individualized current amplitude corresponding to amplitude-titrated seizure threshold (ST) measured in the anesthetized NHPs [227, 273]. However, that study estimated the neural activation threshold under the ECT conditions and the electric field characteristics of MST with individualize current amplitude have not been investigated directly.

In this Chapter, the strength and spatial distribution of the electric field generated by a cap (CAP) MST coil configuration are computed in anatomically realistic finite element models of the four NHP subjects. We estimate the electric field neural activation threshold in the motor cortex by coupling the simulated electric field strength with *in vivo* MT data measured with the CAP MST coil. We determine the electric field stimulation strength and focality relative to an

empirical electric field neural activation threshold at individualized current amplitude corresponding to amplitude-titrated ST. We examine the impact of lowering and individualizing current amplitude on the stimulated brain volume. Understanding the induced electric field characteristics and their individual variability could help identify potential causes of the differences in clinical outcome, and could support the improvement of MST dosing paradigms with reduced side effects.

7.2. Materials and Methods

We simulated the electric field induced by MST in realistic finite element NHP head models using the same methods described in Chapters 2 and 6. The modeling methods are described in detail in Chapters 2 and 6 and are summarized here.

7.2.1. MST Head Model Generation

We constructed realistic finite element models of the four healthy male rhesus macaques (*Macaca mulatta*) from T1-weighted magnetic resonance imaging (MRI) and diffusion tensor imaging data sets. We modeled a cap (CAP) coil (MagVenture A/S, Farum, Denmark) configuration using manufacturer's data and inductance measurements. The CAP coil consists of a single-layer, concave circular winding with an inner diameter of 21 mm, outer diameter of 95 mm, and 15 turns (see Figure 7.1). The coil conductors were centered above the vertex of the NHP head model.

7.2.2. Electric Field Computation

All tissue regions were considered electrically isotropic except the white matter. We used tissue electrical conductivity values given in Table 2.1 for the isotropic tissue compartments. To derive the white matter conductivity tensors with variable anisotropy ratios, we deployed the volume normalization technique using the measured diffusion tensors and the isotropic white matter conductivity value given in Table 2.1. The electric field solutions generated by CAP MST at the output of the MagPro MST device were acquired using the electromagnetic time-harmonic solver of ANSYS (ANSYS Inc., Canonsburg, PA) with appropriate boundary conditions in each NHP subject (see Chapter 2 for details).

7.2.3. *In Vivo* Motor and Seizure Threshold Titration

Both the TMS MT and MST ST procedures were carried out using a MagPro MST device with a CAP coil (MagVenture A/S, Farum, Denmark). The coil induced in the head a cosine current pulse with clockwise initial phase direction and a 0.36 ms period. The coil was centered at the vertex of the head, as illustrated in Figure 7.1. Stimulus intensity was reported as percentage of maximum pulse amplitude (% MA). Maximum pulse amplitude corresponds to 1,800 V peak coil voltage. We determined the MT corresponding to the amplitude of a single TMS pulse required to elicit a motor response in sedated NHPs [226]. The NHP subjects were sedated with ketamine (5–10 mg/kg i.m.) and xylazine (0.35–0.7 mg/kg i.m.) [44]. In each subject, the individual MT was determined as the lowest stimulus pulse amplitude needed to achieve a 50 μV peak-to-peak motor evoked potential in the first dorsal interosseous (FDI) muscle for at least five

out of ten trials [244]. ST was titrated by increasing the stimulus pulse amplitude in percentage of maximum pulse amplitude in MST while holding all the other stimulus parameters were fixed (50 pulses/s, 10 s train duration). We confirmed seizures by observing the motor seizure manifestations in the left arm and the EEG as a secondary criterion. The MT and ST titration was repeated three times on three separate days in each subject.

7.2.4. Stimulation Strength and Focality Analysis

An individual neural activation threshold was derived from the median electric field strength in the FDI representation of the motor cortex at current amplitude corresponding to the individual MT given in Table 7.1. This threshold electric field strength was compared to an estimate from the literature, $\underline{E}_{th}$ = 1.18 V/cm for CAP MST [117]. We determined maps of electric field stimulation strength relative to individual electric field threshold by dividing the electric field magnitude distribution in the brain by the threshold, E/E_{th} [5, 6]. We quantified the focality of stimulation by the percentage of the brain volume that is exposed to electric field strong enough to produce suprathreshold depolarization, i.e., the volume where $E/E_{th} \geq 1$ [6].

7.3. Results

7.3.1. Neural Activation Threshold

We estimated the electric field threshold for neural activation by coupling the simulated electric field strength in the motor cortex with the measured MT. Table 7.1 gives the empirical average

MT for left and right hands and average ST values for the CAP MST coil configuration, which are also plotted in Figures 7.1(a)–(c), respectively. All values in Table 7.1 are the averages of three measurements. CAP MST MTs in the left hand were used to derive the estimates of electric field threshold for neural activation. The average MT in the left hand across the four NHP subjects is 21%, with a range of 16–24 mA (1.5-fold variation) and coefficient of variation of 0.16. The repeated measures analysis of variance (ANOVA) analysis of the combined dataset from all CAP MST titration sessions resulted in a significant difference on MTs (left hand: $F = 11.51$, $df = 3$, $p = 0.0028$; right hand: $F = 90.52$, $df = 3$, $p = 1.63e\text{-}6$) and STs ($F = 11.45$, $df = 3$, $p = 0.0029$) between the four NHP subjects. Figure 7.1(d) shows the corresponding estimates of the electric field threshold for neural activation for each subject, which are also summarized in Table 7.2. The average electric field threshold across the four NHP subjects is 0.77 V/cm (standard deviation = 0.06, coefficient of variation = 0.07). A comparison of the electric field threshold values in Figure 7.1 and Table 7.2 shows that subject CH has the highest electric field threshold (0.85 V/cm), while subject MA has the lowest electric field threshold (0.72 V/cm). We found no significant effect of NHP subject on the electric field thresholds ($F = 2.51$. $df = 3$, $p = 0.1328$).

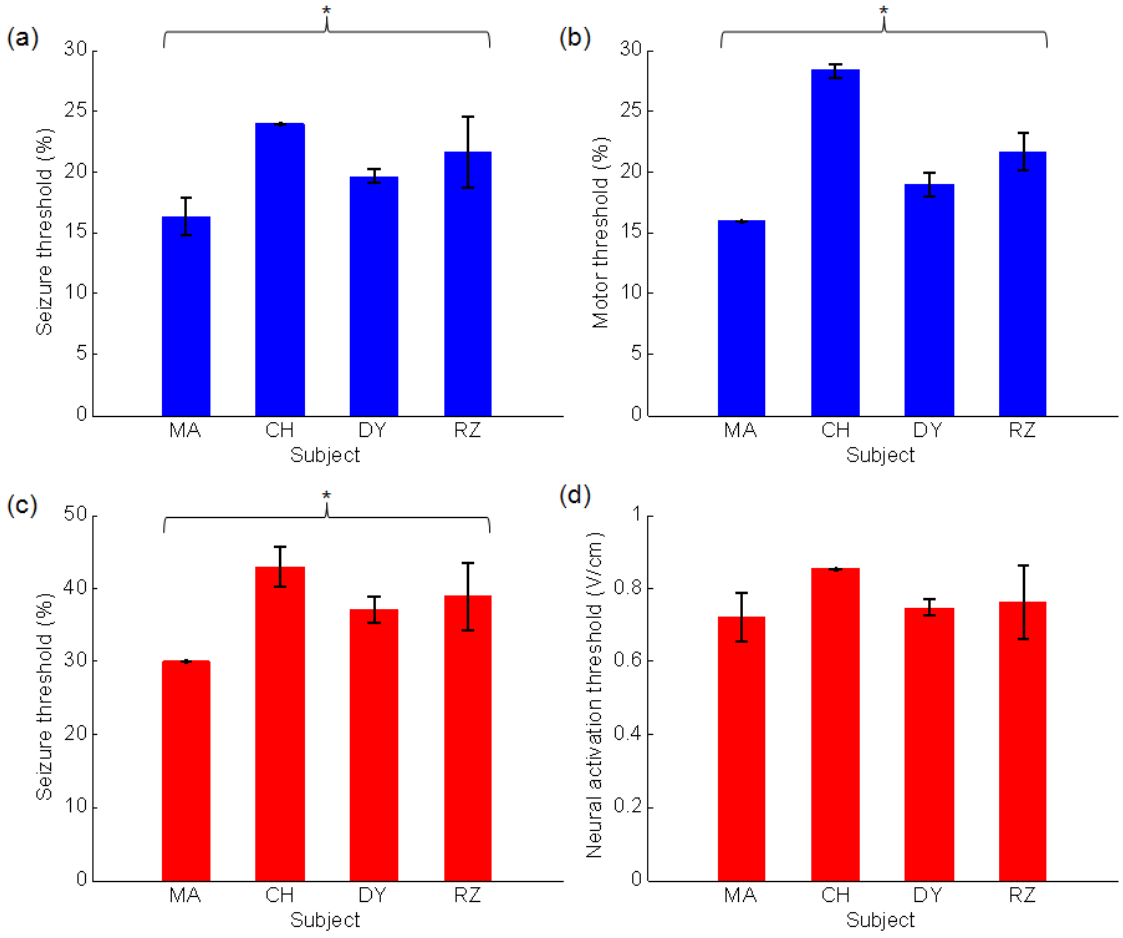

Figure 7.1. Individual amplitude-titrated CAP MST motor threshold (MT) for (a) left and (b) right hands as well as (c) seizure threshold (ST) for the four NHP subjects. (d) Corresponding estimated electric field neural activation threshold in the motor cortex representation of FDI. Bar show mean values and error bars show standard deviations. An asterisk represents significant difference between the NHP subjects at a threshold of $p < 0.05$ in an ANOVA.

Table 7.1. Individually measured average motor threshold (%) for left (L) and right (R) hands and average seizure threshold (%) for the CAP MST coil configuration in the four NHP subjects. SD: standard deviation

Subject	Motor Threshold (%)		Seizure Threshold (%)
	L Hand	R Hand	
MA	16	16	30
CH	24	28	43
DY	20	19	37
RZ	22	22	39
Mean (SD)	21	21	37

Table 7.2. Individual neural activation threshold (V/cm) for the four NHP subjects. SD: standard deviation

	MA	CH	DY	RZ	Mean (SD)
E_{th}	0.72	0.85	0.75	0.76	0.77 (0.06)

7.3.2. Electric Field Distribution Relative to Neural Activation Threshold

Figure 7.2 shows the simulated CAP MST coil configuration for the four NHP subjects (subjects MA, CH, DY, and RZ), and corresponding cortical surface maps as well as coronal cross-sectional maps of the electric field distributions relative to the neural activation threshold (E_{th}) at current strengths corresponding to amplitude-titrated STs (see Table 7.1).

Figure 7.3 shows descriptive statistics (1st, 25th, 50th (median), 75th, and 99th percentiles) of the electric field magnitude relative to the neural activation threshold at individual ST for the four NHP subjects. At individual ST, subject DY has the highest median electric field strength relative to threshold (0.62), whereas subject CH has the lowest strength value (0.38), resulting in 1.6-fold variation in the whole brain across the four NHP subjects. The median MST induced electric field strength ranges from 0.4 to 0.6 times threshold.

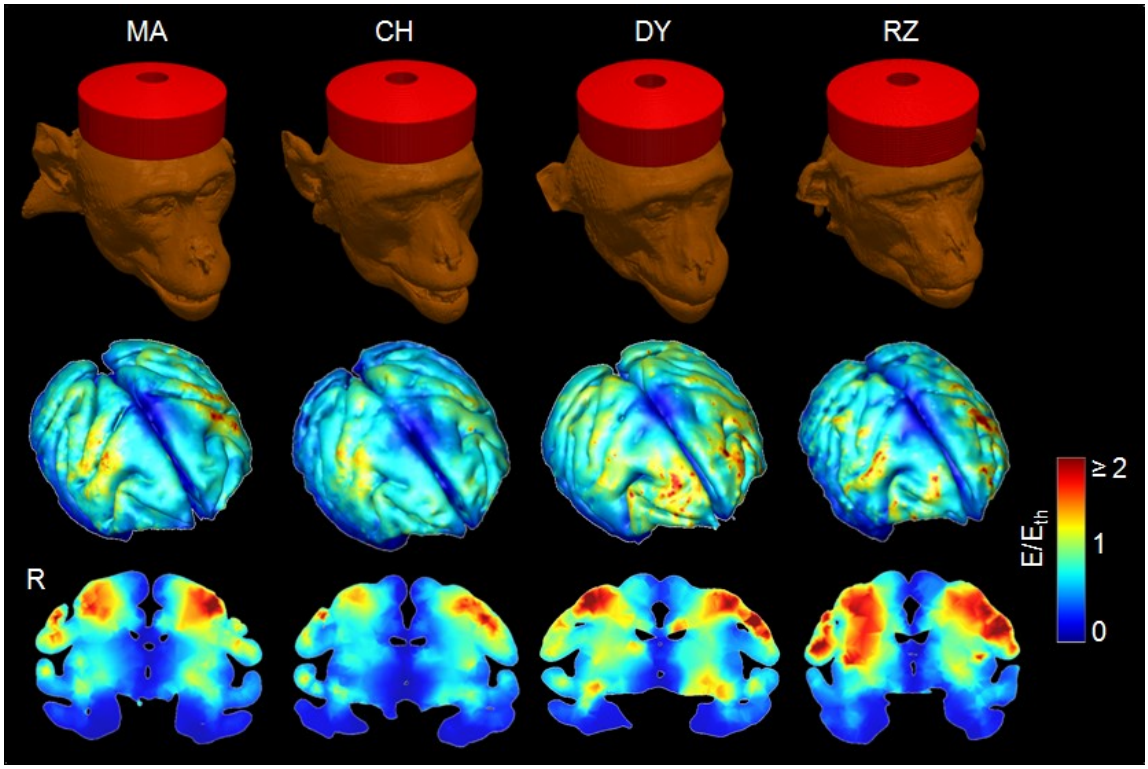

Figure 7.2. Simulation models of CAP MST for the four NHP subjects (top row, subjects MA, CH, DY, and RZ). Electric field stimulation strength relative to neural activation threshold (E_{th}) at current amplitude corresponding to amplitude-titrated seizure threshold (ST) on the cortical surface (middle row) and in a representative coronal slice (bottom row). The E/E_{th} color map is clamped at an upper limit of 2 for good visibility of the distribution of electric field stimulation strength. R: right.

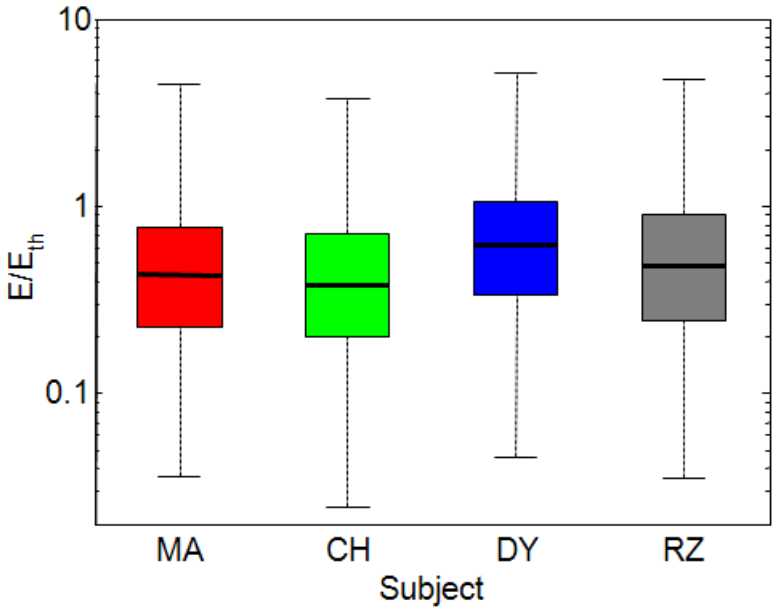

Figure 7.3. Descriptive statistics of electric field magnitude relative to neural activation threshold at individual ST for the four NHP subjects. The electric field stimulation strength (y-axis) is known on a logarithmic scale to normalize the skewed electric field distribution. Boxes indicate the interquartile range (25th to 75th percentile) with the median marked by a thick horizontal line, and whiskers delimit the 1st and 99th percentiles of the electric field distribution.

7.3.3. Effect of Current Amplitude

Figure 7.4 shows the effect of current amplitude on the percentage of the brain volume with electric field above the neural activation threshold for the four NHP subjects. At individual STs, the results in Figure 7.4(a) show that subject RZ has the largest stimulated brain volume (27%), whereas subject CH has the lowest activated brain volume (18%). The average of directly activated brain volume is 23% (standard deviation = 4, coefficient of variation = 0.17) across the four NHP subjects. The results in Figure 7.4(b) show that the stimulated brain volume above threshold increases with higher current amplitude.

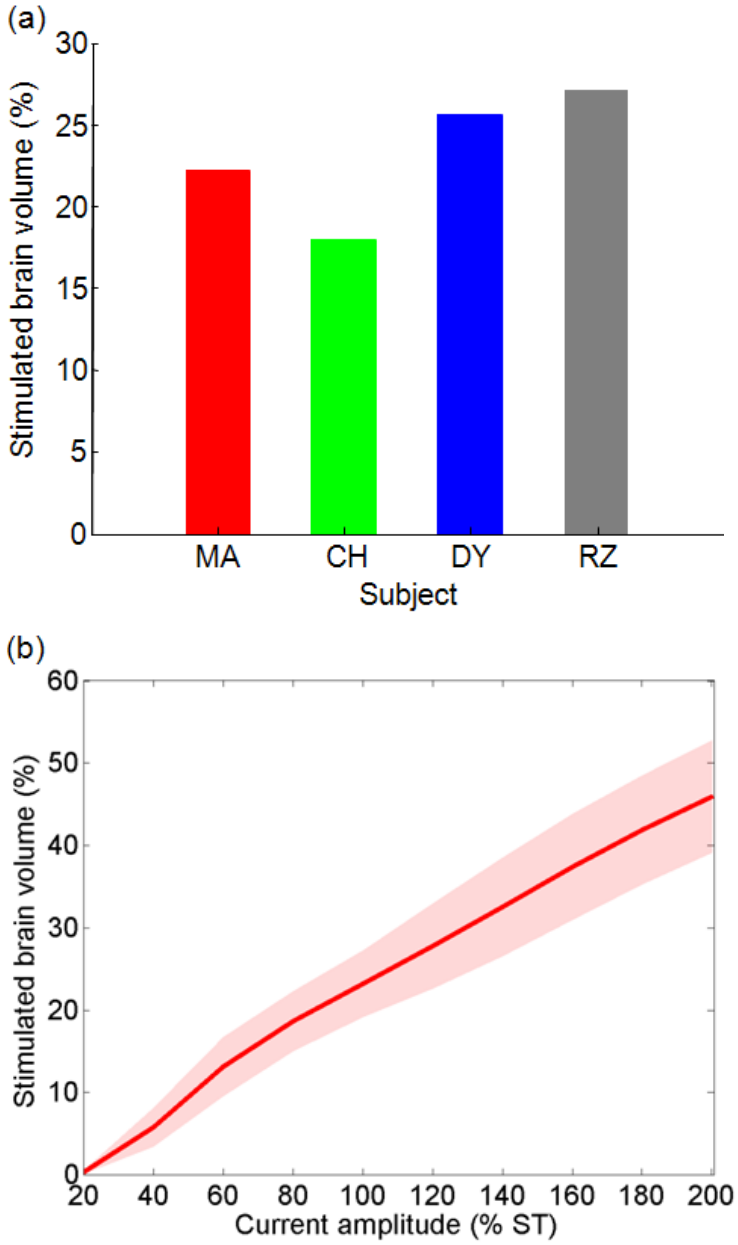

Figure 7.4. Effect of current amplitude on the percentage directly stimulated brain volume above the neural activation threshold ($E \geq E_{th}$) (a) at individual STs (100% ST) and (b) as a function of current amplitude relative to the neural activation threshold for CAP MST. Red color band represents the average (solid line) and standard deviation (shade) of the percentage stimulated brain volume across the four subjects with a range of current amplitudes.

7.3.4. Effect of Current Amplitude Individualization

Figure 7.5 compares the coefficient of variation of the stimulated brain volume above the neural activation threshold among the four NHP subjects between MST with individualized versus group-average (fixed) ST current amplitude. Group-average ST current strength (37%) was used as the fixed current amplitude (see Table 7.1). The results in Figure 7.5 show that individualized current amplitude results in less variability of the stimulation brain volume across the four subjects (17%) compared to MST with the fixed, average ST current amplitude (23%).

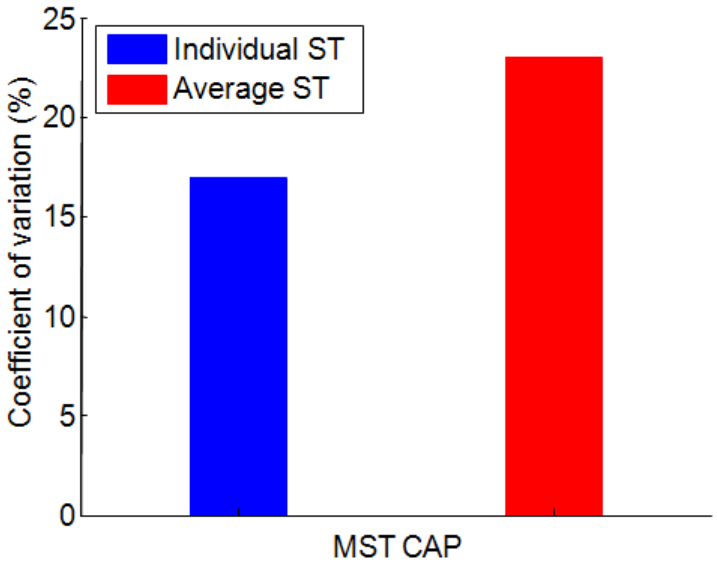

Figure 7.5. Comparison of coefficient of variation of the stimulated brain volume above the neural activation threshold among the four NHP subjects between MST with individual versus group-average (fixed) ST current amplitude for the CAP MST coil configuration.

7.4. Discussion and Conclusions

Understanding the electric field characteristics is of particular importance to unravel the mechanisms of therapeutic seizure induction in MST techniques, but it has not been completely understood. The impact of lowering and individualizing current amplitude on the magnitude and distribution of the electric field induced by MST has not been fully investigated. Therefore, this work represents the first quantitative study investigating the electric field characteristics of MST with individualized current amplitude using high-resolution anatomically accurate finite element models of the four NHP subjects and neurophysiological measurements acquired during *in vivo* MT and ST titration procedures. The results in Figure 7.2 demonstrate the electric field stimulation patterns in the brain at the lowest current strength required to induce a seizure (ST). These results indicate that CAP MST provides less intense and superficial stimulation, supporting that MST may reduce the cognitive side effects of convulsive therapy. This also suggests that MST can be used as a more focal stimulation form of seizure induction.

We utilized the electric field distribution and individual MT and ST data to estimate the strength of stimulation and directly activated brain volume above threshold for seizure induction. Using the median electric field strength in the FDI motor area and the individual MT data, we estimated the neural activation threshold to be 0.77 ± 0.06 V/cm, with a range of 0.72–0.85 V/cm. Our estimates of electric field threshold for neural activation are consistent with published estimates of threshold electric field strength (0.3–1.3 V/cm) [254-257], indirectly supporting the validity of our MST electric field model. Furthermore, we found that our estimated average neural activation threshold (0.77 V/cm) is lower than an estimate (1.18 V/cm) from the literature [117]. This discrepancy may stem from the use of the average human TMS MT data by the figure-8 coil from the literature in that study.

Our results in Figure 7.4 demonstrate that the directly stimulated brain volume above the neural activation threshold is controlled by the current amplitude. The stimulated brain volume at amplitude-titrated ST is substantially lower than the brain volume activated with conventional fixed, high current amplitude that may reach as high as 100% [68, 117, 217, 274]. For example, at the 2×ST current level, our results show that about 46% of the brain volume was exposed to suprathreshold electric field. Increasing the current strength by a factor of 2 (200% ST) stimulated 2 times larger brain volume compared to 100% ST. Another important observation is that seizure induction with a combination of a CAP MST coil configuration and individualized current amplitude (ST) results in an electric field distribution with magnitude below the neural activation threshold in, on average, 77% of the brain. This suggests that direct stimulation of medial-temporal brain regions (e.g., hippocampus) that may be critical to cognitive side effects may be spared, since the electric field strength there is well below the neural activation threshold. This view is also supported by our findings in Figure 7.3 that the MST-induced median electric field strength relative to threshold is well below the neural activation threshold. MST with low, individualized current amplitude provides the electric field in the brain that does not exceed the threshold for neural activation, possibly reducing adverse side effects of convulsive therapy.

The results in Figure 7.5 indicate that MST with individualized current amplitude results in variation in the brain volume stimulated above neural activation threshold across the four NHP subjects that is ~1.3 times smaller than the variation for fixed, average current strength. This suggests that current amplitude individualization could be used as a means of compensating for interindividual variability in anatomy and neurophysiological excitability. Our findings suggest

that MST with low, individualized current amplitude should be explored as a means of reducing side effects and outcome variability in clinical studies.

Taken together, these observations support exploring MST paradigms with low, individualized current amplitude as a potential means of reducing side effects. This work further demonstrates the utility of computational electric field models to examine the electric field stimulation strength and focality to provide insight into the mechanisms of therapeutic seizure induction, and could provide rational basis for future clinical investigation of MST with individualized current amplitude with improved risk/benefit ratio.

Chapter 8

Contributions and Future Research Suggestions

8.1. Contributions

The objective of this dissertation was to develop a novel framework for the rational dosing of electric and magnetic seizure therapy to improve existing approaches for seizure therapies and to develop novel, safer and effective treatments for mental illness and inform the development of device-based therapies that better balance adverse effects and therapeutic outcomes. To this end, this work developed a new platform that couples computational modeling with *in vivo* empirical validation for the refinement of ECT/MST techniques. The present work supports the development of novel forms of seizure therapy with an improved side effect profile, thereby benefiting patients with severe psychiatric disorders.

Original contributions of this dissertation are that (1) it is the first application of individualized realistic 3-D head models to ECT/MST; (2) it couples computational modeling with *in vivo* empirically optimized pulse amplitude and train characteristics; (3) it involves cutting-edge approaches to enhancing the focality of electric and magnetic seizure therapy

through novel electrode/coil and current amplitude configurations (e.g., FEAST and FM ECT, and MST); (4) it entails interdisciplinary work between biomedical engineering and psychiatry, which has been lacking in the field of seizure therapies; (5) it may lead to entirely new and clinically feasible means of ECT/MST dosing paradigms thus potentially improving their risk/benefit ratio; (6) computational modeling tools develop here have a broad impact beyond seizure therapies, because they can be applied to they can be applied to aid field shaping for subconvulsive applications of the recently FDA-approved transcranial magnetic stimulation (TMS) and transcranial direct current stimulation (tDCS) as well. The key findings of the dissertation are summarized below:

In Chapter 2, we developed anatomically realistic finite element models using high-resolution structural MRI and DTI data of human and NHPs for transcranial electric and magnetic stimulation. The NHP models of transcranial brain stimulation were constructed alongside the human model since NHPs are used in preclinical studies on the mechanisms of seizure therapy.

In Chapter 3, we presented the first computational study investigating the electric field (E-field) strength generated by various ECT electrode configurations in specific brain regions of interest (ROIs) that have putative roles in the therapeutic action and/or adverse side effects of ECT. This study also characterized the impact of the white matter conductivity anisotropy on the electric field distribution. A finite element head model incorporating tissue heterogeneity and WM anisotropic conductivity was constructed based on structural MRI and DTI data. We computed the spatial electric field distributions generated by three standard ECT electrode placements including BL, BF, and RUL and an investigational electrode configuration for focal electrically administered seizure therapy (FEAST). The key results are that (1) the median

electric field strength over the whole brain is 3.9, 1.5, 2.3, and 2.6 V/cm for the BL, BF, RUL, and FEAST electrode configurations, respectively, which coupled with the broad spread of the BL electric field suggests a biophysical basis for observations of superior efficacy of BL ECT compared to BF and RUL ECT; (2) in the hippocampi, BL ECT produces a median electric field of 4.8 V/cm that is 1.5–2.8 times stronger than that for the other electrode configurations, consistent with the more pronounced amnestic effects of BL ECT; and (3) neglecting the white matter conductivity anisotropy results in electric field strength error up to 18% overall and up to 39% in specific ROIs, motivating the inclusion of the white matter conductivity anisotropy in accurate head models. This computational study demonstrates how the realistic finite element head model incorporating tissue conductivity anisotropy provides quantitative insight into the biophysics of ECT, which may shed light on the differential clinical outcomes seen with various forms of ECT, and may guide the development of novel stimulation paradigms with improved risk/benefit ratio.

In Chapter 4, we examined the characteristics of the electric field induced in the brain by ECT and MST. The electric field induced by five ECT electrode configurations (bilateral, bifrontal, right unilateral, focal electrically administered seizure therapy, and frontomedial) as well as an MST coil configuration (circular) was computed in an anatomically realistic finite element model of the human head. We computed the maps of the electric field strength relative to an estimated neural activation threshold, and used them to evaluate the stimulation strength and focality of the various ECT and MST paradigms. The results show that the median ECT stimulation strength in the brain is 7–29 times higher than that for MST, and that the stimulated brain volume is substantially higher with ECT (47–100%) than with MST (4%). This study provides insight into the observed reduction of cognitive side effects in MST compared to ECT,

and supports arguments for lowering ECT current amplitude as a means of curbing its side effects.

In Chapter 5, we derived an estimate of the electric field neural activation threshold and tested whether individual differences in TES MT can be predicted by individual anatomical variability as captured by structural MRI data and individualized electric field simulation models. The electric field distribution induced by a right unilateral (RUL) TES/ECT electrode configuration was computed in subject-specific finite element head models of four nonhuman primates (NHPs) for whom individual MT was measured. By combining the measured MTs with the computed electric field maps, the neural activation threshold was estimated to be 0.45 ± 0.07 V/cm for 0.2 ms stimulus pulse width. The individual MT was correlated with the electrode-to-cortex distance under the superior electrode (r^2=0.96, p=0.022) and at vertex (r^2=0.96, p=0.022), as well as with the simulated electrode-current/induced-E-field ratio (r^2=0.95, p=0.026), thus indicating that both individual anatomical variability and individualized electric field models could predict the individual current requirements for transcranial brain stimulation. These findings could be used with realistic human head models and in clinical studies to explore novel ECT dosing paradigms, and as a new noninvasive means to determine individual dosage requirement with ECT.

In Chapter 6, we investigated the characteristics of the electric field induced in the brain by ECT with individualized current amplitude in nonhuman primate (NHP) models. The electric field spatial distributions of three conventional ECT electrode placements including bilateral (BL), bifrontal (BF), and right unilateral (RUL) and an investigational frontomedial (FM) configuration were computed in anatomically realistic finite element models of four NHP heads. We generated maps of the electric field strength relative to an empirical neural activation

threshold, and determined the stimulation strength and focality of the various ECT electrode configurations with individualized current amplitude corresponding to amplitude-titrated seizure threshold (ST) assessed in the anesthetized NHPs, as well as fixed current amplitude corresponding to average ST. The key results are that (1) at individual ST, the average of percentage brain volume stimulated above neural activation threshold is 63%, 40%, 25%, and 36% for the BL, BF, RUL, and FM electrode configurations, suggesting that the focality of stimulation can be enhanced by reduction of the current amplitude along with the use of the focal electrode configuration; (2) ECT with individualized current amplitude results in less variation (16–39%) in stimulated brain volume above threshold compared to fixed, average current amplitude (29–64%), suggesting that current amplitude individualization results in more focal and uniform electric field exposure across different subjects, and can be used as a means of compensating for interindividual variability in anatomy and neurophysiological excitability. Understanding the stimulation strength and focality of various forms of ECT could provide insight into the mechanisms of therapeutic seizure induction, and could provide a rational basis for the clinical investigation of ECT with lowered and individualized current amplitude as an intervention with potentially improved risk/benefit ratio.

In Chapter 7, we investigated the characteristics of the electric field induced in the brain by MST with individualized current amplitude in anatomically realistic nonhuman primate (NHP) head models. The electric field distributions induced in the brain by a cap (CAP) MST were simulated in realistic finite element models of the four NHP subjects. We created maps of the electric field strength relative to an empirical neural activation threshold, and determined the stimulation strength and focality of the CAP MST coil configuration with individualized current amplitude corresponding to amplitude-titrated seizure threshold (ST) assessed in the anesthetized

NHPs, as well as a fixed current amplitude corresponding to group-average ST. The key results are that (1) at individual ST, the average of percentage brain volume stimulated above neural activation threshold is 23%, suggesting that the focality of stimulation can be improved by lowering the current amplitude; (2) MST with individualized current amplitude results in less variation (17%) in stimulated brain volume above threshold compared to fixed, average current amplitude (23%), suggesting that current amplitude individualization results in more focal and uniform electric field exposure across different subjects, and can be used as a means of compensating for interindividual variability in head anatomy and neurophysiological excitability. Understanding the induced electric field characteristics and their individual variability could help identify potential causes of the variations in clinical outcome, and could support the development of MST dosing paradigms with reduced side effects.

8.2. Suggestions for Future Research

Some ideas of how the work in this dissertation can be extended were already discussed in the text. Here we attempt to summarize research directions for future work.

First, while computational models offer accurate insight into detailed electric field/current density field patterns, there are several sources of uncertainty that confound the conclusions of modeling studies. Uncertainty about the electrical properties of the various tissues in the model can contribute inaccuracies of the simulated electric field. The accuracy of electric field in the brain is also limited by the precision and accuracy of tissue segmentation. Although there has been no comprehensive effort for direct validation of the computational modes with experimental data, several studies have attempted to validate the accuracy of the computational

forward models by comparing to neurophysiological measurements [232, 233]. However, there remains a dearth of experimental data validating direct model predictions of induced electric field in the brain. Techniques to experimentally validate the simulated electric field/current density field induced in the brain should be explored. For example, current density imaging (CDI), which is a MRI technique used to quantitatively measure the magnitude and direction of current density vectors [286, 287], could be employed for experimental assessments.

Second, imaging of brain activity during transcranial electric and magnetic stimulation is of particular importance to facilitate the detection of psychiatric disorders and to advance our understanding of the mechanisms of therapeutic effects of psychiatric interventions. The electric field distribution is a key aspect of dosage for both ECT and MST and knowledge of this distribution may help to explain differences in efficacy and side effects seen with existing paradigms and may inform novel methods to improve spatial brain stimulation. However, the electric field alone is not sufficient to evaluate biological, functional, and behavioral effects. The combination of transcranial brain stimulation (e.g., ECT/MST) with other brain imaging modalities (e.g., diffusion tensor and functional MRI, electroencephalography or magnetoencephalography, single photon emission computed tomography) can provide insight into the effect of the induced electric field in the brain and may help to document large-scale stimulation-induced reorganization of structural and functional networks at rest or during task-related activity [288]. Correlating the computational field models with imaging and electrophysiological measurements of brain activity should be explored.

Third, future studies can also explore the incorporation of direction-sensitive neural activation threshold with our electric field models. The electric field threshold for neural activation discussed in Chapters 6 and 8 is independent of the electric field direction. The electric

field direction relative to the stimulated neural population may affect the neural activation threshold [214]. As such, the direction of the induced electric field is an important determinant of the effective stimulation strength and focality [223]. If the electric field direction data becomes available in future studies, it can be incorporated with our electric field models. The computational model with white matter anisotropic conductivity developed in Chapter 2 can also provide more accurate electric field directional information compared to the model with fully isotropic conductivity. The electric field characteristics of ECT/MST paradigms by linking with the direction-sensitive neural activation threshold should be explored.

Bibliography

[1] S. H. Lisanby, B. Luber, T. E. Schlaepfer, and H. A. Sackeim, "Safety and feasibility of magnetic seizure therapy (MST) in major depression: randomized within-subject comparison with electroconvulsive therapy," *Neuropsychopharmacology,* vol. 28, pp. 1852-1865, 2003.

[2] R. C. Kessler, K. A. McGonagle, S. Zhao, C. B. Nelson, M. Hughes, S. Eshleman, H. U. Wittchen, and K. S. Kendler, "Lifetime and 12-month prevalence of DSM-III-R psychiatric disorders in the United States. Results from the National Comorbidity Survey," *Arch Gen Psychiatry,* vol. 51, pp. 8-19, Jan 1994.

[3] R. C. Kessler, P. Berglund, O. Demler, R. Jin, D. Koretz, K. R. Merikangas, A. J. Rush, E. E. Walters, P. S. Wang, and R. National Comorbidity Survey, "The epidemiology of major depressive disorder: results from the National Comorbidity Survey Replication (NCS-R).[see comment]," *JAMA,* vol. 289, pp. 3095-105, 2003.

[4] D. L. Evans and D. S. Charney, "Mood disorders and medical illness: a major public health problem," *Biol Psychiatry,* vol. 54, pp. 177-80, 2003.

[5] C. M. Michaud, C. J. Murray, and B. R. Bloom, "Burden of disease--implications for future research," *JAMA,* vol. 285, pp. 535-9, Feb 7 2001.

[6] A. J. Rush, M. H. Trivedi, S. R. Wisniewski, A. A. Nierenberg, J. W. Stewart, D. Warden, G. Niederehe, M. E. Thase, P. W. Lavori, B. D. Lebowitz, P. J. McGrath, J. F. Rosenbaum, H. A. Sackeim, D. J. Kupfer, J. Luther, and M. Fava, "Acute and longer-term outcomes in depressed outpatients requiring one or several treatment steps: a STAR*D report," *American Journal of Psychiatry,* vol. 163, pp. 1905-17, 2006.

[7] U. E. R. Group, "Efficacy and safety of electroconvulsive therapy in depressive disorders: a systematic review and meta-analysis.[see comment]," *Lancet,* vol. 361, pp. 799-808, 2003.

[8] M. M. Husain, A. J. Rush, M. Fink, R. Knapp, G. Petrides, T. Rummans, M. M. Biggs, K. O'Connor, K. Rasmussen, M. Litle, W. Zhao, H. J. Bernstein, G. Smith, M. Mueller, S. M. McClintock, S. H. Bailine, and C. H. Kellner, "Speed of response and remission in major depressive disorder with acute electroconvulsive therapy (ECT): a Consortium for Research in ECT (CORE) report," *Journal of Clinical Psychiatry,* vol. 65, pp. 485-91, 2004.

[9] J. Prudic and H. Sackeim, "Electroconvulsive therapy and suicide risk," *J Clin Psychiatry,* vol. 60 Suppl 2, pp. 104-10, 1999.

[10] R. Abrams, *Electroconvulsive Therapy*, 4th ed.: Oxford University Press, 200.

[11] T. B. Karasu, A. Gellenberg, A. Merriam, and P. Wang, *Practice Guideline for the Treatment of Patients with Major Depressive Disorder*, 2nd ed.: American Psychiatric Association, 2000.

[12] M. Fava, A. J. Rush, M. H. Trivedi, A. A. Nierenberg, M. E. Thase, H. A. Sackeim, F. M. Quitkin, S. Wisniewski, P. W. Lavori, J. F. Rosenbaum, and D. J. Kupfer, "Background and rationale for the sequenced treatment alternatives to relieve depression (STAR*D) study," *Psychiatric Clinics of North America,* vol. 26, pp. 457-94, 2003.

[13] D. C. Steffens, D. R. McQuoid, and K. R. Krishnan, "The Duke Somatic Treatment Algorithm for Geriatric Depression (STAGED) approach," *Psychopharmacology Bulletin,* vol. 36, pp. 58-68, 2002.

[14] H. Grunze, S. Kasper, G. Goodwin, C. Bowden, D. Baldwin, R. Licht, E. Vieta, H. J. Moller, and D. World Federation of Societies of Biological Psychiatry Task Force on Treatment Guidelines for Bipolar, "World Federation of Societies of Biological Psychiatry (WFSBP) guidelines for biological treatment of bipolar disorders. Part I: Treatment of bipolar depression," *World Journal of Biological Psychiatry,* vol. 3, pp. 115-24, 2002.

[15] Lisanby SH, Maddox JH, Prudic J, Devanand DP, and Sackeim HA, "The effects of electroconvulsive therapy on memory of autobiographical and public events," *Arch Gen Psychiatry,* vol. 57, pp. 581-590, 2000.

[16] R. D. Weiner, "Retrograde amnesia with electroconvulsive therapy: characteristics and implications.[comment]," *Archives of General Psychiatry,* vol. 57, pp. 591-2, 2000.

[17] C. Sobin, H. A. Sackeim, J. Prudic, D. P. Devanand, B. J. Moody, and M. C. McElhiney, "Predictors of retrograde amnesia following ECT," *American Journal of Psychiatry,* vol. 152, pp. 995-1001, 1995.

[18] L. R. Squire, P. C. Slater, and P. L. Miller, "Retrograde amnesia and bilateral electroconvulsive therapy. Long-term follow-up," *Archives of General Psychiatry,* vol. 38, pp. 89-95, 1981.

[19] A. B. Donahue, "Electroconvulsive therapy and memory loss: a personal journey.[see comment]," *Journal of ECT,* vol. 16, pp. 133-43, 2000.

[20] H. A. Sackeim, J. Prudic, R. Fuller, J. Keilp, P. W. Lavori, and M. Olfson, "The cognitive effects of electroconvulsive therapy in community settings," *Neuropsychopharmacology,* vol. 32, pp. 244-254, Jan 2007.

[21] G. A. Nuttall, M. R. Bowersox, S. B. Douglass, J. McDonald, L. J. Rasmussen, P. A. Decker, W. C. Oliver, Jr., and K. G. Rasmussen, "Morbidity and mortality in the use of electroconvulsive therapy," *Journal of ECT,* vol. 20, pp. 237-41, 2004.

[22] H. A. Sackeim, J. Prudic, D. P. Devanand, M. S. Nobler, S. H. Lisanby, S. Peyser, L. Fitzsimons, B. J. Moody, and J. Clark, "A prospective, randomized, double-blind comparison of bilateral and right unilateral electroconvulsive therapy at different stimulus intensities.[see comment]," *Archives of General Psychiatry,* vol. 57, pp. 425-34, 2000.

[23] Sackeim HA, Prudic J, Devanand DP, Kiersky JE, Fitzsimons L, Moody BJ, McElhiney MC, Coleman EA, and Settembrino JM, "Effects of stimulus intensity and electrode placement on the efficacy and cognitive effects of electroconvulsive therapy," *The New England Journal of Medicine,* vol. 328, pp. 839-846, 1993.

[24] H. A. Sackeim, S. Portnoy, P. Neeley, B. L. Steif, P. Decina, and S. Malitz, "Cognitive consequences of low-dosage electroconvulsive therapy," *Annals of the New York Academy of Sciences,* vol. 462, pp. 326-40, 1986.

[25] S. H. Lisanby, "Electroconvulsive therapy for depression," *N Engl J Med,* vol. 357, pp. 1939-1945, 2007.

[26] W. T. Liberson, "Brief stimulus therapy - physiological and clinical observations," *Am J Psychiatry,* vol. 105, pp. 28-39, 1948.

[27] R. D. Weiner, "ECT and seizure threshold: effects of stimulus wave form and electrode placement," *Biol Psychiatry,* vol. 15, pp. 225-41, Apr 1980.

[28] L. R. Squire and J. A. Zouzounis, "ECT and memory: brief pulse versus sine wave," *Am J Psychiatry,* vol. 143, pp. 596-601, May 1986.

[29] B. Cronholm and J. O. Ottosson, "Ultrabrief stimulus technique in electroconvulsive therapy. I. Influence on retrograde amnesia of treatments with the Elther ES electroschock apparatus, Siemens Konvulsator III and of lidocaine-modified treatment," *J Nerv Ment Dis,* vol. 137, pp. 117-23, Aug 1963.

[30] Cronholm B and Ottoson JO, "Ultrabrief stimulus technique in electroconvulsive therapy: II. Comparative studies of therapeutic effects and memory disturbance in treatment of endogenous depression with the Either ES electroshock apparatus and Siemens Konvulsator IIIin EST by unilateral stimulation of the non-dominant hemisphere.," *Journal of Nervous and Mental Disorders,* vol. 137, pp. 268-276, 1963.

[31] L. R. Squire, "ECT and memory loss," *Am J Psychiatry,* vol. 134, pp. 997-1001, 1977.

[32] S. R. Squire and P. C. Slater, "Bilateral and unilateral ECT: effects on verbal and nonverbal memory," *Am J Psychiatry,* vol. 135, pp. 1316-20, 1978.

[33] R. Abrams and M. A. Taylor, "Anterior bifrontal ECT: a clinical trial," *Br J Psychiatry,* vol. 122, pp. 587-90, May 1973.

[34] G. Petrides and M. Fink, "The "half-age" stimulation strategy for ECT dosing," *Convuls Ther,* vol. 12, pp. 138-46, Sep 1996.

[35] H. A. Sackeim, P. Decina, S. Portnoy, P. Neeley, and S. Malitz, "Studies of dosage, seizure threshold, and seizure duration in ECT," *Biol Psychiatry,* vol. 22, pp. 249-68, Mar 1987.

[36] H. A. Sackeim, J. Prudic, M. S. Nobler, L. Fitzsimons, S. H. Lisanby, N. Payne, R. M. Berman, E. L. Brakerneier, T. Perera, and D. P. Devanand, "Effects of pulse width and electrode placement on the efficacy and cognitive effects of electroconvulsive therapy," *Brain Stimulation,* vol. 1, pp. 71-83, Apr 2008.

[37] Sackeim HA, Prudic J, Devanand DP, Nobler MS, Lisanby SH, Peyser S, Fitzsimons L, Moody BJ, and Clark J, "A prospective, randomized, double-blind comparison of bilateral and right unilateral electroconvulsive therapy at different stimulus intensities," *Arch Gen Psychiatry,* vol. 57, pp. 425-434, 2000.

[38] H. A. Sackeim, J. Prudic, D. P. Devanand, M. S. Nobler, S. H. Lisanby, S. Peyser, L. Fitzsimons, B. J. Moody, and J. Clark, "A prospective, randomized, double-blind comparison of bilateral and right unilateral electroconvulsive therapy at different stimulus intensities," *Arch Gen Psychiatry,* vol. 57, pp. 425-434, 2000.

[39] Sackeim HA, "Convulsant and anticonvulsant properties of electroconvulsive therapy: toward a focal form of brain stimulation," *Clinical Neuroscience Research,* vol. 4, pp. 39-57, 2004.

[40] T. Spellman, A. V. Peterchev, and S. H. Lisanby, "Focal electrically administered seizure therapy: a novel form of ECT illustrates the roles of current directionality, polarity, and electrode configuration in seziure induction," *Neuropsychopharmacology,* vol. 34, pp. 2002-2010, 2009.

[41] H. A. Sackeim, J. Long, B. Luber, J. R. Moeller, I. Prohovnik, D. P. Devanand, and M. S. Nobler, "Physical properties and quantification of the ECT stimulus: I. Basic principles," *Convuls Ther,* vol. 10, pp. 93-123, Jun 1994.

[42] S. H. Lisanby, B. Luber, A. D. Finck, C. Schroeder, and H. A. Sackeim, "Deliberate seizure induction with repetitive transcranial magnetic stimulation in nonhuman primates.[erratum appears in Arch Gen Psychiatry 2001 May;58(5):515]," *Archives of General Psychiatry,* vol. 58, pp. 199-200, 2001.

[43] S. H. Lisanby, T. E. Schlaepfer, H. U. Fisch, and H. A. Sackeim, "Magnetic seizure therapy of major depression," *Archives of General Psychiatry,* vol. 58, pp. 303-5, 2001.

[44] S. H. Lisanby, T. D. Moscrip, O. Morales, B. Luber, C. Schroeder, and H. A. Sackeim, "Neurophysiological characterization of magnetic seizure therapy (MST) in non-human primates," *Clin Neurophysiol Suppl,* vol. 56, pp. 81-99, 11-14 June, 2003 2003.

[45] Z.-D. Deng, S. H. Lisanby, and A. V. Peterchev, "Effect of anatomical variability on neural stimulation strength and focality in electroconvulsive therapy (ECT) and magnetic seizure therapy (MST)," in *Conf Proc IEEE Eng Med Biol Soc*, 2009, pp. 682-688.

[46] Z.-D. Deng, A. V. Peterchev, and S. H. Lisanby, "Focality of neural stimulation with magnetic seizure therapy (MST) and electroconvulsive therapy (ECT) in humans and non-human primates," in *Abstracts of the 64th Annual Meeting of the Society of Biological Psychiatry*, 2009, pp. 219S-220S.

[47] Y. M. Cycowicz, B. Luber, T. Spellman, and S. H. Lisanby, "Differential neurophysiological effects of magnetic seizure therapy (MST) and electroconvulsive shock (ECS) in non-human primates," *Clin EEG Neurosci,* vol. 39, pp. 144-9, Jul 2008.

[48] Y. M. Cycowicz, B. Luber, T. Spellman, and S. H. Lisanby, "Neurophysiological Characterization of High-Dose Magnetic Seizure Therapy: Comparisons With Electroconvulsive Shock and Cognitive Outcomes," *J ECT,* Mar 17 2009.

[49] T. D. Moscrip, H. S. Terrace, H. A. Sackeim, and S. H. Lisanby, "Randomized controlled trial of the cognitive side-effects of magnetic seizure therapy (MST) and electroconvulsive shock (ECS)," *Int J Neuropsychopharmacol,* vol. 9, pp. 1-11, Feb 2006.

[50] Spellman T, McClintock SM, Terrace H, Luber B, Husain MM, and Lisanby SH, "Differential effects of high-dose magnetic seizure therapy and electroconvulsive shock on cognitive function," *Biological Psychiatry,* vol. 63, pp. 1163-1170, 2008.

[51] G. Kirov, K. P. Ebmeier, A. I. Scott, M. Atkins, N. Khalid, L. Carrick, A. Stanfield, R. E. O'Carroll, M. M. Husain, and S. H. Lisanby, "Quick recovery of orientation after magnetic seizure therapy for major depressive disorder," *British Journal of Psychiatry,* vol. 193, pp. 152-5, 2008.

[52] S. Kayser, B. Bewernick, N. Axmacher, and T. E. Schlaepfer, "Magnetic seizure therapy of treatment-resistant depression in a patient with bipolar disorder," *J ECT,* vol. 25, pp. 137-40, Jun 2009.

[53] M. Kosel, C. Frick, S. H. Lisanby, H. U. Fisch, and T. E. Schlaepfer, "Magnetic seizure therapy improves mood in refractory major depression," *Neuropsychopharmacology,* vol. 28, pp. 2045-8, Nov 2003.

[54] W. H. Lee, Z.-D. Deng, T.-S. Kim, A. F. Laine, S. H. Lisanby, and A. V. Peterchev, "Regional electric field induced by electroconvulsive therapy: a finite element simulation study," in *Conf Proc IEEE Eng Med Biol Soc*, 2010, pp. 2045-2048.

[55] W. H. Lee, Z.-D. Deng, T.-S. Kim, A. F. Laine, S. H. Lisanby, and A. V. Peterchev, "Regional electric field induced by electroconvulsive therapy in a realistic finite element head model: influence of white matter anisotropic conductivity," *Neuroimage,* vol. 59, pp. 2110-23, 2012.

[56] W. H. Lee, Z.-D. Deng, A. Laine, S. H. Lisanby, and A. V. Peterchev, "Influence of white matter conductivity anisotropy on electric field strength induced by electroconvulsive therapy," in *Conf Proc IEEE Eng Med Biol Soc*, 2011, pp. 5473-6.

[57] W. H. Lee and T. S. Kim, "Methods for high-resolution anisotropic finite element modeling of the human head: automatic MR white matter anisotropy-adaptive mesh generation," *Med Eng Phys,* vol. 34, pp. 85-98, Jan 2012.

[58] W. H. Lee, S. H. Lisanby, A. F. Laine, and A. V. Peterchev, "Finite element model of the rhesus macaque head: electroconvulsive therapy electric field simulation," *Conf Human Brain Mapping,* 2012.

[59] W. H. Lee, S. H. Lisanby, R. M. Curtis, A. F. Laine, and A. V. Peterchev, "Stimulation strength in hippocampus for various ECT electrode configurations computed in a realistic head model," *J ECT,* vol. 28, pp. 149-150, 2012.

[60] W. H. Lee, S. H. Lisanby, A. F. Laine, and A. V. Peterchev, "Anatomical variability predicts individual differences in transcranial electric stimulation motor threshold," in *Conf Proc IEEE Eng Med Biol Soc*, 2013, pp. 815-818.

[61] W. H. Lee, S. H. Lisanby, A. F. Laine, and A. V. Peterchev, "Stimulation strength and focality of electroconvulsive therapy with individualized current amplitude: a preclinical study," in *Conf Proc IEEE Eng Med Biol*, 2012, pp. 6430-6433.

[62] W. H. Lee, S. H. Lisanby, A. F. Laine, and A. V. Peterchev, "Electric field characteristics of electroconvulsive therapy with individualized current amplitude: a preclinical study," in *Conf Proc IEEE Eng Med Biol Soc*, 2013, pp. 3082-3085.

[63] P. J. Basser, J. Mattiello, and D. Lebihan, "MR Diffusion Tensor Spectroscopy and Imaging," *Biophysical Journal,* vol. 66, pp. 259-267, Jan 1994.

[64] P. J. Basser, J. Mattiello, and D. Lebihan, "Estimation of the Effective Self-Diffusion Tensor from the NMR Spin-Echo," *Journal of Magnetic Resonance Series B,* vol. 103, pp. 247-254, Mar 1994.

[65] T. G. Reese, O. Heid, R. M. Weisskoff, and V. J. Wedeen, "Reduction of eddy-current-induced distortion in diffusion MRI using a twice-refocused spin echo," *Magnetic Resonance in Medicine,* vol. 49, pp. 177-82, Jan 2003.

[66] T. Jaermann, K. P. Pruessmann, A. Valavanis, S. Kollias, and P. Boesiger, "Influence of SENSE on image properties in high-resolution single-shot echo-planar DTI," *Magnetic Resonance in Medicine,* vol. 55, pp. 335-42, Feb 2006.

[67] X. Liu, T. Zhu, T. Gu, and J. Zhong, "Optimization of in vivo high-resolution DTI of non-human primates on a 3T human scanner," *Methods,* vol. 50, pp. 205-13, Mar 2010.

[68] W. H. Lee, Z. D. Deng, T. S. Kim, A. F. Laine, S. H. Lisanby, and A. V. Peterchev, "Regional electric field induced by electroconvulsive therapy in a realistic finite element head model: influence of white matter anisotropic conductivity," *Neuroimage,* vol. 59, pp. 2110-23, Feb 1 2012.

[69] N. J. Tustison, B. B. Avants, P. A. Cook, Y. Zheng, A. Egan, P. A. Yushkevich, and J. C. Gee, "N4ITK: improved N3 bias correction," *IEEE Trans Med Imaging,* vol. 29, pp. 1310-20, Jun 2010.

[70] E. Ardizzone, R. Pirrone, and O. Gambino, "Automatic segmentation of MR images based on adaptive anisotropic filtering," *12th International Conference on Image Analysis and Processing, Proceedings,* pp. 283-288, 2003.

[71] W. H. Lee, T. S. Kim, M. H. Cho, Y. B. Ahn, and S. Y. Lee, "Methods and evaluations of MRI content-adaptive finite element mesh generation for bioelectromagnetic problems," *Physics in Medicine and Biology,* vol. 51, pp. 6173-6186, Dec 7 2006.

[72] J. Weickert, "A review of nonlinear diffusion filtering," *Scale-Space Theory in Computer Vision,* vol. 1252, pp. 3-28, 1997.

[73] S. Kim, T. S. Kim, Y. X. Zhou, and M. Singh, "Influence of conductivity tensors on the scalp electrical potential: Study with 2-D finite element models," *IEEE Transactions on Nuclear Science,* vol. 50, pp. 133-139, Feb 2003.

[74] S. M. Smith, M. Jenkinson, M. W. Woolrich, C. F. Beckmann, T. E. Behrens, H. Johansen-Berg, P. R. Bannister, M. De Luca, I. Drobnjak, D. E. Flitney, R. K. Niazy, J. Saunders, J. Vickers, Y. Zhang, N. De Stefano, J. M. Brady, and P. M. Matthews, "Advances in functional and structural MR image analysis and implementation as FSL," *Neuroimage,* vol. 23 Suppl 1, pp. S208-19, 2004.

[75] P. A. Yushkevich, J. Piven, H. C. Hazlett, R. G. Smith, S. Ho, J. C. Gee, and G. Gerig, "User-guided 3D active contour segmentation of anatomical structures: significantly improved efficiency and reliability," *Neuroimage,* vol. 31, pp. 1116-28, Jul 1 2006.

[76] J. Ashburner and K. J. Friston, "Unified segmentation," *Neuroimage,* vol. 26, pp. 839-51, Jul 1 2005.

[77] D. G. McLaren, K. J. Kosmatka, T. R. Oakes, C. D. Kroenke, S. G. Kohama, J. A. Matochik, D. K. Ingram, and S. C. Johnson, "A population-average MRI-based atlas collection of the rhesus macaque," *Neuroimage,* vol. 45, pp. 52-9, Mar 1 2009.

[78] D. G. McLaren, K. J. Kosmatka, E. K. Kastman, B. B. Bendlin, and S. C. Johnson, "Rhesus macaque brain morphometry: a methodological comparison of voxel-wise approaches," *Methods,* vol. 50, pp. 157-65, Mar 2010.

[79] R. Abrams, *Electroconvulsive Therapy*, 4th ed. New York: Oxford Unversity Press, 2002.

[80] APA, *The Practice of Electroconvulsive Therapy: Recommendations for Treatment, and Privileging: A Task Force Report of the American Psychiatric Association*. Washington, D.C.: American Psychiatric Association, 2001.

[81] H. A. Sackeim, "Convulsant and anticonvulsant properties of electroconvulsive therapy: towards a focal form of brain stimulation," *Clinical Neuroscience Research,* vol. 4, pp. 39-57, Jul 2004.

[82] T. Spellman, A. V. Peterchev, and S. H. Lisanby, "Focal electrically administered seizure therapy: a novel form of ECT illustrates the roles of current directionality, polarity, and electrode configuration in seizure induction," *Neuropsychopharmacology,* vol. 34, pp. 2002-10, Jul 2009.

[83] R. Jalinous, "Technical and practical aspects of magnetic nerve stimulation," *J Clin Neurophysiol,* vol. 8, pp. 10-25, Jan 1991.

[84] R. Jalinous. (1998, Guide to Magnetic Stimulation. Available: http://jalimedical.com/guide.html

[85] T. A. Wagner, M. Zahn, A. J. Grodzinsky, and A. Pascual-Leone, "Three-dimensional head model simulation of transcranial magnetic stimulation," *IEEE Trans Biomed Eng,* vol. 51, pp. 1586-1598, Sep 2004.

[86] Z.-D. Deng, S. H. Lisanby, and A. V. Peterchev, "Electric field strength and focality in electroconvulsive therapy and magnetic seizure therapy: a finite element simulation study," *J Neural Eng,* vol. 8, p. 016007, 2011.

[87] J. D. Boissonnat and S. Oudot, "Provably good sampling and meshing of surfaces," *Graphical Models,* vol. 67, pp. 405-451, Sep 2005.

[88] J. P. Pons, E. Segonne, J. D. Boissonnat, L. Rineau, M. Yvinec, and R. Keriven, "High-quality consistent meshing of multi-label datasets," *Inf Process Med Imaging,* vol. 20, pp. 198-210, 2007.

[89] K. A. Awada, D. R. Jackson, S. B. Baumann, J. T. Williams, D. R. Wilton, P. W. Fink, and B. R. Prasky, "Effect of conductivity uncertainties and modeling errors on EEG source localization using a 2-D model," *IEEE Transactions on Biomedical Engineering,* vol. 45, pp. 1135-1145, Sep 1998.

[90] C. H. Wolters, A. Anwander, X. Tricoche, D. Weinstein, M. A. Koch, and R. S. MacLeod, "Influence of tissue conductivity anisotropy on EEG/MEG field and return current computation in a realistic head model: a simulation and visualization study using high-resolution finite element modeling," *Neuroimage,* vol. 30, pp. 813-826, 2006.

[91] R. J. Sadleir, T. D. Vannorsdall, D. J. Schretlen, and B. Gordon, "Transcranial direct current stimulation (tDCS) in a realistic head model," *Neuroimage,* vol. 51, pp. 1310-1318, 2010.

[92] D. C. Alexander, C. Pierpaoli, P. J. Basser, and J. C. Gee, "Spatial transformations of diffusion tensor magnetic resonance images," *IEEE Trans Med Imaging,* vol. 20, pp. 1131-9, Nov 2001.

[93] D. Gullmar, J. Haueisen, and J. R. Reichenbach, "Influence of anisotropic electrical conductivity in white matter tissue on the EEG/MEG forward and inverse solution. A high-resolution whole head simulation study," *Neuroimage,* vol. 51, pp. 145-163, May 15 2010.

[94] H. Hallez, S. Staelens, and I. Lemahieu, "Dipole estimation errors due to not incorporating anisotropic conductivities in realistic head models for EEG source analysis," *Physics in Medicine and Biology,* vol. 54, pp. 6079-6093, Oct 21 2009.

[95] H. Hallez, B. Vanrumste, P. Van Hese, S. Delputte, and I. Lemahieu, "Dipole estimation errors due to differences in modeling anisotropic conductivities in realistic head models for EEG source analysis," *Physics in Medicine and Biology,* vol. 53, pp. 1877-1894, Apr 7 2008.

[96] H. S. Suh, W. H. Lee, and T. S. Kim, "Influence of anisotropic conductivity in the skull and white matter on transcranial direct current stimulation via an anatomically realistic finite element head model," *Physics in Medicine and Biology,* vol. 57, pp. 6961-80, Nov 7 2012.

[97] W. H. Lee, Z. M. Liu, B. A. Mueller, K. Lim, and B. He, "Influence of white matter anisotropic conductivity on EEG source localization: Comparison to fMRI in human primary visual cortex," *Clinical Neurophysiology,* vol. 120, pp. 2071-2081, Dec 2009.

[98] G. Ruffini, F. Wendling, I. Merlet, B. Molaee-Ardekani, A. Mekkonen, R. Salvador, A. Soria-Frisch, C. Grau, S. Dunne, and P. Miranda, "Transcranial Current Brain Stimulation (tCS): Models and Technologies," *IEEE Trans Neural Syst Rehabil Eng,* Sep 4 2012.

[99] P. C. Miranda, M. Hallett, and P. J. Basser, "The electric field induced in the brain by magnetic stimulation: a 3-D finite-element analysis of the effect of tissue heterogeneity and anisotropy," *IEEE Trans Biomed Eng,* vol. 50, pp. 1074-1085, 2003.

[100] M. Chen and D. J. Mogul, "Using increased structural detail of the cortex to improve the accuracy of modeling the effects of transcranial magnetic stimulation on neocortical activation," *IEEE Trans Biomed Eng,* vol. 57, pp. 1216-1226, 2010.

[101] *ANSYS Theory Reference*, 9th ed., 2004.

[102] C. A. Bossetti, M. J. Birdno, and W. M. Grill, "Analysis of the quasi-static approximation for calculating potentials generated by neural stimulation," *J Neural Eng,* vol. 5, pp. 44-53, Mar 2008.

[103] R. Plonsey and D. B. Heppner, "Considerations of Quasi-Stationarity in Electrophysiological Systems," *Bulletin of Mathematical Biophysics,* vol. 29, pp. 657-664, 1967.

[104] B. J. Roth and P. J. Basser, "A model of the stimulation of a nerve fiber by electromagnetic induction," *IEEE Trans Biomed Eng,* vol. 37, pp. 588-597, Jun 1990.

[105] C. A. Bossetti, M. J. Birdno, and W. M. Grill, "Analysis of the quasi-static approximation for calculating potentials generated by neural stimulation," *Journal of Neural Engineering,* vol. 5, pp. 44-53, Mar 2008.

[106] F. Rattay, "Modeling the Excitation of Fibers under Surface Electrodes," *IEEE Transactions on Biomedical Engineering,* vol. 35, pp. 199-202, Mar 1988.

[107] L. R. Squire, "Memory Functions as Affected by Electroconvulsive-Therapy," *Annals of the New York Academy of Sciences,* vol. 462, pp. 307-314, Mar 14 1986.

[108] G. A. Nuttall, M. R. Bowersox, S. B. Douglass, J. McDonald, L. J. Rasmussen, P. A. Decker, W. C. Oliver, and K. G. Rasmussen, "Morbidity and mortality in the use of electroconvulsive therapy," *Journal of Ect,* vol. 20, pp. 237-241, Dec 2004.

[109] H. A. Sackeim, J. Prudic, D. P. Devanand, P. Decina, B. Kerr, and S. Malitz, "The impact of medication resistance and continuation pharmacotherapy on relapse following response to electroconvulsive therapy in major depression," *J Clin Psychopharmacol,* vol. 10, pp. 96-104, Apr 1990.

[110] C. H. Kellner, K. G. Tobias, and J. Wiegand, "Electrode placement in electroconvulsive therapy (ECT): a review of the literature," *J ECT,* vol. 26, pp. 175-180, 2010.

[111] A. V. Peterchev, M. A. Rosa, Z. D. Deng, J. Prudic, and S. H. Lisanby, "Electroconvulsive therapy stimulus parameters: rethinking dosage," *J ECT,* vol. 26, pp. 159-74, Sep 2010.

[112] H. A. Sackeim, J. Prudic, D. P. Devanand, M. S. Nobler, S. H. Lisanby, S. Peyser, L. Fitzsimons, B. J. Moody, and J. Clark, "A prospective, randomized, double-blind comparison of bilateral and right unilateral electroconvulsive therapy at different stimulus intensities," *Archives of General Psychiatry,* vol. 57, pp. 425-434, May 2000.

[113] F. M. Lorimer, M. M. Segal, and S. N. Stein, "Path of current distribution in brain during electro-convulsive therapy; preliminary report," *Electroencephalogr Clin Neurophysiol,* vol. 1, pp. 343-8, Aug 1949.

[114] J. W. Smitt and C. F. Wegener, "ON ELECTRIC CONVULSIVE THERAPY with particular regard to a parietal application of electrodes, controlled by intracerebral voltage measurements," *Acta Psychiatrica Et Neurologica,* vol. 19, pp. 529-549, 1944.

[115] S. Rush and D. A. Driscoll, "Current Distribution in Brain from Surface Electrodes," *Anesthesia and Analgesia Current Researches,* vol. 47, pp. 717-&, 1968.

[116] Z. D. Deng, S. H. Lisanby, and A. V. Peterchev, "Effect of anatomical variability on neural stimulation strength and focality in electroconvulsive therapy (ECT) and magnetic seizure therapy (MST)," *Conf Proc IEEE Eng Med Biol Soc,* vol. 2009, pp. 682-8, 2009.

[117] Z. D. Deng, S. H. Lisanby, and A. V. Peterchev, "Electric field strength and focality in electroconvulsive therapy and magnetic seizure therapy: a finite element simulation study," *J Neural Eng,* vol. 8, p. 016007, Jan 19 2011.

[118] L. Weaver, R. Williams, and S. Rush, "Current density in bilateral and unilateral ECT," *Biol Psychiatry,* vol. 11, pp. 303-312, 1976.

[119] S. Bai, C. Loo, A. Al Abed, and S. Dokos, "A computational model of direct brain excitation induced by electroconvulsive therapy: comparison among three conventional electrode placements," *Brain Stimul,* vol. 5, pp. 408-21, 2012.

[120] M. Sekino and S. Ueno, "Comparison of current distributions in electroconvulsive therapy and transcranial magnetic stimulation," *J Appl Phys,* vol. 91, pp. 8730-8732, May 15 2002.

[121] M. Sekino and S. Ueno, "FEM-based determination of optimum current distribution in transcranial magnetic stimulation as an alternative to electroconvulsive therapy," *IEEE Trans Magn,* vol. 40, pp. 2167-2169, 2004.

[122] M. Nadeem, T. Thorlin, O. P. Gandhi, and M. A. Persson, "Computation of electric and magnetic stimulation in human head using the 3-D impedance method," *IEEE Trans Biomed Eng,* vol. 50, pp. 900-907, 2003.

[123] R. Szmurło, B. Sawicki, J. Starzynski, and S. Wincenciak, "A comparison of two models of electrodes for ECT simulations," *Ieee Transactions on Magnetics,* vol. 42, pp. 1395-1398, Apr 2006.

[124] A. Datta, V. Bansal, J. Diaz, J. Patel, D. Reato, and M. Bikson, "Gyri-precise head model of transcranial direct current stimulation: Improved spatial focality using a ring electrode versus conventional rectangular pad," *Brain Stimulation,* vol. 2, pp. 201-207, 2009.

[125] A. Datta, M. Elwassif, F. Battaglia, and M. Bikson, "Transcranial current stimulation focality using disc and ring electrode configurations: FEM analysis," *J Neural Eng,* vol. 5, pp. 163-74, Jun 2008.

[126] F. Grandori and P. Rossini, "Electrical stimulation of the motor cortex: theoretical considerations," *Annals of Biomedical Engineering,* vol. 16, pp. 639-52, 1988.

[127] W. H. Lee, H. S. Seo, S. H. Kim, M. H. Cho, S. Y. Lee, and T. S. Kim, "Influence of white matter anisotropy on the effects of transcranial direct current stimulation: a finite element study," *Int Conf Biomed Eng,* vol. 2009, pp. 460-4, 2009.

[128] P. C. Miranda, L. Correia, R. Salvador, and P. J. Basser, "Tissue heterogeneity as a mechanism for localized neural stimulation by applied electric fields," *Physics in Medicine and Biology,* vol. 52, pp. 5603-5617, Sep 21 2007.

[129] P. C. Miranda, M. Lomarev, and M. Hallett, "Modeling the current distribution during transcranial direct current stimulation," *Clin Neurophysiol,* vol. 117, pp. 1623-1629, 2006.

[130] S. S. Nathan, S. R. Sinha, B. Gordon, R. P. Lesser, and N. V. Thakor, "Determination of Current-Density Distributions Generated by Electrical-Stimulation of the Human Cerebral-Cortex," *Electroencephalography and Clinical Neurophysiology,* vol. 86, pp. 183-192, Mar 1993.

[131] M. Parazzini, S. Fiocchi, E. Rossi, A. Paglialonga, and P. Ravazzani, "Transcranial direct current stimulation: estimation of the electric field and of the current density in an anatomical human head model," *IEEE Trans Biomed Eng,* vol. 58, pp. 1773-80, 2011.

[132] R. Salvador, A. Mekonnen, G. Ruffini, and P. C. Miranda, "Modeling the electric field induced in a high resolution realistic head model during transcranial current stimulation," *Conf Proc IEEE Eng Med Biol Soc,* vol. 2010, pp. 2073-6, 2010.

[133] J. M. Saypol, B. J. Roth, L. G. Cohen, and M. Hallett, "A theoretical comparison of electric and magnetic stimulation of the brain," *Annals of Biomedical Engineering,* vol. 19, pp. 317-28, 1991.

[134] M. M. Stecker, "Transcranial electric stimulation of motor pathways: a theoretical analysis," *Comput Biol Med,* vol. 35, pp. 133-155, 2005.

[135] H. S. Suh, S. H. Kim, W. H. Lee, and T. S. Kim, "Realistic simulation of transcranial direct current stimulation via 3-d high-resolution finite element analysis: Effect of tissue anisotropy," *Conf Proc IEEE Eng Med Biol Soc,* vol. 2009, pp. 638-41, 2009.

[136] V. Suihko, "Modelling the response of scalp sensory receptors to transcranial electrical stimulation," *Medical & Biological Engineering & Computing,* vol. 40, pp. 395-401, Jul 2002.

[137] T. Wagner, F. Fregni, S. Fecteau, A. Grodzinsky, M. Zahn, and A. Pascual-Leone, "Transcranial direct current stimulation: A computer-based human model study," *Neuroimage,* vol. 35, pp. 1113-1124, Apr 15 2007.

[138] R. N. Holdefer, R. J. Sadleir, and M. J. Russell, "Predicted current densities in the brain during transcranial electrical stimulation," *Clin Neurophysiol,* vol. 117, pp. 1388-1397, 2006.

[139] C.-H. Im, H.-H. Jung, J.-D. Choi, S. Y. Lee, and K.-Y. Jung, "Determination of optimal electrode positions for transcranial direct current stimulation (tDCS)," *Phys Med Biol,* vol. 53, pp. N219-N225, 2008.

[140] T. F. Oostendorp, Y. A. Hengeveld, C. H. Wolters, J. Stinstra, G. van Elswijk, and D. F. Stegeman, "Modeling transcranial DC stimulation," in *Conf Proc IEEE Eng Med Biol Soc*, 2008, pp. 4226-4229.

[141] M. S. Korgaonkar, S. M. Grieve, S. H. Koslow, J. D. Gabrieli, E. Gordon, and L. M. Williams, "Loss of white matter integrity in major depressive disorder: Evidence using tract-based spatial statistical analysis of diffusion tensor imaging," *Human Brain Mapping,* Dec 17 2010.

[142] F. Wu, Y. Tang, K. Xu, L. Kong, W. Sun, F. Wang, D. Kong, Y. Li, and Y. Liu, "Whiter matter abnormalities in medication-naive subjects with a single short-duration episode of major depressive disorder," *Psychiatry Res,* vol. 191, pp. 80-3, Jan 30 2011.

[143] D. Gullmar, J. Haueisen, M. Eiselt, F. Giessler, L. Flemming, A. Anwander, T. R. Knoesche, C. H. Wolters, M. Dumpelmann, D. S. Tuch, and J. R. Reichenbach, "Influence of anisotropic conductivity on EEG source reconstruction: Investigations in a rabbit model," *IEEE Transactions on Biomedical Engineering,* vol. 53, pp. 1841-1850, Sep 2006.

[144] J. Haueisen, C. Ramon, M. Eiselt, H. Brauer, and H. Nowak, "Influence of tissue resistivities on neuromagnetic fields and electric potentials studied with a finite element model of the head," *Ieee Transactions on Biomedical Engineering,* vol. 44, pp. 727-735, Aug 1997.

[145] W. H. Lee, T. S. Kim, A. T. Kim, and S. Y. Lee, "3-D diffusion tensor MRI anisotropy content-adaptive finite element head model generation for bioelectromagnetic imaging," *Conf Proc IEEE Eng Med Biol Soc,* vol. 2008, pp. 4003-6, 2008.

[146] G. Marin, C. Guerin, S. Baillet, L. Garnero, and G. Meunier, "Influence of skull anisotropy for the forward and inverse problem in EEG: Simulation studies using FEM on realistic head models," *Human Brain Mapping,* vol. 6, pp. 250-269, 1998.

[147] M. Rullmann, A. Anwander, M. Dannhauer, S. K. Warfield, F. H. Duffy, and C. H. Wolters, "EEG source analysis of epileptiform activity using a 1 mm anisotropic hexahedra finite element head model," *Neuroimage,* vol. 44, pp. 399-410, Jan 15 2009.

[148] H. S. Suh, W. H. Lee, Y. S. Cho, J. H. Kim, and T. S. Kim, "Reduced spatial focality of electrical field in tDCS with ring electrodes due to tissue anisotropy," *Conf Proc IEEE Eng Med Biol Soc,* vol. 1, pp. 2053-6, 2010.

[149] C. R. Butson, S. E. Cooper, J. M. Henderson, and C. C. McIntyre, "Patient-specific analysis of the volume of tissue activated during deep brain stimulation," *Neuroimage,* vol. 34, pp. 661-70, Jan 15 2007.

[150] M. De Lucia, G. J. M. Parker, K. Embleton, J. M. Newton, and V. Walsh, "Diffusion tensor MRI-based estimation of the influence of brain tissue anisotropy on the effects of transcranial magnetic stimulation," *Neuroimage,* vol. 36, pp. 1159-1170, Jul 15 2007.

[151] A. Thielscher, A. Opitz, and M. Windhoff, "Impact of the gyral geometry on the electric field induced by transcranial magnetic stimulation," *Neuroimage,* vol. 54, pp. 234-243, 2011.

[152] J. F. P. J. Abascal, S. R. Arridge, D. Atkinson, R. Horesh, L. Fabrizi, M. De Lucia, L. Horesh, R. H. Bayford, and D. S. Holder, "Use of anisotropic modelling in electrical impedance tomography; Description of method and preliminary assessment of utility in imaging brain function in the adult human head," *Neuroimage,* vol. 43, pp. 258-268, Nov 1 2008.

[153] D. S. Tuch, V. J. Wedeen, A. M. Dale, J. S. George, and J. W. Belliveau, "Conductivity mapping of biological tissue using diffusion MRI," *Ann N Y Acad Sci,* vol. 888, pp. 314-6, Oct 30 1999.

[154] D. S. Tuch, V. J. Wedeen, A. M. Dale, J. S. George, and J. W. Belliveau, "Conductivity tensor mapping of the human brain using diffusion tensor MRI," *Proc Natl Acad Sci U S A,* vol. 98, pp. 11697-11701, September 25, 2001 2001.

[155] J. Haueisen, D. S. Tuch, C. Ramon, P. H. Schimpf, V. J. Wedeen, J. S. George, and J. W. Belliveau, "The influence of brain tissue anisotropy on human EEG and MEG," *Neuroimage,* vol. 15, pp. 159-66, Jan 2002.

[156] J. S. Shimony, R. C. McKinstry, E. Akbudak, J. A. Aronovitz, A. Z. Snyder, N. F. Lori, T. S. Cull, and T. E. Conturo, "Quantitative diffusion-tenser anisotropy brain MR imaging: Normative human data and anatomic analysis," *Radiology,* vol. 212, pp. 770-784, Sep 1999.

[157] P. W. Nicholson, "Specific Impedance of Cerebral White Matter," *Experimental Neurology,* vol. 13, pp. 386-401, 1965.

[158] K. Wang, S. Zhu, B. A. Mueller, K. O. Lim, Z. M. Liu, and B. He, "A New Method to Derive White Matter Conductivity From Diffusion Tensor MRI," *IEEE Transactions on Biomedical Engineering,* vol. 55, pp. 2481-2486, Oct 2008.

[159] W. M. Wells, 3rd, P. Viola, H. Atsumi, S. Nakajima, and R. Kikinis, "Multi-modal volume registration by maximization of mutual information," *Medical Image Analysis,* vol. 1, pp. 35-51, Mar 1996.

[160] D. W. Shattuck and R. M. Leahy, "BrainSuite: An automated cortical surface identification tool," *Medical Image Analysis,* vol. 6, pp. 129-142, Jun 2002.

[161] B. Dogdas, D. W. Shattuck, and R. M. Leahy, "Segmentation of skull and scalp in 3-D human MRI using mathematical morphology," *Human Brain Mapping,* vol. 26, pp. 273-285, Dec 2005.

[162] L. A. Geddes and L. E. Baker, "The specific resistance of biological material--a compendium of data for the biomedical engineer and physiologist," *Med Biol Eng,* vol. 5, pp. 271-93, May 1967.

[163] M. Fuchs, M. Wagner, and J. Kastner, "Development of volume conductor and source models to localize epileptic foci," *Journal of Clinical Neurophysiology,* vol. 24, pp. 101-119, Apr 2007.

[164] M. Akhtari, H. C. Bryant, A. N. Marnelak, E. R. Flynn, L. Heller, J. J. Shih, M. Mandelkern, A. Matlachov, D. M. Ranken, E. D. Best, M. A. DiMauro, R. R. Lee, and W. W. Sutherling, "Conductivities of three-layer live human skull," *Brain Topography,* vol. 14, pp. 151-167, Spr 2002.

[165] S. Rampersad, D. Stegeman, and T. Oostendorp, "On handling the layered structure of the skull in transcranial direct current stimulation models," in *Conf Proc IEEE Eng Med Biol Soc*, 2011, pp. 1989-92.

[166] S. Rampersad, D. Stegeman, and T. Oostendorp, "Single-layer skull approximations perform well in transcranial direct current stimulation modeling," *IEEE Trans Neural Syst Rehabil Eng,* vol. 21, pp. 346-53, 2013.

[167] R. J. Sadleir and A. Argibay, "Modeling skull electrical properties," *Ann Biomed Eng,* vol. 35, pp. 1699-1712, 2007.

[168] M. Chen and D. J. Mogul, "A structurally detailed finite element human head model for simulation of transcranial magnetic stimulation," *J Neurosci Methods,* vol. 179, pp. 111-120, Apr 30 2009.

[169] R. Abrams and M. A. Taylor, "Diencephalic stimulation and the effects of ECT in endogenous depression," *Br J Psychiatry,* vol. 129, pp. 482-5, Nov 1976.

[170] A. D. Krystal and R. D. Weiner, "ECT seizure therapeutic adequacy," *Convuls Ther,* vol. 10, pp. 153-164, 1994.

[171] A. D. Krystal, R. D. Weiner, W. V. Mccall, F. E. Shelp, R. Arias, and P. Smith, "The effects of ECT stimulus dose and electrode placement on the ictal electroencephalogram: an intraindividual crossover study," *Biol Psychiatry,* vol. 34, pp. 759-767, Dec 1 1993.

[172] H. S. Mayberg, "Targeted electrode-based modulation of neural circuits for depression," *Journal of Clinical Investigation,* vol. 119, pp. 717-725, Apr 2009.

[173] H. S. Mayberg, A. M. Lozano, V. Voon, H. E. McNeely, D. Seminowicz, C. Hamani, J. M. Schwalb, and S. H. Kennedy, "Deep brain stimulation for treatment-resistant depression," *Neuron,* vol. 45, pp. 651-660, 2005.

[174] C. H. Kellner, R. Knapp, M. M. Husain, K. Rasmussen, S. Sampson, M. Cullum, S. M. McClintock, K. G. Tobias, C. Martino, M. Mueller, S. H. Bailine, M. Fink, and G. Petrides, "Bifrontal, bitemporal and right unilateral electrode placement in ECT: randomised trial," *Br J Psychiatry,* vol. 196, pp. 226-234, 2010.

[175] S. H. Lisanby, J. H. Maddox, J. Prudic, D. P. Devanand, and H. A. Sackeim, "The effects of electroconvulsive therapy on memory of autobiographical and public events," *Arch Gen Psychiatry,* vol. 57, pp. 581-590, 2000.

[176] L. R. Squire, P. C. Slater, and P. L. Miller, "Retrograde-Amnesia and Bilateral Electroconvulsive-Therapy - Long-Term Follow-Up," *Archives of General Psychiatry,* vol. 38, pp. 89-95, 1981.

[177] H. Blumenfeld, M. Westerveld, R. B. Ostroff, S. D. Vanderhill, J. Freeman, A. Necochea, P. Uranga, T. Tanhehco, A. Smith, J. P. Seibyl, R. Stokking, C. Studholme, S. S. Spencer, and I. G. Zubal, "Selective frontal, parietal, and temporal networks in generalized seizures," *Neuroimage,* vol. 19, pp. 1556-1566, 2003.

[178] H. A. Sackeim and S. Mukherjee, "Neurophysiological variability in the effects of the ECT stimulus," *Convuls Ther,* vol. 2, pp. 267-276, 1986.

[179] J. M. Goldstein, L. J. Seidman, N. Makris, T. Ahern, L. M. O'Brien, V. S. Caviness, D. N. Kennedy, S. V. Faraone, and M. T. Tsuang, "Hypothalamic abnormalities in schizophrenia: Sex effects and genetic vulnerability," *Biological Psychiatry,* vol. 61, pp. 935-945, Apr 15 2007.

[180] J. P. John, B. S. Yashavantha, M. Gado, R. Veena, S. Jain, S. Ravishankar, and J. G. Csernansky, "A proposal for MRI-based parcellation of the frontal pole," *Brain Structure & Function,* vol. 212, pp. 245-253, Dec 2007.

[181] N. Makris, J. W. Meyer, J. F. Bates, E. H. Yeterian, D. N. Kennedy, and V. S. Caviness, "MRI-Based topographic parcellation of human cerebral white matter and nuclei II. Rationale and applications with systematics of cerebral connectivity," *Neuroimage,* vol. 9, pp. 18-45, Jan 1999.

[182] L. M. McCormick, S. Ziebell, P. Nopoulos, M. Cassell, N. C. Andreasen, and M. Brumm, "Anterior cingulate cortex: an MRI-based parcellation method," *Neuroimage,* vol. 32, pp. 1167-1175, 2006.

[183] M. Nakamura, P. G. Nestor, J. J. Levitt, A. S. Cohen, T. Kawashima, M. E. Shenton, and R. W. McCarley, "Orbitofrontal volume deficit in schizophrenia and thought disorder," *Brain,* vol. 131, pp. 180-195, Jan 2008.

[184] M. E. Ranta, D. Crocetti, J. A. Clauss, M. A. Kraut, S. H. Mostofsky, and W. E. Kaufmann, "Manual MRI parcellation of the frontal lobe," *Psychiatry Res,* vol. 172, pp. 147-154, 2009.

[185] A. P. Weiss, I. DeWitt, D. Goff, T. Ditman, and S. Heckers, "Anterior and posterior hippocampal volumes in schizophrenia," *Schizophrenia Research,* vol. 73, pp. 103-112, Feb 1 2005.

[186] C. G. Wible, M. E. Shenton, I. A. Fischer, J. E. Allard, R. Kikinis, F. A. Jolesz, D. V. Iosifescu, and R. W. McCarley, "Parcellation of the human prefrontal cortex using MRI," *Psychiatry Research-Neuroimaging,* vol. 76, pp. 29-40, Nov 28 1997.

[187] Z. Tu, K. L. Narr, P. Dollar, I. Dinov, P. M. Thompson, and A. W. Toga, "Brain anatomical structure segmentation by hybrid discriminative/generative models," *IEEE Trans Med Imaging,* vol. 27, pp. 495-508, Apr 2008.

[188] F. Drechsler, C. H. Wolters, T. Dierkes, H. Si, and L. Grasedyck, "A full subtraction approach for finite element method based source analysis using constrained Delaunay tetrahedralisation," *Neuroimage,* vol. 46, pp. 1055-1065, Jul 15 2009.

[189] R. N. Klepfer, C. R. Johnson, and R. S. Macleod, "The effects of inhomogeneities and anisotropies on electrocardiographic fields: A 3-D finite-element study," *IEEE Transactions on Biomedical Engineering,* vol. 44, pp. 706-719, Aug 1997.

[190] J. O. Ottosson, "Experimental studies of memory impairment after electroconvulsive therapy. The role of the electrical stimulation and of the seizure studied by variation of stimulus intensity and modification by lidocaine of seizure discharge," *Acta Psychiatr Scand Suppl,* vol. 35, pp. 103-31, 1960.

[191] P. B. Fitzgerald and Z. J. Daskalakis, "The effects of repetitive transcranial magnetic stimulation in the treatment of depression," *Expert Rev Med Devices,* vol. 8, pp. 85-95, 2011.

[192] H. E. McNeely, H. S. Mayberg, A. M. Lozano, and S. H. Kennedy, "Neuropsychological impact of Cg25 deep brain stimulation for treatment-resistant depression: preliminary results over 12 months," *J Nerv Ment Dis,* vol. 196, pp. 405-410, 2008.

[193] D. A. Gutman, P. E. Holtzheimer, T. E. J. Behrens, H. Johansen-Berg, and H. S. Mayberg, "A tractography analysis of two deep brain stimulation white matter targets for depression," *Biol Psychiatry,* vol. 65, pp. 276-282, 2009.

[194] H. Johansen-Berg, D. A. Gutman, T. E. J. Behrens, P. M. Matthews, M. F. S. Rushworth, E. Katz, A. M. Lozano, and H. S. Mayberg, "Anatomical connectivity of the subgenual cingulate region targeted with deep brain stimulation for treatment-resistant depression," *Cereb Cortex,* vol. 18, pp. 1374-1383, 2008.

[195] H. S. Mayberg, "Targeted electrode-based modulation of neural circuits for depression," *J Clin Invest,* vol. 119, pp. 717-725, 2009.

[196] R. W. Guillery and S. M. Sherman, "Thalamic relay functions and their role in corticocortical communication: generalizations from the visual system," *Neuron,* vol. 33, pp. 163-175, 2002.

[197] K. A. McNally and H. Blumenfeld, "Focal network involvement in generalized seizures: new insights from electroconvulsive therapy," *Epilepsy Behav,* vol. 5, pp. 3-12, 2004.

[198] A. D. Krystal and R. D. Weiner, "Low-frequency ictal EEG activity and ECT therapeutic impact," *Convuls Ther,* vol. 9, pp. 220-222, 1993.

[199] H. A. Sackeim, D. P. Devanand, and J. Prudic, "Stimulus intensity, seizure threshold, and seizure duration: impact on the efficacy and safety of electroconvulsive therapy," *Psychiatr Clin North Am,* vol. 14, pp. 803-43, Dec 1991.

[200] B. Luber, M. S. Nobler, J. R. Moeller, G. P. Katzman, J. Prudic, D. P. Devanand, G. S. Dichter, and H. A. Sackeim, "Quantitative EEG during seizures induced by electroconvulsive therapy: relations to treatment modality and clinical features. II. Topographic analyses," *J ECT,* vol. 16, pp. 229-243, 2000.

[201] L. Squire, "Memory function as affected by electroconvulsive therapy," *Ann N Y Acad Sci,* vol. 462, pp. 307-314, 1986.

[202] S. Oppenheimer, "Cerebrogenic cardiac arrhythmias: Cortical lateralization and clinical significance," *Clinical Autonomic Research,* vol. 16, pp. 6-11, Feb 2006.

[203] S. Oppenheimer, "Cerebrogenic cardiac arrhythmias: cortical lateralization and clinical significance," *Clin Auton Res,* vol. 16, pp. 6-11, 2006.

[204] S. M. Oppenheimer, A. Gelb, J. P. Girvin, and V. C. Hachinski, "Cardiovascular effects of human insular cortex stimulation," *Neurology,* vol. 42, pp. 1727-32, 1992.

[205] J. Nagler, "Absence of asystole during bifrontal stimulation in electroconvulsive therapy," *J ECT,* vol. 26, pp. 100-103, 2010.

[206] C. Loo, P. Stewart, R. MacPherson, and D. Hadzi-Pavlovic, "Lower Incidence of Asystole and Bradycardia With Ultrabrief Pulsewidth Stimulation and Bifrontal Electrode Placement," *Journal of Ect,* vol. 25, pp. 149-150, Jun 2009.

[207] J. Nagler, "Absence of Asystole During Bifrontal Stimulation in Electroconvulsive Therapy," *Journal of Ect,* vol. 26, pp. 100-103, Jun 2010.

[208] C. A. Welch and L. J. Drop, "Cardiovascular Effects of ECT," *Convulsive Therapy,* vol. 5, pp. 35-43, 1989.

[209] J. P. Dmochowski, A. Datta, M. Bikson, Y. Su, and L. C. Parra, "Optimized multi-electrode stimulation increases focality and intensity at target," *J Neural Eng,* vol. 8, p. 046011, 2011.

[210] J.-H. Park, S.-B. Hong, D.-W. Kim, M. Suh, and C.-H. Im, "A novel array-type transcranial direct current stimulation (tDCS) system for accurate focusing on targeted brain areas," *IEEE Trans Magn,* vol. 47, pp. 882-885, 2011.

[211] J. D. Bremner, "Changes in brain volume in major depression," *Depression: Mind and Brain,* vol. 2, pp. 38-46, 2005.

[212] C. Tsopelas, R. Stewart, G. M. Savva, C. Brayne, P. Ince, A. Thomas, and F. E. Matthews, "Neuropathological correlates of late-life depression in older people," *Br J Psychiatry,* vol. 198, pp. 109-14, Feb 2011.

[213] M. Bikson and A. Datta, "Guidelines for precise and accurate computational models of tDCS," *Brain Stimul,* vol. 5, pp. 430-431, 2012.

[214] T. Radman, R. L. Ramos, J. C. Brumberg, and M. Bikson, "Role of cortical cell type and morphology in subthreshold and suprathreshold uniform electric field stimulation in vitro," *Brain Stimul,* vol. 2, pp. 215-228, 2009.

[215] W. A. H. Rushton, "The effect upon the threshold for nervous excitation of the length of nerve exposed, and the angle between current and nerve," *J Physiol,* vol. 63, pp. 357-77, 1927.

[216] N. B. Bangera, D. L. Schomer, N. Dehghani, I. Ulbert, S. Cash, S. Papavasiliou, S. R. Eisenberg, A. M. Dale, and E. Halgren, "Experimental validation of the influence of white matter anisotropy on the intracranial EEG forward solution," *Journal of Computational Neuroscience,* vol. 29, pp. 371-387, Dec 2010.

[217] Z. D. Deng, S. H. Lisanby, and A. V. Peterchev, "Controlling Stimulation Strength and Focality in Electroconvulsive Therapy via Current Amplitude and Electrode Size and Spacing: Comparison With Magnetic Seizure Therapy," *J ECT,* vol. 29, pp. 321-31, Dec 2013.

[218] A. V. Peterchev, M. A. Rosa, Z.-D. Deng, J. Prudic, and S. H. Lisanby, "Electroconvulsive therapy stimulus parameters: rethinking dosage," *J ECT,* vol. 26, pp. 159-174, 2010.

[219] H. A. Sackeim, "Convulsant and anticonvulsant properties of electroconvulsive therapy: towards a focal form of brain stimulation," *Clin Neurosci Res,* vol. 4, pp. 39-57, 2004.

[220] Z. Nahas, B. Short, C. Burns, M. Archer, M. Schmidt, J. Prudic, M. S. Nobler, D. P. Devanand, L. Fitzsimons, S. H. Lisanby, N. Payne, T. Perera, M. S. George, and H. A. Sackeim, "A feasibility study of a new method for electrically producing seizures in man:

focal electrically administered seizure therapy [FEAST]," *Brain Stimul,* vol. 6, pp. 403-408, 2013.

[221] M. A. Rosa, G. L. Abdo, M. O. Rosa, S. H. Lisanby, and A. V. Peterchev, "Fronto-medial electrode placement with low current amplitude: a case report," *J ECT,* vol. 28, p. 146, 2012.

[222] S. B. Rowny, K. Benzl, and S. H. Lisanby, "Translational development strategy for magnetic seizure therapy," *Exp Neurol,* vol. 219, pp. 27-35, Sep 2009.

[223] Z.-D. Deng, S. H. Lisanby, and A. V. Peterchev, "Electric field depth–focality tradeoff in transcranial magnetic stimulation: simulation comparison of 50 coil designs," *Brain Stimul,* vol. 6, pp. 1-13, 2013.

[224] R. D. Weiner, H. J. Rogers, J. R. Davidson, and L. R. Squire, "Effects of stimulus parameters on cognitive side effects," *Ann N Y Acad Sci,* vol. 462, pp. 315-325, 1986.

[225] S. Rossi, M. Hallett, P. M. Rossini, A. Pascual-Leone, and Safety of TMS Consensus Group, "Safety, ethical considerations, and application guidelines for the use of transcranial magnetic stimulation in clinical practice and research," *Clin Neurophysiol,* vol. 120, pp. 2008-2039, Dec 2009.

[226] A. V. Peterchev, B. Chan, and S. H. Lisanby, "Pulse amplitude adjustment: a novel means of individualizing and predicting dosage requirements for electroconvulsive therapy and magnetic seizure therapy," *J ECT* vol. 26, p. 154, 2010.

[227] W. H. Lee, S. H. Lisanby, A. F. Laine, and A. V. Peterchev, "Stimulation strength and focality of electroconvulsive therapy with individualized current amplitude: a preclinical study," *Conf Proc IEEE Eng Med Biol Soc,* vol. 2012, pp. 6430-3, 2012.

[228] D. Edwards, M. Cortes, A. Datta, P. Minhas, E. M. Wassermann, and M. Bikson, "Physiological and modeling evidence for focal transcranial electrical brain stimulation in humans: a basis for high-definition tDCS," *Neuroimage,* vol. 74, pp. 266-75, 2013.

[229] T. D. Moscrip, H. S. Terrace, H. A. Sackeim, and S. H. Lisanby, "A primate model of anterograde and retrograde amnesia produced by convulsive treatment," *J ECT,* vol. 20, pp. 26-36, Mar 2004.

[230] S. H. Lisanby, T. Moscrip, O. Morales, B. Luber, C. Schroeder, and H. A. Sackeim, "Neurophysiological characterization of magnetic seizure therapy (MST) in non-human primates," *Suppl Clin Neurophysiol,* vol. 56, pp. 81-99, 2003.

[231] A. Datta, D. Truong, P. Minhas, L. C. Parra, and M. Bikson, "Inter-Individual Variation during Transcranial Direct Current Stimulation and Normalization of Dose Using MRI-Derived Computational Models," *Front Psychiatry,* vol. 3, p. 91, 2012.

[232] A. Datta, X. Zhou, Y. Su, L. C. Parra, and M. Bikson, "Validation of finite element model of transcranial electrical stimulation using scalp potentials: implications for clinical dose," *J Neural Eng,* vol. 10, p. 036018, 2013.

[233] A. Opitz, W. Legon, A. Rowlands, W. K. Bickel, W. Paulus, and W. J. Tyler, "Physiological observations validate finite element models for estimating subject-specific electric field distributions induced by transcranial magnetic stimulation of the human motor cortex," *Neuroimage,* vol. 81, pp. 253-64, 2013.

[234] D. Q. Truong, G. Magerowski, G. L. Blackburn, M. Bikson, and M. Alonso-Alonso, "Computational modeling of transcranial direct current stimulation (tDCS) in obesity: Impact of head fat and dose guidelines," *Neuroimage: Clinical,* vol. 2013, pp. 759-66, 2013.

[235] A. V. Peterchev, T. A. Wagner, P. C. Miranda, M. A. Nitsche, W. Paulus, S. H. Lisanby, A. Pascual-Leone, and M. Bikson, "Fundamentals of transcranial electric and magnetic stimulation dose: definition, selection, and reporting practices," *Brain Stimul,* vol. 5, pp. 435-453, 2012.

[236] M. Chen and D. J. Mogul, "A structurally detailed finite element human head model for simulation of transcranial magnetic stimulation," *Journal of Neuroscience Methods,* vol. 179, pp. 111-120, Apr 30 2009.

[237] J. P. Dmochowski, A. Datta, Y. Huang, J. D. Richardson, M. Bikson, J. Fridriksson, and L. C. Parra, "Targeted transcranial direct current stimulation for rehabilitation after stroke," *Neuroimage,* vol. 75, pp. 12-19, 2013.

[238] W. H. Lee, Z. D. Deng, A. F. Laine, S. H. Lisanby, and A. V. Peterchev, "Influence of white matter conductivity anisotropy on electric field induced by electroconvulsive therapy," *Conf Proc IEEE Eng Med Biol Soc,* 2011.

[239] M. Sekino and S. Ueno, "FEM-based determination of optimum current distribution in transcranial magnetic stimulation as an alternative to electroconvulsive therapy," *IEEE Transactions on Magnetics,* vol. 40, pp. 2167-2169, Jul 2004.

[240] P. C. Miranda, A. Mekonnen, R. Salvador, and G. Ruffini, "The electric field in the cortex during transcranial current stimulation," *Neuroimage,* vol. 70, pp. 48–58, 2013.

[241] R. Salvador and P. C. Miranda, "Transcranial magnetic stimulation of small animals: a modeling study of the influence of coil geometry, size and orientation," *Conf Proc IEEE Eng Med Biol Soc,* vol. 2009, pp. 674-7, 2009.

[242] W. H. Lee, S. H. Lisanby, A. F. Laine, and A. V. Peterchev, "Anatomical variablity predicts indiviudal differences in transcranial electric stimulation motor threshold," *Conf Proc IEEE Eng Med Biol Soc,* vol. 2013, pp. 815-818, 2013.

[243] G. Ruffini, F. Wendling, I. Merlet, B. Molaee-Ardekani, A. Mekkonen, R. Salvador, A. Soria-Frisch, C. Grau, S. Dunne, and P. Miranda, "Transcranial Current Brain Stimulation (tCS):Models and Technologies," *IEEE Trans Neural Syst Rehabil Eng,* Sep 4 2012.

[244] P. M. Rossini, A. T. Barker, A. Berardelli, M. D. Caramia, G. Caruso, R. Q. Cracco, M. R. Dimitrijevic, M. Hallett, Y. Katayama, C. H. Lucking, and et al., "Non-invasive electrical and magnetic stimulation of the brain, spinal cord and roots: basic principles and procedures for routine clinical application. Report of an IFCN committee," *Electroencephalogr Clin Neurophysiol,* vol. 91, pp. 79-92, Aug 1994.

[245] D. C. Van Essen, "Surface-based atlases of cerebellar cortex in the human, macaque, and mouse," *Ann N Y Acad Sci,* vol. 978, pp. 468-79, Dec 2002.

[246] G. Paxinos, X. F. Huang, and A. W. Toga, *The rhesus monkey brain in stereotaxic coordinates*. San Diego: Academic Press, 2000.

[247] K. S. Saleem and N. K. Logothetis, *A combined MRI and histology atlas of the rhesus monkey brain in stereotaxic coordinates*, 1st ed. Amsterdam ; Boston: Elsevier/Academic Press, 2007.

[248] T. A. Yousry, U. D. Schmid, H. Alkadhi, D. Schmidt, A. Peraud, A. Buettner, and P. Winkler, "Localization of the motor hand area to a knob on the precentral gyrus. A new landmark," *Brain,* vol. 120 (Pt 1), pp. 141-57, Jan 1997.

[249] F. Amaya, W. Paulus, S. Treue, and D. Liebetanz, "Transcranial magnetic stimulation and PAS-induced cortical neuroplasticity in the awake rhesus monkey," *Clin Neurophysiol,* vol. 121, pp. 2143-51, Dec 2010.

[250] J. A. van Waarde, L. J. van Oudheusden, B. A. Tonino, N. J. van der Wee, B. Verwey, R. C. van der Mast, and E. J. Giltay, "MRI characteristics predicting seizure threshold in patients undergoing electroconvulsive therapy: A prospective study," *Brain Stimul,* Jan 5 2013.

[251] M. S. Beauchamp, M. R. Beurlot, E. Fava, A. R. Nath, N. A. Parikh, Z. S. Saad, H. Bortfeld, and J. S. Oghalai, "The developmental trajectory of brain-scalp distance from birth through childhood: implications for functional neuroimaging," *PLoS One,* vol. 6, p. e24981, 2011.

[252] B. Fischl and A. M. Dale, "Measuring the thickness of the human cerebral cortex from magnetic resonance images," *Proc Natl Acad Sci U S A,* vol. 97, pp. 11050-5, Sep 26 2000.

[253] D. Q. Truong, G. Magerowski, A. Pascual-Leone, M. Alonso-Alonso, and M. Bikson, "Finite Element study of skin and fat delineation in an obese subject for transcranial

Direct Current Stimulation," *Conf Proc IEEE Eng Med Biol Soc,* vol. 2012, pp. 6587-90, 2012.

[254] S. Komssi, P. Savolainen, J. Heiskala, and S. Kähkönen, "Excitation threshold of the motor cortex estimated with transcranial magnetic stimulation electroencephalography," *Neuroreport,* vol. 18, pp. 13-16, 2007.

[255] A. Thielscher and T. Kammer, "Linking physics with physiology in TMS: a sphere field model to determine the cortical stimulation site in TMS," *Neuroimage,* vol. 17, pp. 1117-30, Nov 2002.

[256] C. M. Epstein, D. G. Schwartzberg, K. R. Davey, and D. B. Sudderth, "Localizing the site of magnetic brain stimulation in humans," *Neurology,* vol. 40, pp. 666-670, Apr 1990.

[257] D. Rudiak and E. Marg, "Finding the depth of magnetic brain stimulation: a re-evaluation," *Electroencephalogr Clin Neurophysiol,* vol. 93, pp. 358-71, Oct 1994.

[258] B. Calancie, W. Harris, J. G. Broton, N. Alexeeva, and B. A. Green, ""Threshold-level" multipulse transcranial electrical stimulation of motor cortex for intraoperative monitoring of spinal motor tracts: description of method and comparison to somatosensory evoked potential monitoring," *Journal of Neurosurgery,* vol. 88, pp. 457-470, 1998.

[259] N. Danner, P. Julkunen, M. Könönen, L. Säisänen, J. Nurkkala, and J. Karhu, "Navigated transcranial magnetic stimulation and computed electric field strength reduce stimulator-dependent differences in the motor threshold," *J Neurosci Methods,* vol. 174, pp. 116-122, Sep 2008.

[260] W. Cai, J. S. George, C. D. Chambers, M. G. Stokes, F. Verbruggen, and A. R. Aron, "Stimulating deep cortical structures with the batwing coil: how to determine the intensity for transcranial magnetic stimulation using coil-cortex distance," *J Neurosci Methods,* vol. 204, pp. 238-41, 2012.

[261] P. Julkunen, L. Saisanen, T. Hukkanen, N. Danner, and M. Kononen, "Does second-scale intertrial interval affect motor evoked potentials induced by single-pulse transcranial magnetic stimulation?," *Brain Stimul,* vol. 5, pp. 526-32, Oct 2012.

[262] P. Julkunen, L. Säisänen, N. Danner, F. Awiszus, and M. Könönen, "Within-subject effect of coil-to-cortex distance on cortical electric field threshold and motor evoked potentials in transcranial magnetic stimulation," *J Neurosci Methods,* vol. 206, pp. 158-164, 2012.

[263] T. Herbsman, L. Forster, C. Molnar, R. Dougherty, D. Christie, J. Koola, D. Ramsey, P. S. Morgan, D. E. Bohning, M. S. George, and Z. Nahas, "Motor threshold in transcranial magnetic stimulation: the impact of white matter fiber orientation and skull-to-cortex distance," *Human Brain Mapping,* vol. 30, pp. 2044-55, Jul 2009.

[264] M. G. Stokes, C. D. Chambers, I. C. Gould, T. English, E. McNaught, O. McDonald, and J. B. Mattingley, "Distance-adjusted motor threshold for transcranial magnetic stimulation," *Clin Neurophysiol,* vol. 118, pp. 1617-25, Jul 2007.

[265] M. G. Stokes, C. D. Chambers, I. C. Gould, T. R. Henderson, N. E. Janko, N. B. Allen, and J. B. Mattingley, "Simple metric for scaling motor threshold based on scalp-cortex distance: application to studies using transcranial magnetic stimulation," *J Neurophysiol,* vol. 94, pp. 4520-4527, December 1, 2005 2005.

[266] K. A. McConnell, Z. Nahas, A. Shastri, J. P. Lorberbaum, F. A. Kozel, D. E. Bohning, and M. S. George, "The transcranial magnetic stimulation motor threshold depends on the distance from coil to underlying cortex: a replication in healthy adults comparing two methods of assessing the distance to cortex," *Biol Psychiatry,* vol. 49, pp. 454-9, Mar 1 2001.

[267] F. A. Kozel, Z. Nahas, C. deBrux, M. Molloy, J. P. Lorberbaum, D. Bohning, S. C. Risch, and M. S. George, "How coil-cortex distance relates to age, motor threshold, and antidepressant response to repetitive transcranial magnetic stimulation," *J Neuropsychiatry Clin Neurosci,* vol. 12, pp. 376-384, 2000.

[268] W. T. Liberson, "Brief stimulus therapy; psysiological and clinical observations," *Am J Psychiatry,* vol. 105, pp. 28-39, Jul 1948.

[269] B. Cronholm and J. O. Ottosson, "Ultrabrief Stimulus Technique in Electroconvulsive Therapy. Ii. Comparative Studies of Therapeutic Effects and Memory Disturbances in Treatment of Endogenous Depression with the Elther Es Electroshock Apparatus and Siemens Konvulsator Iii," *J Nerv Ment Dis,* vol. 137, pp. 268-76, Sep 1963.

[270] B. Cronholm and J. O. Ottosson, "Ultrabrief Stimulus Technique in Electroconvulsive Therapy. I. Influence on Retrograde Amnesia of Treatments with the Elther Es Electroschock Apparatus, Siemens Konvulsator Iii and of Lidocaine-Modified Treatment," *J Nerv Ment Dis,* vol. 137, pp. 117-23, Aug 1963.

[271] M. A. Rosa, G. L. Abdo, S. H. Lisanby, and A. V. Peterchev, "Seizure induction with low-amplitude-current (0.5A) electroconvulsive therapy," *J ECT* vol. 27, pp. 341-342, 2011.

[272] Z. D. Deng, A. V. Peterchev, and S. H. Lisanby, "Focality of neural stimulation with magnetic seizure therapy (MST) and electroconvulsive therapy (ECT) in humans and non-human primates," *64th Ann Conf Soc Biol Psychiatry,* vol. 2009, 2009.

[273] W. H. Lee, S. H. Lisanby, A. F. Laine, and A. V. Peterchev, "Electric field characteristics of electroconvulsive therapy with individualized current amplitude: a preclinical study," *Conf Proc IEEE Eng Med Biol Soc,* vol. 2013, pp. 3082-3085, 2013.

[274] W. H. Lee, S. H. Lisanby, A. F. Laine, and A. V. Peterchev, "Stimulation strength in hippocampus for various ECT electrode configurations computed in a realistic head model," *J ECT,* vol. 28, p. 149, 2012.

[275] D. Gordon, "Electro-convulsive therapy with minimum hazard," *Br J Psychiatry,* vol. 141, pp. 12-8, Jul 1982.

[276] D. Gordon, "Electroconvulsive therapy," *J Biomed Eng,* vol. 11, pp. 170-1, Mar 1989.

[277] A. Hilkevitch, "Frequency and length of stimulus in electric shock therapy," *AMA Arch Neurol Psychiatry,* vol. 65, p. 245, 1951.

[278] D. Balslev, W. Braet, C. McAllister, and R. C. Miall, "Inter-individual variability in optimal current direction for transcranial magnetic stimulation of the motor cortex," *J Neurosci Methods,* vol. 162, pp. 309-313, May 2007.

[279] T. Kammer, S. Beck, A. Thielscher, U. Laubis-Herrmann, and H. Topka, "Motor thresholds in humans: a transcranial magnetic stimulation study comparing different pulse waveforms, current directions and stimulator types," *Clin Neurophysiol,* vol. 112, pp. 250-258, Feb 2001.

[280] V. Di Lazzaro, A. Oliviero, P. Mazzone, A. Insola, F. Pilato, E. Saturno, A. Accurso, P. Tonali, and J. C. Rothwell, "Comparison of descending volleys evoked by monophasic and biphasic magnetic stimulation of the motor cortex in conscious humans," *Exp Brain Res,* vol. 141, pp. 121-7, Nov 2001.

[281] H. A. Sackeim, S. Portnoy, P. Neeley, B. L. Steif, P. Decina, and S. Malitz, "Cognitive consequences of low-dosage electroconvulsive therapy," *Ann N Y Acad Sci,* vol. 462, pp. 326-40, 1986.

[282] H. A. Sackeim, J. Prudic, D. P. Devanand, J. E. Kiersky, L. Fitzsimons, B. J. Moody, M. C. McElhiney, E. A. Coleman, and J. M. Settembrino, "Effects of stimulus intensity and electrode placement on the efficacy and cognitive effects of electroconvulsive therapy," *N Engl J Med,* vol. 328, pp. 839-846, 1993.

[283] B. Cronholm and J. O. Ottosson, "Ultrabrief stimulus technique in electroconvulsive therapy. II. Comparative studies of therapeutic effects and memory disturbances in treatment of endogenous depression with the Elther ES electroshock apparatus and Siemens Konvulsator III," *J Nerv Ment Dis,* vol. 137, pp. 268-76, Sep 1963.

[284] H. A. Sackeim, J. Prudic, M. S. Nobler, L. Fitzsimons, S. H. Lisanby, N. Payne, R. M. Berman, E.-L. Brakemeier, T. Perera, and D. P. Devanand, "Effects of pulse width and electrode placement on the efficacy and cognitive effects of electroconvulsive therapy," *Brain Stimul,* vol. 1, pp. 71-83, 2008.

[285] H. A. Sackeim, P. Decina, I. Prohvnik, and S. Malitz, "Seizure threshold in electroconvulsive therapy: effects of sex, age, electrode placement, and number of treatments," *Arch Gen Psychiatry,* vol. 44, pp. 355-360, 1987.

[286] T. P. DeMonte, D. Wang, W. Ma, J. H. Gao, and M. L. Joy, "In-vivo measurement of relationship between applied current amplitude and current density magnitude from 10 mA to 110 mA," in *Conf Proc IEEE Eng Med Biol Soc*, 2009, pp. 3177-3180.

[287] M. L. G. Joy, V. P. Lebedev, and J. S. Gati, "Imaging of current density and current pathways in rabbit brain during transcranial electrostimulation," *IEEE Trans Biomed Eng,* vol. 46, pp. 1139-1149, 1999.

[288] E. Dayan, N. Censor, E. R. Buch, M. Sandrini, and L. G. Cohen, "Noninvasive brain stimulation: from physiology to network dynamics and back," *Nat Neurosci,* vol. 16, pp. 838-44, Jul 2013.